CORA Cork Open Research Archive
Cartlann Taighde Oscailte Chorcaí

Title	Small angle scattering characterisation of micellar systems and templated architectures
Authors	O'Callaghan, John M.
Publication date	2010-04
Original Citation	O'Callaghan, J.M., 2010. Small angle scattering characterisation of micellar systems and templated architectures. PhD Thesis, University College Cork.
Type of publication	Doctoral thesis
Link to publisher's version	http://library.ucc.ie/record=b1999321~S0
Rights	©2010, John M. O'Callaghan - http://creativecommons.org/licenses/by-nc-nd/3.0/
Download date	2026-11-15 16:19:34
Item downloaded from	https://hdl.handle.net/10468/177



UCC
University College Cork, Ireland
Coláiste na hOllscoile Corcaigh

Small Angle Scattering Characterisation of Micellar Systems and Templated Architectures

John M. O'Callaghan, BSc.

Department of Chemistry,

University College Cork,

Ireland.



Presented for the PhD. Degree to the National University of Ireland

Supervisor

Dr. Justin D. Holmes

April 2010

"The key to creativity and philosophy is the lack of sleep"

-Kirk Ziegler, RAL Sept. 2003

"...the aggregate of our joy and suffering..."

-Carl Sagan, The Pale Blue Dot

Declaration

I John O'Callaghan certify that this Thesis is my own work and I have not obtained a degree in this University or elsewhere on the basis of this PhD Thesis.

_____

John O'Callaghan

Abstract

The work described in this thesis reports the structural changes induced on micelles under a variety of conditions. The micelles of a liquid crystal film and dilute solutions of micelles were subjected to high pressure CO_2 and selected hydrocarbon environments. Using small angle neutron scattering (SANS) techniques the spacing between liquid crystal micelles was measured *in-situ*. The liquid crystals studied were templated from different surfactants with varying structural characteristics. Micelles of a dilute surfactant solution were also subjected to elevated pressures of varying gas atmospheres. Detailed modelling of the *in-situ* SANS experiments revealed information of the size and shape of the micelles at a number of different pressures.

Also reported in this thesis is the characterisation of mesoporous materials in the confined channels of larger porous materials. Periodic mesoporous organosilicas (PMOs) were synthesised within the channels of anodic alumina membranes (AAM) under different conditions, including drying rates and precursor concentrations. *In-situ* small angle x-ray scattering (SAXS) and transmission electron microscopy (TEM) was used to determine the pore morphology of the PMO within the AAM channels.

PMO materials were also used as templates in the deposition of gold nanoparticles and subsequently used in the synthesis of germanium nanostructures. Polymer thin films were also employed as templates for the directed deposition of gold nanoparticles which were again used as seeds for the production of germanium nanostructures. A supercritical CO_2 (sc-CO_2) technique was successfully used during the production of the germanium nanostructures.

Acknowledgments

Firstly I would like to thank Dr. Justin Holmes for the opportunity to undertake this PhD, for the chance to publish my work and for his patience, suggestions and corrections. I would also like to thank Prof. Mick Morris, Dr. Richard Heenan and Dr. David Steytler.

All the technical and administration staff of the Chemistry Department, thank you for your support and help Johnny, Mick, Tony, Christine, Terry, Pat, Donnacha and Matthias who thought me everything I know about the joys of modern computing.

I want to thank the following people, so in no order or sense. Thank you Richie Farrell, firstly for suggesting a PhD to me way-back-when and secondly for his expert knowledge of ceria and all other worldly things. Next are John Hanrahan and Mark Copley who introduced me to wonderful places called beamlines where we spent many long days and cosy nights typing "CSET JULABO", at the time I had no clue what I was doing either scientifically or with respect to anything else.

Everyone I went travelling with, thank you Joe, Frank, Mark, Justin, Gill and Tom, we always happened to be going to someone's wedding. Thank you Brian and Deana, Jaideep and Anjali, Aoife and Dave for said wedding, bringing 115 and 343 to Canada/India/Spain made it just like going to a wedding in Cork. Special thanks go to Keith and Justin who saved my life when I did that thing, that time.

I would also like to thank everyone who passed through and who is still in Lab 115 or 343. From different eras, Lab 115 (past) John, Joe, Guillaume, Jaideep, Donna, Dáire, Wen-Hua, Mark, Tim and Ju. The old 115 thought me to be thankful of a clean and safe working environment and that pork-chop are an acceptable lunch time snack. Thanks also go to my peer Malcolm, I may have got there first but he helped me in more ways than he can ever know.

From Lab 115 (present) Justin, Pal Paul, Gillian, Richard, Macteld, Dave Ciara and Richard thank you all, and I forgive you Paul for dancing with the devil and who

knew the rapid expansion of liquefied gas at room temperature under constant volume could be so entertaining, and I would like to mention it is "*not a crime*".

Thank you all from Lab 343 (past), Mark, Richie, Frank, Jenny, Donal, Paudie, Tom, Dennis, Jacqui, Kaixue, Rory, Eoin, Barbara, Matt, Louise and Nikolay and from Lab 343 (present) Keith, Pete, Aoife, Colm & Colm and Sheena. Thank you all for your friendship and support over the past years.

I cannot limit my appreciation to people who helped me during my PhD without thanking those in the School of Pharmacy who witnessed/endured the greatest moments of my thesis writing. Firstly I want to thank my best friend Caroline, your support and friendship made everything so much easier for me in countless ways. I would also like to thank Marie and Aoife for the numerous consultations when I was suffering from the black lung and thank you Martin for your great impressions of me during my time as a practicing and fully qualified Pre-Doc. Timmy, thank you so much for all the kind words of support and understanding. I also sincerely thank Fatma and Waleed and Rakesh for your support and kindness over the past two years.

Thank you Jenny not only for the office space but for understanding the struggle that goes with writing a thesis, it made the process tremendously easier. Also I need to thank Abina and Katie for their understanding during the protracted "finishing" stage. Thank you also to Trevor, Marion, Cristin, and Phillip who wished me well along the way.

Finally I would like to thank my parents, this thesis is a reflection of your efforts not only mine.

Dedicated to my mother and father.

Table of Contents

Chapter 1

Introduction	1
1.0 Surface Active Agents	2
1.1 Non-Ionic Surfactants	4
1.2 Ionic Surfactants	7
1.3 Micelle Formation	7
1.4 Liquid Crystals	9
1.5 Applications of Surfactants	12
1.6 Pluronic Surfactants in the Production of Mesoporous Silica	15
1.7 Small Angle Scattering	24
1.8 Overview	32
1.9 References	32
Chapter 2 Experimental	39
2.1 Experimental Methods	40
2.2 Characterisation Techniques	51
2.3 Central Facility Beamline Parameters	62
2.4 Small Angle Scattering Theory	64
2.5 References	80
Chapter 3 Swelling of Liquid Crystal Films	82
3.1 Abstract	83
3.2 Introduction	84
3.3 Experimental	86
3.4 Results and Discussion	88
3.5 Conclusions	101
3.6 References	102

Chapter 4 Swelling of Ionic and Non-ionic Surfactant Micelles by High Pressure Gases 104

4.1 Abstract 105

4.2 Introduction 106

4.3 Experimental 108

4.4 Results and Discussion 110

4.5 Conclusions 127

4.6 References 128

Chapter 5 Time resolved SAXS Studies of Periodic Mesoporous Organosilicas in Anodic Alumina Membranes 132

5.1 Abstract 133

5.2 Introduction 134

5.3 Experimental 136

5.4 Results and Discussion 138

5.5 Conclusions 152

5.6 References 153

Chapter 6 Chemical Modification of Silica Surfaces and their use in the Production of Metallic Nanostructures 155

6.1 Abstract 156

6.2 Introduction 157

6.3 Experimental 161

6.4 Results and Discussion 163

6.5 Conclusions 184

6.6 References 186

Chapter 7 Conclusions 198

Chapter 1

Introduction

1.0 Surface Active Agents

A surfactant molecule is composed of two different parts which possess dissimilar properties, usually a polar, water soluble component attached to a non-polar, water insoluble component [1]. This makes the molecule amphiphilic. Soaps, detergents, long chain alcohols and lipids can all be classified as amphiphilies or surfactants. They are surface active, which means they can stabilise the interface between different phases (for example liquid-liquid or liquid-gas) by reducing surface tension of a single phase (at the surface of water for example) or reducing the interfacial tension between two immiscible phases (polar and non-polar solvents for example). Under certain conditions (elevated surfactant concentration and elevated temperature) the interfacial stabilisation results in a complete coating of the interface with surfactant molecules and the aggregation of surfactant molecules occurs. The resulting entities are called micelles and the concentration and temperature at which micelles form is called the critical micelle concentration (CMC) and the critical micelle temperature (CMT) respectively [2]. Micelles exist along with free surfactant monomers in an equilibrium state, with free surfactant monomers constantly being adsorbed on and desorbed from the micelles. The driving force behind micelle formation in an aqueous surfactant solution is the reduction of unfavourable interactions between the hydrophobic (or lipophilic) segments of the surfactant with water, which leads to the formation of hydrophobic domains within the core of the micelle, while on the exterior of the micelle hydrophobic segments remain in contact with water, see the diagram in Figure 1.1.

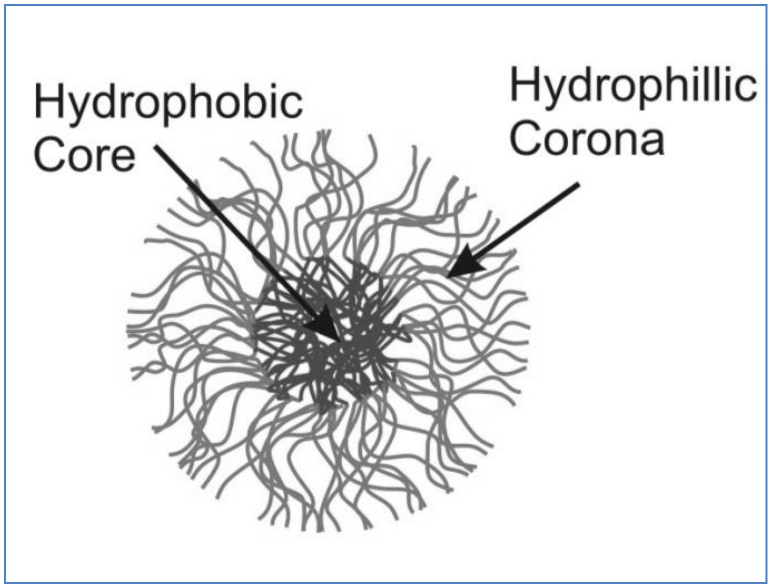


Figure 1.1 A schematic of an ABA tri-block copolymer micelle with a hydrated hydrophilic corona and a hydrophobic micelle core.

There are many different types of surfactant molecules, including large molecular weight non-ionic di- and tri-block copolymers and smaller molecular weight ionic molecules. The most common type of surfactant used in the work reported in this thesis was the Pluronic© range of tri-block copolymer surfactants. At low concentrations these surfactants exist only as monomers in solution. For block copolymers the term unimers is used to avoid any confusion with single polymer segments. The term micelle and aggregate are used interchangeably and refer to the entity present in a surfactant solution. The strength of interaction between the surfactant units with other surfactant units and the strength of interaction between surfactant segments with the solvent, dictates what type of aggregation conformation will be present [3].

A simple example of micelle formation is an ionic surfactant molecule with a charged polar head group and non-polar hydrocarbon tail in an aqueous solution. The interactions between the non-polar tail of the surfactant molecule and water are unfavourable, so the surfactant molecules will form aggregates of spherical micelles. Micelles are formed because the solvent is "good" for one segment but "poor" for another. Surfactants with a hydrocarbon tail require a minimum of eight CH_2 groups to associate into a hydrocarbon phase which is able to overcome the repulsion felt between the charged polar head groups of the surfactant head group [4].

1.1 Non-Ionic Surfactants

1.1.1 Pluronic Surfactants

Pluronic surfactants are either di-block or tri-block copolymers with different repeat units, as shown in Figure 1.2. The repeat units which make up di-block or tri-block copolymer surfactants can be a number of different polymers, examples of polymer segments are polypropylene oxide (PPO), polyethylene oxide (PEO also called polyethylene glycol, PEG), polybutylene oxide (PBO), polybutadiene (PB) or polystryrene (PS). Mostly tri-block copolymer surfactants are made up of the hydrophobic PPO and the hydrophilic PEO.

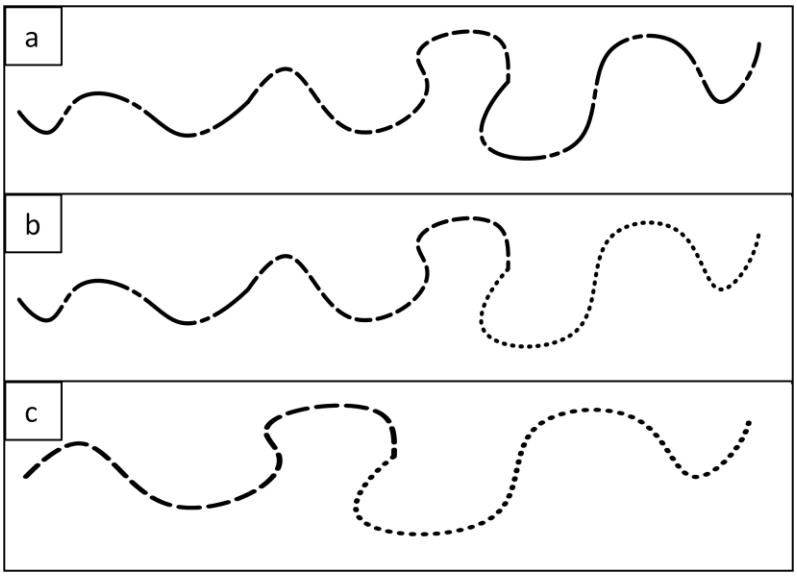


Figure 1.2 An ABA tri-block copolymer (a), an ABC tri-block copolymer (b) and an AB di-block copolymer (c). Each block can be a variety of different polymer blocks [5].

The PEO blocks are soluble in polar solvents due to hydrogen bonding interactions between the polar solvent molecules and the terminal alcohol groups on the PEO segment and the hydrogen bonding of a water molecule to two ether oxygens on the PEO backbone [6, 7]. It is these interactions that are missing on the PPO segments and steric considerations that make PPO more soluble in non-polar solvents. This dual character of the Pluronic surfactant makes them active at the interfaces, *e.g.* at the water and air interface. The molecular structure of Pluronic surfactants is shown in the Figure 1.3.

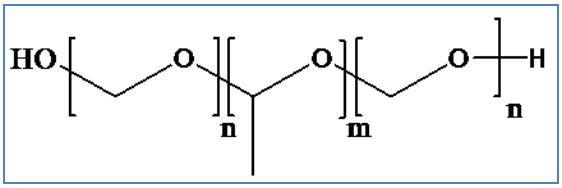


Figure 1.3 Molecular structure of the Pluronic back-bone. Examples of Pluronic surfactant are P123 ($PEO_{20}PPO_{70}PEO_{20}$), F127 ($PEO_{100}PPO_{65}PEO_{100}$) and L62 ($PEO_6PPO_{35}PEO_6$). The "F", "P" and "L" notation refers to the physical state of the surfactant, F referring to flakes, P refers to paste and L refers to liquid. The different ratios of hydrophilic PPO and hydrophobic PEO give the surfactants different properties and vary their association behaviour [8].

1.1.2 Brij Surfactants

The Brij class of non-ionic surfactants are very similar to the Pluronic range of surfactants. They consist of a hydrophobic PEO group and a non-polar long alkane chain, *e.g.* $C_{16}H_{33}$ $(PEO)_{10}H$ as shown in Figure 1.4 [9]. These surfactants aggregate in the same manner as the Pluronic surfactants, with the PEO segment soluble in polar solvents and the non-polar hydrocarbon chain soluble in non-polar solvents.

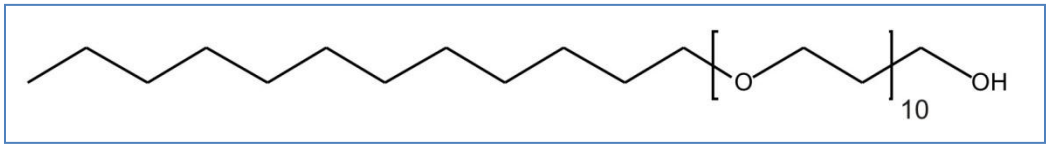


Figure 1.4 The molecular structure of the Brij 56 molecule.

1.2 Ionic Surfactants

1.2.1 Hexadecyltrimethylammonium Bromide

A commonly used cationic surfactant is hexadecyltrimethylammonium bromide (CTAB) and is composed of a large amine head group and a long (C_{16}) hydrocarbon tail group, see Figure 1.5. There are a few variations of the CTAB molecule which make use of different counter ions, for example, CTACl [10]. Various hydrocarbon chain lengths also exist, for example dodecyltrimethylammonium bromide (DTAB) which is composed of a C_{12} hydocarbon chain [11]. Other popular ionic surfactants are sodium dioctylsulfosuccinate (Aersol OT or AOT) [12] and sodiumdecyl sulphate (SDS) [13].

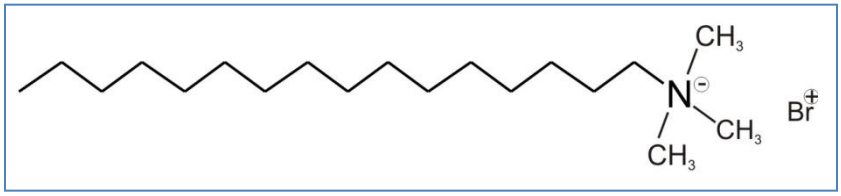


Figure 1.5 Molecular structure of the CTAB molecule

1.3 Micelle Formation

The formation of micelles in a surfactant solution is governed by different factors, the most notable being the critical micelle concentration (CMC) and the critical micelle temperature (CMT), but also the solvent polarity and the presence of additives such as salts or co-surfactants [14, 15]. The sudden appearance of micelles in solution, upon reaching the CMC is accompanied by an increase in the turbidity of the micellar solution, the result of the scattering of light by the

newly formed micelles. The CMC indicates the threshold concentration of surfactant in solution needed to form micelles. Below this limit at a constant temperature micelles are not seen. Above this limit, surfactant molecules aggregate and micelles are formed, see Figure 1.6. The effect of temperature on the formation of micelles is a reflection of the solubility of different parts of the surfactant molecule in the solvent. As the temperature of the solution is increased it is usual for the CMC to decrease. Micelles sizes are normally in the range of 1 to 10 nm, with the large tri-block copolymer surfactants being some of the biggest. The number of surfactant monomers that self organise into micelles is known as the aggregation number and varies between micellar systems. Surfactants are used as structure directing agents (SDAs) in the biomimetic process of synthesising inorganic materials with nanometre dimensions [16], such as in the synthesis of mesoporous materials, most notably the production of mesoporous silica materials [17]. The ability of surfactant molecules to accurately reproduce the same structure under identical experimental conditions and their easy removal from the final mesoporous material is a major benefit during the synthesis of these materials.

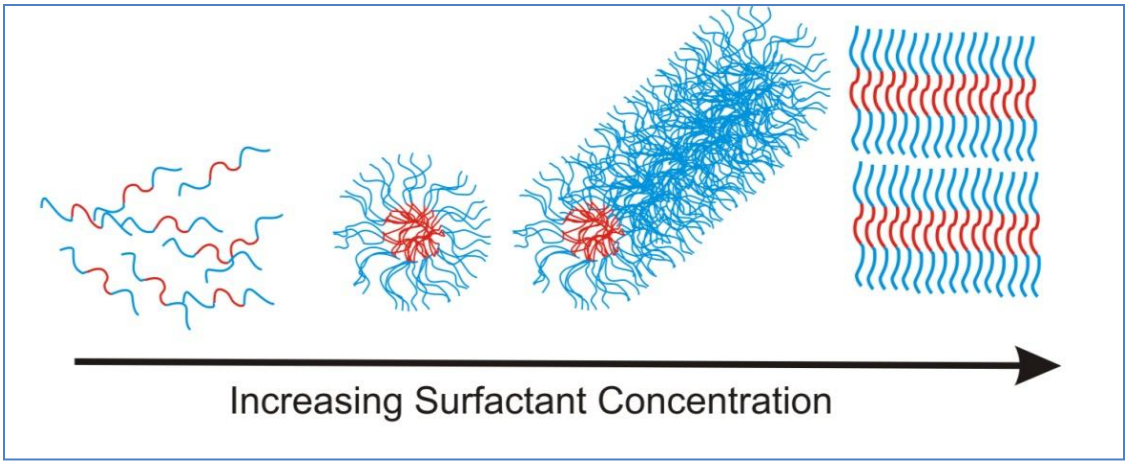


Figure 1.6 Increasing the concentration of the surfactant in solution leads to the formation of micelles of varying shapes. From left to right, surfactant monomers, spherical micelles, rod shaped micelles and finally lamellar shaped micelles.

1.4 Liquid Crystals

The liquid crystal (LC) state, or the mesogenic state, is one that has characteristics of both the liquid state and the solid state. In the liquid state molecules move about randomly and are not aligned in a common direction or along a common axis. However molecules in the crystal state are held rigid in a lattice and have little chance of moving about [18]. Liquid crystals have characteristics of both these states. As observed from the liquid crystals reported in Chapter 3 a high degree of ordering is present, even though the liquid crystal sample can still flow somewhat like a highly viscous liquid. The micelles present in a liquid crystal disperse much like a liquid but retain some semblance of rigidity, either in orientation or position. Surfactants in high enough concentrations form liquid crystals which are composed of micelles of regular shapes arranged in the lowest energy conformations [19].

Investigation of liquid crystals and their applications has become an important research area, with chemists exploiting the supramolecular ordering of liquid crystals to create novel nanoscale materials. Of particular importance is the liquid crystal templating of nanoporous materials, such as the mesoporous silicates like MCM [20], SBA [21] and MSU [22]. Ionic surfactants and non-ionic polymer liquid crystal templates are used in the synthesis of high quality mesostructured materials due to their supramolecular templating ability [23]. Many authors have reported the successful use of short chain ethylene oxide surfactants [24] and tri-block copolymer surfactants containing poly(ethylene oxide) (PEO) and poly(propylene oxide) (PPO) segments [21, 25-27] in the synthesis of mesoporous materials.

Liquid crystals also have the ability to absorb significant amounts of an appropriate solvent and consequently swell [28, 29]. Alexandrisdis *et al.* demonstrated the swelling of up to 20% of Pluronic liquid crystals templated form P105 using glycols [30]. Swollen liquid crystals (SLCs) have recently been utilised as templates for synthesising nanoscale materials, such as zirconia nanoneedles [31] and platinum nanoparticles [32]. In some cases the liquid crystal can easily be removed from the final material by destabilising the SLC and washing with suitable solvents. Work by dos Santos and co-workers [33] has demonstrated the stability and dexterity of SLC templates over a wide range of pH values and compositions. Further application of liquid crystal templating have been reported by Lubeck *et al.* [34] who used Brij 97 liquid crystals as a template to produce CdS nanostructures and Karanikolos *et al.* used a P105 liquid crystal templated to direct the formation of ZnSe nanostructures [35].

Conventional swelling of liquid crystal templates with non-polar solvents requires careful consideration of many factors in order to maintain a stable liquid crystal that retains its shape. Factors include the ionic strength of the solvent when swelling ionic surfactants, pH, temperature and the use a co-surfactant to accomplish the swelling of the liquid crystal. To successfully swell the hexagonal phase of sodium dodecylsulphate (SDS) Ramos *et al.* [36] had to monitor the oil content of the liquid crystal solution and ionic strength of the swelling solvent, and use a co-surfactant to obtain the required template. In the study by Nagarajan *et al.* [37] swelling of Pluronic aggregates resulted in sphere to rod to lamellae micelle shape transitions as a result of hydrocarbon swelling.

However an alternative solvent which does not require the considerations mentioned above is available. Hanrahan *et al.* have demonstrated that supercritical carbon dioxide (sc-CO_2) can be easily utilised to swell liquid crystal templates during the production of mesoporous silica materials [38, 39]. In those studies it was found that swelling (increasing the distance between hexagonal micelle rods and the resulting pore-to-pore spacing of the mesoporous silica) with sc-CO_2 was easily achieved without any loss of ordering, *i.e.* there was no cylinder "wandering" observed, as opposed to when conventional solvent swelling techniques are used where increased inter-cylinder distance becomes too large (relative to cylinder radius) to retain the long range hexagonal ordering.

1.5 Applications of Surfactants

Pluronic amphiphilic block copolymers have become extensively used in a wide range of applications in recent years. They have found uses as detergents [40, 41], in separation applications

[42, 43], drug solubilisation and delivery [44-46], water treatment [47] and the controlled release of drugs [48-50]. The ionic surfactant CTAB has also been widely studied in the past because of its use as templates in mesoporous silica synthesis [51, 52], as a detergent [40], in stabilising nanoparticles [53, 54] and CTAB has also found applications in separation science[55].

One of the more widely studied areas in which micelles are employed is their use in the synthesis of mesoporous materials. In 1990 it was demonstrated by Mobile Oil Corporation scientists that by exploiting the templating action of cationic surfactants and choosing the correct silica precursor with the proper reaction conditions, a new class of molecular sieves could be synthesised. Mesoporous silica with a narrow pore size distribution and extremely large surface area was produced [20]. This material was designated as MCM (Mobile Composition of Matter) and used the templating ability of a cationic surfactant liquid crystal. Further research has investigated other routes to produce mesoporous silica, most importantly breakthroughs made by Stucky and co-workers, who used block copolymers in low concentration to direct the production of mesoporous materials [56].

A characteristic of many micelle systems is their ability to uptake large amounts of a solvent and consequently swell in size. There have been many studies in the past which have investigated the solubility of various hydrocarbons, alcohols and other additives in micellar systems and the consequential swelling of the micelle by their addition. Below are a few examples of such solubility/swelling reports. The solubility of various low molecular weight hydrocarbons in the anionic sodium dodecylsulphate (SDS) surfactant has been reported by Chen *et al.* [57] and Ownby *et al.* [58]. Ruggles *et al.* [59] investigated the changing unit cell dimensions of a 2 dimensional

hexagonal mesoporous silica thin film templated from CTACl micelles after the addition of high molecular weight (C_8 to C_{16}) hydrocarbons during the synthesis of the silica.

Shrestha *et al.* [60] showed the swelling of a non-ionic glycerol (C_{12}) monolaurate in different non-polar solvents, such as cyclohexane, decane, tetradecane, *etc*. Ma *et al.* [61] investigated the micellisation of the Pluronic P85 in the presence of different oils; it was found that the critical micelle temperature of the P85 decreased with the increasing oil concentration. Also in the Ma *et al.* study the core of the micelles was observed to swell significantly at low oil concentrations. ChilluraMartino *et al.* [62] presented a very good study which showed the versatility of SANS in the study of various polymers (poly(1, 1-dihydroperfluorooctyl acrylate), poly(hexafluoropropylene oxide) and poly(dimethyl siloxane)) in supercritical carbon dioxide. Friman *et al.* [63] used small-angle x-ray scattering to investigate the micellisation of sodium octanoate in the presence of octane-1,8-diol which was found to penetrate into the hydrocarbon core of the micelle and cause the micelle to swell considerably.

Swollen micelles are usually employed to produce a material with the inverse structure of the micelle system itself. Below are a number of examples where swollen micelles have been used in the past to produce a novel material. Cao *et al.* [64] enlarged the pores of SBA-15 mesoporous silica templated from the Pluronic P123 by adding 1,3,5-triethylbenzene or 1,3,5-triisopropylbenzene during the synthesis of the mesoporous silica. 1,3,5-trimethylbenzene was used to swell the pores of a cubic mesoporous organosilica in Zhou *et al.* [65] and it was found that the resulting cubic periodic mesoporous organosilica possessed enlarged pore diameters. Investigating the swelling of various Pluronic micellar solutions (including P123, L64 and F68)

using tributylphosphate (TBP) was undertaken by Causse *et al.* [66] and it was found that TBP had an affinity for the hydrophobic core of the Pluronic micelles. Addition of trimethylbenzene (TMB) during the synthesis of mesoporous silica was also seen to result in mesoporous silica with enlarged pores by Chen *et al.* [67].

The addition of the swelling agent triisopropylbenzene during the synthesis of CTAB-templated mesoporous silica was investigated by Fukuoka *et al.* [68], who reported a swollen 2 dimensional hexagonal system; with increasing amounts of triisopropyl benzene during synthesis a phase change from 2 dimensional hexagonal to a cubic system was observed. Blin *et al.* [69] studied the affect of alkane addition to the synthesis of CTAB-templated mesoporous silica, decane was found to be the most successful swelling agent of CTAB in that study.

1.6 Pluronic Surfactants used in the Production of Mesoporous Silica

1.6.1 Self Assembly Strategy and Liquid Crystal Templating Strategy

The self assembly mechanism for the low surfactant concentration synthesis of mesoporous silica involves individual micelles and the inorganic precursor forming a composite [70]. These composites aggregate and phase separation leads to local areas of liquid crystalline concentrations. Polymerisation and condensation of the inorganic species completes the mesostructure and removal of the surfactant template produces the final product. Using a liquid crystal templating route requires the surfactant to be in higher concentrations than those used in the self assembly strategy. Once in a liquid crystal state the final mesostructure is already

present. The inorganic precursor is then incorporated into the liquid crystal template and condenses to the final mesostructured product [71]. Again once the surfactant template has been removed the final framework remains. See the schematic in Figure 1.7.

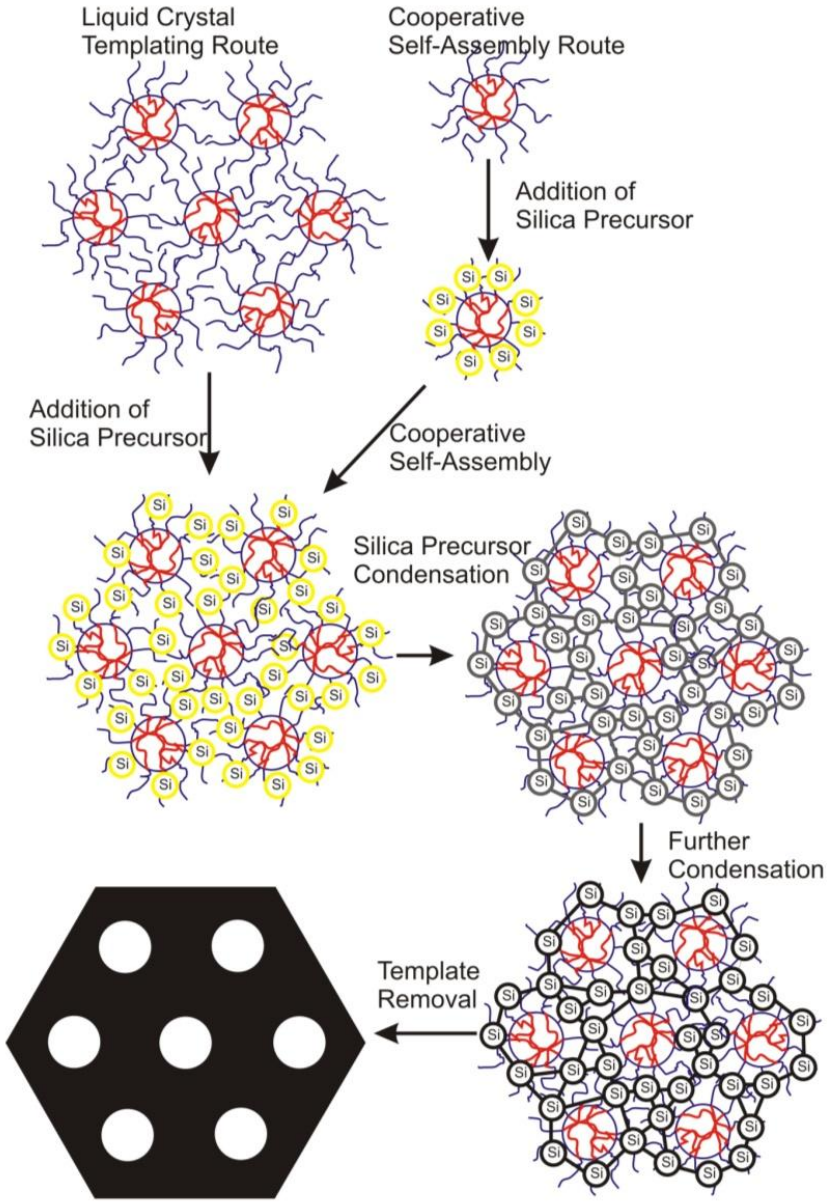


Figure 1.7 Schematic showing the two recognised templating routes in the production of mesoporous silica; the liquid crystal templating route and the cooperative self-assembly route [72].

1.6.2 Mesoporous Silica

Materials with mesoporous properties and physical characteristics have been known for quite some time in one form or another. Zeolites were the first known type of periodic porous material with a well ordered microporous cage structure and crystalline aluminosilicate network [73]. Zeolites have pore diameters typically less than 2 nm, which means that these pores can be easily blocked limiting their use in a number of applications [74]. Other examples of porous materials are metal oxide pillared interlayered clays [75] that are essentially metal oxide pillars supporting the layers of mineral clays, such as montmorillonite [76], beidellite [77, 78] or saponite [79]. These pillars result in the microporous structures that have larger pore diameters compared to zeolites, but the pore dimensions are still in the microporous region, *i.e.* sub 2 nm. Pillared clays have found greater uses than zeolites, due to their larger pore openings, but they have a lower thermal stability [80]. Porous glasses and gels were also known, but these lacked pore ordering and have large pore size distribution [81]. Pores sizes are divided into three size classes, the IUPAC definition is as follows; micropores are less than 2 nm, mesopores are between 2 and 50 nm and macropores above 50 nm [82].

With the discovery of MCM-41, the first well ordered mesoporous system with a well ordered pore system and narrow pore size distribution was available for various applications. The Mobile Corporation patented this porous material in 1991, but a patent for the synthesis of low density silica was filed in 1963, a material which had identical properties to the MCM type of materials but these properties were not revealed at the time. Many other types of mesoporous materials such as the SBA (Santa Barbara Amphorous), discovered in the laboratories of Brad Chmelka and Galen Stucky in Santa Barbara in 1997, have also been heavily researched [56, 83].

SBA-n (n = 15 [84, 85], 16 [86], 1 [87], 2 [88]) materials are made by the characteristic low weight percentage use of structure directing agent (typically below 10 wt%), where as the MCM-type materials use much larger percentages of SDA (up to 40 and 50 wt%). Mesoporous materials that use a low wt% of SDA is thought to follow the cooperative self-assembly method of formation whereas materials synthesised from larger wt% of SDA are thought to follow the liquid crystal method of formation. Other types of mesoporous materials have also been reported in recent years, such as FDU silicas that use a poly-butylene triblock copolymer during its synthesis [89] and CMK materials that are the carbon analogues of porous silica, produced using existing porous silica materials as templates [90]. Ordered mesoporous materials have attracted considerable interest due to their potential applications in areas such as catalysis [91-93], nano-electronics [56, 94, 95] and polymer mesofibers [96, 97]. In particular, the highly ordered and size-tunable channels within ordered mesoporous materials (OMMs) make them ideal host for the encapsulation of nanomaterials [98-100], i.e. nanoparticles [101-104], nanowires [105-107] and carbon nanotube networks [108].

During the production of mesoporous silica such as SBA-n (n = 11 [56], 12 [56], 15 [109] and 16 [56]) and KIT-n (n = 5 [110] and 6 [111]) the mechanism of formation is thought to follow $S^0H^+X^-I^+$, where S^0 is the non-ionic surfactant, I^+ is the silicate species and X^- is the acid counter ion (which is thought to provide electrostatic shielding and enough hydrogen bonding between the micelle and the silica precursor [21, 112]). The self assembly is driven by the electrostatic Coulombic force and hydrogen bonding between the surfactant PEO corona and the pre-condensed silica species which results in pseudo-hydration of the Pluronic surfactant corona. Further condensation of the silica precursor results in the polymerisation and cross linking of the silicate species in the PEO

corona and leads to a surfactant-silica composite, see Equations 1.1 and 1.2 below. The inorganic precursor at the surfactant-inorganic interface polymerises and cross links resulting in a formation of the porous structure.

$$Si(OC_2H_5)_4 + 4H_2O \xrightarrow{H^+/OH^-} Si(OH)_4 + 4C_2H_5OH \qquad 1.1$$

$$Si(OH)_4 \xrightarrow{H^+/OH^-} SiO_2 \downarrow + 2H_2O \qquad 1.2$$

The inorganic mesostructured material is then obtained by simply removing the organic surfactant. Ordered mesoporous materials like those discussed above and those produced during this project possess large uniform pore sizes (7-10 nm) with narrow pore size distribution and extremely large surface areas (< 600 $m^2 g^{-1}$).

MCM-41 has a honeycomb type 2-dimensional hexagonal pore structures, but there exists many other types of structure. MCM 48 is a cubic system, which consists of 2 interwoven worm hole pore systems, sometimes known as "plumber's nightmare", but with cubically aligned pore entrances [113]. MCM 51 is a lamellar-type structure that consists of silica layers, but is structurally unstable as the sheets collapse upon the removal of the structure directing agent. The type of inorganic materials which can be used as the mesoporous framework include silica, other non-silica metal oxides [114], metal sulphides [115], metals [116] and carbons [117, 118].

The inorganic framework in mesoporous silica is mostly made up of individual SiO_4 units, however at the surface there are three connected and even two connected SiO_4 units which create hydrophilic terminal hydroxyl groups (Si-OH) [72].

1.6.3 Periodic Mesoporous Organo-silicas

Periodic mesoporous organosilicas (PMOs) are an attractive class of ordered mesoporous materials consisting of hybrid structural units, *i.e.* -[$_{1.5}$OSi-R-SiO$_{1.5}$]- (where R is a bridged group, such as -CH_2CH_2-, -CH=CH-, or phenyl), where the inorganic and organic moieties in the structure are covalently linked to each other [119-123]. PMO materials offer novel porous structures with different chemical characteristics to the traditional inorganic-based mesoporous materials. These materials combine the rigidity of the silica framework with the added functionality of the organic counterpart. The organo-silica functionality is generated during the initial synthesis of the material by hydrolysis of an appropriate organo-silica precursor which results in the formation of a material with a repeating organic bridging unit [124]. Examples of the synthesis of PMO materials, including one of the first reported synthesis of a PMO material by Inagaki *et al.* [125], who reported the basic synthesis of an ethane-bridged PMO using the surfactant octadecyltrimethyl ammonium chloride (ODTMA). Another early investigation into the synthesis of PMO materials was carried out by Asefa, *et al.* [126] in which cetyltrimethylammonium bromide (CTAB) was used in the production of an ethane-bridged PMO. Another versatile synthesis route in the production of PMO materials was researched by Liang *et al.* [127] who used a mixture of the Gemini surfactant $[CH_3(CH_2)_{17}NMe_2(CH_2)_3NMe_3]^{2+}$

$2Br^-$ and CTAB to produce an ethane bridged PMO material with relatively poor long range order, but a PMO material none the less.

PMOs have found use in a wide range of applications including catalysis [128], chromatography [129] and as high-k dielectrics [130], as reviewed by Wight *et. al.* [131] and Hoffmann *et. al.* [132]. PMO materials have much more applications than their completely inorganic analogues due to their increased reactivity. For HPLC applications Rebbin *et al.* [133] produced near ideal ethane-bridged PMO spheres, with a narrow size distribution. Due to their reactivity, PMO materials can act as great adsorbent materials for different substances. Lee *et al.* [28] used PMO materials as an anion exchange resin, which removed ions like perrhenate, perchlorate and pertechnetate using a complex ammonium group in the framework of ethane and benzene-bridged PMO materials. Also PMO materials have been used as templates for the production of novel nanoscale materials, such as pure Pt and Rh nanostructures and mixtures of each by Fukuoka *et al.* [134]. These materials were grown inside ethane-bridged PMO materials, the resulting nanowires produced had a necklace morphology, which was thought to be due to the interaction of the metallic nanowire precursor with the periodic ethane bridges in the PMO pore walls.

Further chemical functionalisation of PMOs (or any other silica material) post synthesis is achieved by reaction of organo-silanes with surface silanol groups which leads to functionalised PMO materials [135]. There is a wide range of functionalisation possibilities due to the comprehensive range of organo-silanes now available, including 3-glycidoxypropyl trimethoxy silane and 3-aminopropyl trimethoxy silane. The variety of functionality is limited only by the availability of stable organosilanes. On a silica surface the majority of species exist as tetragonal

SiO_4 units, however there also exists three connected and two connected SiO_4 units which are terminated by silanol groups (Si-OH). These hydroxyl groups are responsible for the hydrophobic surface of the material. The population of these hydroxyl groups varies with relative humidity and during calcination they are completely removed only to reappear under conditions of high humidity [136]. The number of hydroxyl groups can be increased by treating the silica surface with a H_2O_2 solution. The surface hydroxyl groups act as reaction centres for the functionalisation of the silica surface with organic groups.

1.6.4 Periodic Mesoporous Organo-silicas in Confined Architectures

Thin films of PMO materials have also been prepared by the deposition of suitable gels onto substrates, for example Wu *et al.* [137] have reported the production of PMO thin films on silicon substrates. The formation of mesoporous materials within the confined architecture of a structured template, for example anodic alumina membranes (AAMs) [138, 139], provides a unique opportunity to spatially align the mesopores in a particular orientation due to the directional alignment of the pores within the template. Similar mesoporous silica filaments were reported by Huo *et al.* in 1997 [140]. Two common mesoporous structures have been identified within the confines of AAMs: (i) circular hexagonal – where the mesopores wind around the main axis of the AAM channels and (ii) columnar hexagonal – where the mesopores run parallel to the main axis of the AAM channels. Recently another confined mesoporous structure has been postulated, *i.e.* a lamellar structure which is composed of concentric silica sheets [141]. There have been reports of the use of such materials in the literature including the use of mesoporous silica in

AAMs as templates during the synthesis of carbon filaments [142] and the use of mesoporous silica filaments in controlled drug delivery [143, 144].

The analysis of PMO filaments confined with the porous structure of AAMs has also been studied in the past, most recently using small-angle x-ray scattering (SAXS) and transmission electron microscopy (TEM) by Keilbach *et al.* [145]. Electrophoretic deposition of PMO materials within AAM channels was investigated by Hill *et al.* [146] and deposition using a PMO gel with two different structural directing agents was reported by Lee *et al.* [147]. Ku *et al.* [148] and Lai *et al.* [149] both reported the deposition of various mesoporous materials within the channels of AAMs and the growth of nanowires within the pores of mesoporous silica confined within the channels of AAM was reported by Petkov *et al.* [150]. Marlow *et al.* also studied circular mesoporous silica filaments synthesised in the absence of an AAMs using SAXS [151].

1.7 Small-Angle Scattering

Small-angle scattering of radiation (x-rays, neutrons or light) is one of the most widely used techniques in the analysis of dispersed particles. All SAS techniques involve the scattering of radiation from particles, be it visible light, x-rays or neutrons. Depending on the radiation wavelength used different length scales are investigated. Powerful synchrotron and neutron sources combined with very sensitive detectors and CCD cameras have made SAS one of the best techniques that can be used in the analysis of dispersed systems in solution. The SAS technique needs a mono-dispersion of particles, for example macro-molecules or solid particles.

1.7.1 Small-Angle X-ray Scattering

Small-angle x-ray scattering (SAXS) is a very powerful technique used to investigate a wide range of different systems. Some examples SAXS studies are Viswanatha *et al.* Who studied the growth of CdS and ZnS semiconducting nanocrystals [152], SAXS analysis of mesoporous monoliths was conducted by Malfatti *et al.* [153], and the analysis of Eu_2O_3 mesoporous films by Castro *et al.* [154]. The incident high intensity monochromatic hard x-rays are produced by synchrotron radiation and are scattered by the electrons in the sample under investigation, more scattering occurs from atoms with increased number of electrons (increasing Z number). This results in an observable contrast between different atoms, molecular domains or elemental density present in the sample. The scattered x-rays are recorded on a CCD camera situated at the end of an evacuated tube. A beam stop prevents saturation of the CCD detector with incident x-rays. The scattering from a size-monodispersed sample of suspended particles results in isotropic scattering rings which are recorded by the CCD camera. The scattering x-rays have been scattered through an angle determined SAXS scattering vector. The scattering vector, Q for SAXS is given by equation 1.3:

$$Q = \left(\frac{4\pi}{\lambda}\right)\sin\left(\frac{\theta}{2}\right) \qquad 1.3$$

Where θ is the angle at which the x-rays have been scattered and λ is the wavelength of radiation used. Synchrotron radiation has a wavelength which is determined by the energy of the x-rays available. SAXS experiments which were conducted in this project were carried out at the

Austrian Institute of Biophysics and Bio Systems Research funded SAXS beam line at the Elettra synchrotron in Trieste, Italy.

1.7.2 Synchrotron Radiation

Synchrotron is a type of particle accelerator which is designed to emit radiation, unlike a particle accelerator which does not emit light. A synchrotron produces radiation of high energy that can be used in the study a wide range of fields, including chemistry, biology and medical sciences.

The synchrotron principle is based on the fact that charged particles travelling at very high speeds (close to the speed of light) emit radiation [155]. In a synchrotron, electrons are accelerated firstly in a static electric field linear accelerator (LINAC) to a few MeV and then injected into a storage ring. In the storage ring radio frequency emitters oscillate at a frequency that is in phase with the electrons already accelerated by the LINAC and accelerates the electrons further. The storage ring is a tube under extreme vacuum. In the storage ring strong magnetic fields perpendicular to the ring change the direction of the electrons. The charged particles experience a Lorentz force that focuses their trajectory toward the centre of the ring, causing their curved path. Increasing the magnitude of the magnetic field increases the bending effect felt by the electron. Once passed the bending magnet the electron continues along a straight line trajectory. Therefore the ring is not necessarily a "ring" but rather a series of bends with as many straight sections.

The ring is housed inside thick concrete shielding to contain the radiation. It is the size of the ring and the power of the magnetic fields that governs the highest possible energy a synchrotron can achieve. Along with bending magnets there are also focussing magnets that are placed between the bending magnets. These are 4-pole or 6-pole magnets that focus the beam so it stays in its trajectory, much like a lens for visible light. Every time the electron trajectory is changed it loses energy in the form of radiation, so bending magnets also serve as radiation emission points that supply the beam lines with the necessary radiation.

1.7.4 Small-Angle Neutron Scattering

Neutrons are scattered by the nucleus of an atom, but unlike x-rays, the amount of scattering is not dependent on the number of neutrons present in the nucleus but on the sum of the scattering lengths and scattering length densities (SLD) [156]. The SLD of a molecule is a function of (i) the bulk density of the material, (ii) the molecular weight of the material and (iii) the coherent neutron scattering length of the different nuclei present in the scatting particle. There is very little contrast seen between domains with similar SLDs. For example, the polyethylene oxide (PEO) blocks and polypropylene oxide (PPO) blocks of a di-block polymer have very similar scattering length densities and it is impossible to distinguish between them. However, due to the fact that PEO is hydrated with H_2O in an aqueous solution means that it is possible for the SANS technique to distinguish between hydrated PEO and dry PPO [157]. One of the benefits of neutron scattering is that neutrons are scattered differently by isotopes of the same element. The most striking difference is the different scattering cross sections seen by hydrogen and deuterium [156]. Hydrogen scatters neutrons differently than deuterium; it is this reason why in some spallation

sources liquid H_2O is used as a moderator around the spallation target. Background signals are always present in SANS instruments due to cosmic and facility background and electronic noise.

The wavelength of neutrons used in a SANS measurement (0.15nm-2.5nm) is much larger than the size of a nucleus, so the nucleus acts like a point scatterer. SANS has the advantage over other types of scattering techniques that as the angle of scattering increases the intensity of the scattered neutrons is not lost. With other small-angle scattering techniques a loss of intensity of the scattered radiation is seen as the angle of scatter is increased. SANS is a technique that is also widely used in the analysis of different materials, including the investigation of water-in-CO_2 microemulsions using non-fluorinated surfactants [158-161], and much work has been carried out on alloys, ceramics and composite materials [162]. SANS determination of the temperature induced swelling of high concentrations of the Pluronic surfactant F127 micellar solutions was investigated by Lenaerts *et al.* [163]. O'Driscoll *et al.* [164] used SANS measurements to determine the meso-structure of cetyltrimethylammonium bromide/polyethylenimine polymer films after the incorporation of small organic molecules into the polymer films. It was seen in that study that cyclohexane and decane could evenly swell the structure of the film and that cyclohexane swelling of the prolate elliptical CTAB micelles extended the main axis of the micelle.

SANS experiments which were conducted for this work were carried out at the LOQ SANS station at the Isis neutron facility at the Rutherford Appleton Labs (RAL) in Oxfordshire in the UK.

1.7.5 Spallation Neutron Sources

Neutrons used at Isis are produced from a process called spallation. Spallation employs high energy protons produced from a LINAC, cyclotron or synchrotron that strike a target. The target can be any nucleus but those of higher elemental weight produce more neutrons. The bombardment of high energy protons at the target causes an inter-nucleus cascade of the now high energy nucleus. In an attempt to regain a lower energy the nucleus emits energy in the form of protons that strike other nuclei and neutrons are produced. For example at ISIS, a tungsten target is used and is struck with protons produced from a LINAC and a synchrotron. This process produces fast neutrons used in different beam lines. Moderators and heavy water are used to slow the fast neutrons to a more usable energy. Neutrons to be used in the different neutron beam lines are channelled down evacuated beam tubes [165]. Depending on the type (thermal/fast neutrons of cold/slow neutrons) of neutrons needed the spallation target with its moderators, reflectors and beam tubes will be laid out in different arrangements to obtain different optimisation. From a spallation source, pulsed neutron bursts are produced as a result of a chopper that cuts out unwanted neutrons, but causes a range of neutrons wavelengths to be used (different wavelengths arriving at the detector at different times). This range of neutron wavelengths has the advantage of not needing a moveable detector, but one with a fixed geometry. This smearing of neutron energies is taken into account during measurements.

1.8 Overview

This thesis will present the structural investigation of a variety of micellar systems under different high pressure environments, the morphology of a porous material in a confined architecture and the use of templates in the production of nanostrucutres.

Chapter 2 describes in detail the sample preparation methods and the experimental techniques used for sample characterisation. Also described are the mathematical models used in the analysis and interpretation of the neutron scattering data from the Pluronic tri-block copolymer F127 and CTAB micelle systems.

Chapter 3 focuses on the changing structural properties of liquid crystal films templated from F127, CTAB and Brij 56, when subjected to high pressure CO_2, sc-CO_2 and propane. Swelling of the liquid crystal films was measured using small-angle neutron scattering (SANS).

Chapter 4 focuses on the structural characterisation of F127 and CTAB micelles in solution when exposed to high pressure gases. This work carries on what was achieved in Chapter 3 but a much more detailed analysis was used. Using a lower concentration of surfactant in solution, the spherical micelles were seen to increase in size as the pressure of the gaseous environment was increased. Like the swelling of liquid crystals in Chapter 3, the degree of micelle swelling was seen to depend on the solubility of the gaseous environment in the micelle. Mathematical models were used to model the neutron scattering from the F127 and CTAB micelles and various micelle parameters were obtained from the best fits of the experimental data.

Chapter 5 explores in the pore morphology of filaments of periodic mesoporous organosilica (PMO) in the pores of anodic alumina membranes (AAMs). The mesoporous filaments were deposited onto the membrane under different drying conditions and precursor gel compositions. Different pore alignments of the filaments as determined from small-angle x-ray scattering (SAXS) and transmission electron microscopy analysis (TEM) resulted from different deposition conditions. A time resolved SAXS measurement was used to map the development of the mesoporous structure as the mesoporous filament formed within the channel structure of the membrane.

Chapter 6 describes the use of PMO materials and polymer thin films in the production of germanium nanostructures from gold seeds. The materials were chemically modified with thiol functionality, which were later used as reduction centres which deposited gold particles on the surface of the polymer template and in the pore structure and on the surface of the PMO the material. The gold nanoparticles then acted as seeds for the catalysed growth of germanium nanowires.

1.9 References

1 Kale, T. S.; Klaikherd, A.; Popere, B.; Thayumanavan, S., *Langmuir* **2009,** *25*, 9660.
2 O'Reilly, R. K., *Philos. Trans. R. Soc. London, Ser. A* **2007,** *365*, 2863.
3 Evans, D. F., *Langmuir* **1988,** *4*, 3.
4 Moulik, S. P., *Curr. Sci.* **1996,** *71*, 368.
5 Alexandridis, P.; Hatton, T. A., *Colloids Surf., A* **1995,** *96*, 1.
6 Breen, J.; Huis, D.; Debleijser, J.; Leyte, J. C., *J. Chem. Soc., Faraday Trans.* **1988,** *84*, 293.
7 Cametti, C.; Dibiasio, A., *Ber. Bunsen. Ges.-Phys. Chem. Chem. Phy.* **1988,** *92*, 1089.
8 Alexandridis, P.; Holzwarth, J. F.; Hatton, T. A., *Macromolecules* **1994,** *27*, 2414.
9 Smarsly, B.; Gibaud, A.; Ruland, W.; Sturmayr, D.; Brinker, C. J., *Langmuir* **2005,** *21*, 3858.
10 Park, S. S.; An, B.; Ha, C. S., *Microporous Mesoporous Mater.* **2008,** *111*, 367.
11 Bahri, M. A.; Hoebeke, M.; Grammenos, A.; Delanaye, L.; Vandewalle, N.; Seret, A., *Colloids and Surfaces a-Physicochemical and Engineering Aspects* **2006,** *290*, 206.
12 Tielrooij, K. J.; Cox, M. J.; Bakker, H. J., *Chemphyschem* **2009,** *10*, 245.
13 Quina, F. H.; Nassar, P. M.; Bonilha, J. B. S.; Bales, B. L., *J. Phys. Chem.* **1995,** *99*, 17028.
14 Vlachy, N.; Drechsler, M.; Verbavatz, J. M.; Touraud, D.; Kunz, W., *J. Coll. Inter. Sci.* **2008,** *319*, 542.
15 Lin, B.; Mohanty, S.; McCormick, A. V.; Davis, H. T., *Mesoscale Phenomena in Fluid Systems* **2003,** *861*, 313.
16 Holmber, K., *J. Coll. and Inter. Sci.* **2004,** *274*, 355.
17 Tanev, P. T.; Pinnavaia, T. J., *Chem. Mater.* **1996,** *8*, 2068.
18 Singh, S., *Physics Report* **2000,** *324*, 107-269.
19 Fritscher, C.; Husing, N.; Bernstorff, S.; Brandhuber, D.; Koch, T.; Seidler, S.; Lichtenegger, H. C., *J. Synchrotron Radiat.* **2005,** *12*, 717.
20 Beck, J. S.; Vartulli, J. C.; Roth, W. J.; Leonowicz, M. E.; Kresge, C. T.; Schmitt, K. D.; Chu, C. T.; Olson, D. H.; Shepard, E.; McMyllen, S. B.; Higgins, J. B.; Schlenker, J. L., *J. Am. Chem. Soc.* **1992,** *114*,
21 Zhao, D.; Feng, J.; Huo, Q.; Melosh, N.; Fredrickson, G. H.; Chmelka, B. F.; Stucky, G. D., *Science* **1998,** *279*, 548.
22 Martines, M. A. U.; Yeong, E.; Larbot, A.; Prouzet, E., *Micro. Meso. Mater.* **2003,** *74*, 213.
23 Flodstrom, K.; Alfredsson, *Micro. Meso. Mater.* **2003,** *59*, 167-179.
24 Attard, G. S.; Glyde, J. C.; Goltner, C. G., *Nature* **1995,** *378*, 366.
25 Huo, Q.; Margolese, D. L.; Ciesla, U.; Demuth, D. G.; Feng, P.; Gier, T. E.; Sieger, P.; Chmelka, B. F.; Schuth, F.; Stucky, G. D., *Chem. Mater.* **1994,** *6*, 1176.
26 Huo, Q.; Margolese, D. L.; Stucky, G. D., *Chem. Mater.* **1996,** *8*, 1147.
27 Zhao, D.; Sun, J.; Li, Q.; Stucky, G. D., *Chem. Mater.* **2000,** *12*, 275.
28 Lee, J.; Choi, S.-U.; Yoon, M.-K.; Choi, Y. W., *Arch. Pharm. Res.* **2003,** *26*, 880.
29 Yusuf, Y.; Ono, Y.; Sumisaki, Y.; Cladis, P. E.; Brand, H. R.; Finkelmann, H.; Kai, S., *Phys. Rev. B* **2004,** *69*, 4-10.
30 Alexandrisdis, P.; Ivanova, R.; Lindman, B., *Langmuir* **2000,** *16*, 3676.

31 Dos Santos, E. P.; Santilli, C. V.; Pulcinelli, S. H.; Prouzet, E., *Chem. Mater.* **2004,** *16*, 4187-4192.
32 Surrendran, G.; Tokumoto, M. S.; Pena dos Sontos, E.; Remita, H.; Ramos, L.; Kooyman, P. J.; Valentim Santilli, C.; Bourgaux, C.; Dieudonne, P.; Prouzet, E., *Chem. Mater.* **2005**, 1505.
33 dos Santos, E. P.; Tokumoto, M. S.; Surendran, G.; Remita, H.; Bourgaux, C.; Dieudonne, P.; Prouzet, E.; Ramos, L., *Langmuir* **2005,** *21*, 4362.
34 Lubeck, C. R.; Han, T. Y. J.; Gash, A. E.; Satcher, J. H.; Doyle, F. M., *Adv. Mater.* **2006,** *18*, 781.
35 Karanikolos, G. N.; Alexandrisdis, P.; Mallory, R.; Petrou, A.; Mountziaria, T. J., *Nanotechnology* **2005,** *16*, 2372.
36 Ramos, L.; Fabre, P., *Langmuir* **1997,** *13*, 682.
37 Nagarajan, R., *Colloid Surface B* **1999,** *16*, 52.
38 Hanrahan, J. P.; Copley, M. P.; Ryan, K. M.; Spalding, T. R.; Morris, M. A.; Holmes, J. D., *Chem. Mater.* **2004,** *16*, 424.
39 Hanrahan, J. P.; Copley, M. P.; Ziegler, K. J.; Spalding, T. R.; Morris, M. A.; Steytler, D. C.; Heenan, R. K.; Schweins, R.; Holmes, J. D., *Langmuir* **2005,** *21*, 4163-4167.
40 Burapatana, V.; Booth, E. A.; Prokop, A.; Tanner, R. D., *Ind. Eng. Chem. Res* **2005,** *44*, 4968.
41 Kristiansen, T. B.; Hagemeister, J. J.; Grave, M.; HellungLarsen, P., *J. Cell. Physi.* **1996,** *169*, 139.
42 Chen, W. J.; Peng, J. M.; Su, Y. L.; Zheng, L. L.; Wang, L. J.; Jiang, Z. Y., *Sep. Purif. Methods* **2009,** *66*, 591.
43 Miksik, I.; Deyl, Z., *J. Chromatogr. B* **2000,** *739*, 109.
44 Oh, K. T.; Bronich, T. K.; Bromberg, L.; Hatton, T. A.; Kabanov, A. V., *J. Controlled Release* **2006,** *115*, 9.
45 Sek, L.; Boyd, B. J.; Charman, W. N.; Porter, C. J. H., *J. Pharm. Pharmacol.* **2006,** *58*, 809.
46 Shaik, M. S.; Haynes, A.; McSween, J.; Ikediobi, O.; Kanikkannan, N.; Singh, M., *J. Aerosol Med.* **2002,** *15*, 261.
47 Hurter, P. N.; Haton, T. A., *Langmuir* **1992,** *8*, 1291.
48 Wei, Z.; Hao, J. G.; Yuan, S.; Li, Y. J.; Juan, W.; Sha, X. Y.; Fang, X. L., *Int. J. Pharm.* **2009,** *376*, 176.
49 Wang, Y. Z.; Li, Y. J.; Zhang, L. J.; Fang, X. L., *Arch. Pharmacal Res.* **2008,** *31*, 530.
50 Sharma, P. K.; Reilly, M. J.; Bhatia, S. K.; Sakhitab, N.; Archambault, J. D.; Bhatia, S. R., *Colloids Surf., B* **2008,** *63*, 229.
51 Han, S.; Hou, W.; Dang, W.; Xu, J.; Hu, J.; Li, D., *Mater. Lett.* **2003,** *57*, 4520.
52 Kim, W. J.; Yang, S. M., *Chem. Mater.* **2000,** *12*, 3227.
53 Moon, S. Y.; Kusunose, T.; Sekino, T., *Mater. Lett.* **2009,** *63*, 2038.
54 Kotkata, M. F.; Masoud, A. E.; Mohamed, M. B.; Mahmoud, E. A., *Physica E* **2009,** *41*, 1457.
55 Zhou, Y. B.; Chen, L.; Hu, X. M.; Lu, J., *Water Sci. Technol.* **2009,** *59*, 957.
56 Zhao, D.; Feng, J.; Huo, Q.; Melosh, N.; Fredrickson, G. H.; Chmelka, B. F.; Stucy, G., *Science* **1998,** *279*, 548.

57 Chen, L. T.; Sun, C. Y.; Nie, Y. Q.; Sun, Z. S.; Yang, L. Y.; Chen, G. J., *J. Chem. Eng. Data* **2009,** *54*, 1500.
58 Ownby, D. W.; King, A. D., *J. Coll. Inter. Sci.* **1984,** *101*, 271.
59 Ruggles, J. L.; Gilbert, E. P.; Holt, S. A.; Reynolds, P. A.; White, J. W., *Langmuir* **2003,** *19*, 793.
60 Shrestha, L. K.; Sato, T.; Aramaki, K., *PCCP* **2009,** *11*, 4251.
61 Ma, J. H.; Wang, Y.; Guo, C.; Liu, H. Z.; Tang, Y. L.; Bahadur, P., *J. Phys. Chem. B* **2007,** *111*, 11140.
62 ChilluraMartino, D.; Triolo, R.; McClain, J. B.; Combes, J. R.; Betts, D. E.; Canelas, D. A.; DeSimone, J. M.; Samulski, E. T.; Cochran, H. D.; Londono, J. D., *J. Mol. Struct.* **1996,** *383*, 3.
63 Friman, R.; Rosenholm, J. B., *Coll. Polym. Sci* **1982,** *260*, 545.
64 Cao, L. A.; Man, T.; Kruk, M., *Chem. Mater.* **2009,** *21*, 1144.
65 Zhou, X. F.; Qiao, S. Z.; Hao, N.; Wang, X. L.; Yu, C. Z.; Wang, L. Z.; Zhao, D. Y.; Lu, G. Q., *Chem. Mater.* **2007,** *19*, 1870.
66 Causse, J.; Lagerge, S.; de Menorval, L. C.; Faure, S., *J. Coll. Inter. Sci.* **2006,** *300*, 713.
67 Chen, D. H.; Li, Z.; Wan, Y.; Tu, X. J.; Shi, Y. F.; Chen, Z. X.; Shen, W.; Yu, C. Z.; Tu, B.; Zhao, D. Y., *J. Mater. Chem.* **2006,** *16*, 1511.
68 Fukuoka, A.; Kikkawa, I.; Sasaki, Y.; Shimojima, A.; Okubo, T., *Langmuir* **2009,** *25*, 10992.
69 Blin, J.; Otjacques, C.; Herrier, G.; Su, B.-L., *Langmuir* **2000,** *16*, 4229.
70 Patarin, J.; Lebeau, B.; Zana, R., *Curr. Opin. Coll. Inter. Sci.* **2002,** *7*, 107.
71 Liu, D.; Lei, J. H.; Guo, L. P.; Du, X. D.; Zeng, K., *Microporous Mesoporous Mater.* **2009,** *117*, 67.
72 Wan, Y.; Zhao, D. Y., *Chem. Rev.* **2007,** *107*, 2821.
73 Catlow, C. R. A.; Bell, R. G.; Gale, J. D.; Lewis, D. W., *Zeolites: A Refined Tool for Designing Catalytic Sites* **1995,** *97*, 87.
74 Davis, M. S., *Nature* **2002,** *417*, 813.
75 Volzone, C., *Microporous and Mesoporous Materials* **2001,** *49*, 197.
76 Kanda, Y.; Iwamoto, H.; Kobayashi, T.; Uemichi, Y.; Sugioka, M., *Top. Catal.* **2009,** *52*, 765.
77 Diaz, M.; Cambier, P.; Brendle, J.; Prost, R., *Appl. Clay Sci.* **2007,** *37*, 12.
78 De Stefanis, A.; Dondi, M.; Perez, G.; Tomlinson, A. A. G., *Chemosphere* **2000,** *41*, 1161.
79 Mata, G.; Trujillano, R.; Vicente, M. A.; Korili, S. A.; Gil, A.; Belver, C.; Ciuffi, K. J.; Nassar, E. J.; Ricci, G. P.; Cestari, A.; Nakagaki, S., *Microporous Mesoporous Mater.* **2009,** *124*, 218.
80 Corma, A., *Chem. Rev.* **1997,** *97*, 2373.
81 Ulrike Ciesla, F. S., *Microporous and Mesoporous Materials* **1999,** *27*, 131-149.
82 K. S. W. Sing, D. H. E., R. H. W. Haul, L. Moscou, R. A. Pierotti, J. Rouquerol, T. Siemieniewska, *Pure Appl. Chem.* **1985,** *57*, 710.
83 Zhao, D. Y.; Sun, J. Y.; Li, Q. Z.; Stucky, G. D., *Chem. Mater.* **2000,** *12*, 275.
84 Luan, Z. H.; Hartmann, M.; Zhao, D. Y.; Zhou, W. Z.; KeVan, L., *Chem. Mater.* **1999,** *11*, 1621.
85 Shin, H. J.; Ryoo, R.; Kruk, M.; Jaroniec, M., *Chem. Comm.* **2001**, 349.

86 Van der Voort, P.; Benjelloun, M.; Vansant, E. F., *J. Phys. Chem. B* **2002,** *106*, 9027.
87 Kruk, M.; Jaroniec, M.; Ryoo, R.; Kim, J. M., *Chem. Mater.* **1999,** *11*, 2568.
88 Perez-Mendoza, M.; Gonzalez, J.; Wright, P. A.; Seaton, N. A., *Langmuir* **2004,** *20*, 9856.
89 Matos, J. R.; Kruk, M.; Mercuri, L. P.; Jaroniec, M.; Zhao, D.; Kamiyama, T.; Terasaki, O.; Pinnavaia, T. J.; Liu, Y., *J. Am. Chem. Soc.* **2002,** *125*, 821.
90 Ryoo, R.; Joo, S. H.; Kruk, M.; Jaroniec, M., *Adv. Mater.* **2001,** *13*, 677.
91 Corma, A., *Chem. Rev.* **1997,** *97*, 2373.
92 Ying, J. Y.; Mehnert, C. P.; Wong, M. S., *Angew. Chem. Int. Ed.* **1999,** *38*, 56.
93 Linssen, T.; Cassiers, K.; Cool, P.; Vansant, E. F., *Adv. Colloid Interface Sci.* **2003,** *103*, 121.
94 Huo, Q. S.; Margolese, D. I.; Ciesla, U.; Feng, P. Y.; Gier, T. E.; Sieger, P.; Leon, R.; Petroff, P. M.; Schuth, F.; Stucky, G. D., *Nature* **1994,** *368*, 317.
95 Tanev, P. T.; Pinnavaia, T. J., *Science* **1995,** *267*, 865.
96 Xiang, S.; Zhang, Y. L.; Xin, Q.; Li, C., *Angew. Chem. Int. Ed.* **2002,** *41*, 821.
97 Kruk, M.; Jaroniec, M., *Chem. Mater.* **2001,** *13*, 3169.
98 Moller, K.; Bein, T., *Chem. Mater.* **1998,** *10*, 2950.
99 Moller, K.; Bein, T.; Fischer, R. X., *Chem. Mater.* **1998,** *10*, 1841.
100 Bronstein, L. M., *Colloid Chemistry 1* **2003,** *226*, 55.
101 Zhang, W. H.; Shi, J. L.; Wang, L. Z.; Yan, D. S., *Mater. Lett.* **2000,** *46*, 35.
102 Zhang, W. H.; Shi, J. L.; Wang, L. Z.; Yan, D. S., *Chem. Mater.* **2000,** *12*, 1408.
103 Parala, H.; Winkler, H.; Kolbe, M.; Wohlfart, A.; Fischer, R. A.; Schmechel, R.; von Seggern, H., *Adv. Mater.* **2000,** *12*, 1050.
104 Winkler, H.; Birkner, A.; Hagen, V.; Wolf, I.; Schmechel, R.; von Seggern, H.; Fischer, R. A., *Adv. Mater.* **1999,** *11*, 1444.
105 Brieler, F. J.; Grundmann, P.; Froba, M.; Chen, L. M.; Klar, P. J.; Heimbrodt, W.; von Nidda, H. A. K.; Kurz, T.; Loidl, A., *J. Am. Chem. Soc.* **2004,** *126*, 797.
106 Coleman, N. R. B.; O'Sullivan, N.; Ryan, K. M.; Crowley, T. A.; Morris, M. A.; Spalding, T. R.; Steytler, D. C.; Holmes, J. D., *J. Am. Chem. Soc.* **2001,** *123*, 7010.
107 Coleman, N. R. B.; Ryan, K. M.; Spalding, T. R.; Holmes, J. D.; Morris, M. A., *Chem. Phys. Lett.* **2001,** *343*, 1.
108 Ryoo, R.; Joo, S. H.; Kruk, M.; Jaroniec, M., *Adv. Mater.* **2001,** *13*, 677.
109 Flodstrom, K.; Wennerstrom, H.; Alfredsson, V., *Langmuir* **2004,** *20*, 680.
110 Kleitz, F.; Liu, D.; Anilkumar, G. M.; Park, I.-S.; Solovyov, L. A.; Shmakov, A. N.; Ryoo, R., *J. Phys. Chem. B.* **2003,** *107*, 14296.
111 Kleitz, F.; Hei Choi, S.; Ryoo, R., *Chem. Comm.* **2003**,
112 Zhao, D.; Huo, Q.; Feng, J.; Chmelka, B. F.; Stucky, G. D., *J. Am. Chem. Soc.* **1997,** *120*, 6024.
113 Finnefrock, A. C.; Ulrich, R.; Du Chesne, A.; Honeker, C. C.; Schumacher, K.; Unger, K. K.; Gruner, S. M.; Wiesner, U., *Angew. Chem. Int. Ed.* **2001,** *40*, 1207.
114 Huo, Q. S.; Margolese, D. L.; Ciesla, U.; Feng, P. Y.; Gier, T. E.; Sieger, P.; Leon, R.; TPetroff, P. M.; Schuth, F.; Stucky, G. D., *Nature* **1994,** *368*, 317.
115 Braun, P. V.; Osenar, P.; Stupp, S. I., *Nature* **1996,** *380*, 325.
116 Armatas, G. S.; Kanatzidis, M. G., *Nature* **2006,** *441*, 1122.
117 Landskron, K.; Ozin, G. A., *Science* **2004,** *306*, 1529.

118 Meng, Y.; Gu, D.; Zhang, F.; Shi, Y.; Yang, H.; Li, Z.; Yu, C.; Tu, B.; Zhao, D., *Angew. Chem. Int. Ed.* **2005,** *44*, 7053.
119 Melde, B. J.; Holland, B. T.; Blanford, C. F.; Stein, A., *Chem. Mater.* **1999,** *11*, 3302.
120 Inagaki, S.; Guan, S.; Fukushima, Y.; Ohsuna, T.; Terasaki, O., *J. Am. Chem. Soc.* **1999,** *121*, 9611.
121 Hatton, B.; Landskron, K.; Whitnall, W.; Perovic, D.; Ozin, G. A., *Accounts of Chemical Research* **2005,** *38*, 305.
122 Yang, Q. H.; Liu, J.; Zhang, L.; Li, C., *J. Mater. Chem.* **2009,** *19*, 1945.
123 Shylesh, S.; Samuel, P. P.; Sisodiya, S.; Singh, A. P., *Catal. Surv. Asia.* **2008,** *12*, 266.
124 Yang, Y.; Sayari, A., *Chem. Mater.* **2007,** *19*, 4117.
125 Inagaki, S.; Guan, S.; Fukushima, Y.; Ohsuna, T.; Terasaki, O., *J. Am. Chem. Soc.* **1999,** *121*, 9611.
126 Asefa, T.; Maclachlan, M. J.; Coombs, N.; Ozin, G. A., *Nature* **1999,** *402*, 867.
127 Liang, Y.; Anwander, R., *Micro. Meso. Mater.* **2004,** *72*, 153.
128 Shylesh, S.; Samuel, P. P.; Sisodiya, S.; Singh, A. P., *Catalysis Surveys from Asia* **2008,** *12*, 266-282.
129 Rebbin, V.; Jakubowski, M.; Potz, S.; Froba, M., *Microporous Mesoporous Mater.* **2004,** *72*, 99.
130 Landskron, K.; Hatton, B. D.; Perovic, D. D.; Ozin, G. A., *Science* **2003,** *302*, 266.
131 Wight, A. P.; Davis, M. E., *Chem. Rev.* **2002,** *102*, 3589.
132 Hoffmann, F.; Cornelius, M.; Morell, J.; Froba, M., *J. Nanosci. Nanotechnol.* **2006,** *6*, 265.
133 Rebbin, V.; Jakubowski, M.; Potz, S.; Froba, M., *Micro. Meso. Mater.* **2004,** *72*, 99.
134 Fukuoka, A.; Sakamoto, Y.; Guan, S.; Inagaki, S.; Sugimoto, Y.; Fukushima, K.; Hirahara, K.; Iijima, S.; Ichikawa, M., *J. Am. Chem. Soc.* **2001,** *123*, 3373.
135 Zhang, W.-H.; Lu, X.-B.; Xiu, J.-H.; Hua, Z.-L.; Zhang, L.-X.; Robertson, M.; Shi, J.-L.; Yan, D.-S.; Holmes, J. D., *Adv. Funct. Mater.* **2004,** *14*, 544.
136 Iler, R. K., *The Chemistry of Silica*. John Wiley & Sons: **1979**
137 Wu, S. Y.; Hsueh, H. S.; Huang, M. H., *Chem. Mater.* **2007,** *19*, 5986.
138 Platschek, B.; Kohn, R.; Doblinger, M.; Bein, T., *Langmuir* **2008,** *24*, 5018.
139 Platschek, B.; Kohn, R.; Doblinger, M.; Bein, T., *Chemphyschem* **2008,** *9*, 2059.
140 Huo, Q. S.; Zhao, D. Y.; Feng, J. L.; Weston, K.; Buratto, S. K.; Stucky, G. D.; Schacht, S.; Schuth, F., *Adv. Mater.* **1997,** *9*, 974.
141 Platschek, B.; Kohn, R.; Doblinger, M.; Bein, T., *Langmuir* **2008,** *24*, 5018-5023.
142 Cott, D. J.; Petkov, N.; Morris, M. A.; Platschek, B.; Bein, T.; Holmes, J. D., *J. Am. Chem. Soc.* **2006,** *128*, 3920.
143 Cauda, V.; Muhlstein, L.; Onida, B.; Bein, T., *Microporous Mesoporous Mater.* **2009,** *118*, 435.
144 Cauda, V.; Onida, B.; Platschek, B.; Muhlstein, L.; Bein, T., *J. Mater. Chem.* **2008,** *18*, 5888.
145 Keilbach, A.; Doblinger, M.; Kohn, R.; Amenitsch, H.; Bein, T., *Chem. Eur. J.* **2009,** *15*, 6645.
146 Hill, J. J.; Cotton, S. P.; Ziegler, K. J., *Chem. Mater.* **2009,** *21*, 1841.
147 Lee, K. J.; Min, S. H.; Jang, J., *Chem. Eur. J.* **2009,** *15*, 2491.

148 Ku, A. Y.; Taylor, S. T.; Heward, W. J.; Denault, L.; Loureiro, S. M., *Microporous Mesoporous Mater.* **2006,** *88*, 214.
149 Lai, P.; Hu, M. Z.; Shi, D.; Blom, D., *Chem. Comm.* **2008**, 1338.
150 Petkov, N.; Platschek, B.; Morris, M. A.; Holmes, J. D.; Bein, T., *Chem. Mater.* **2007,** *19*, 1376.
151 Marlow, F.; Leike, I.; Weidenthaler, C.; Lehmann, C. W.; Wilczok, U., *Adv. Mater.* **2001,** *13*, 307.
152 Viswanatha, R.; Sapra, S.; Amenitsch, H.; Sartori, B.; Sarma, D. D., *J. Nanosci. and Nanotech.* **2007,** *7*, 1726.
153 Malfatti, L.; Kidchob, T.; Falcaro, P.; Costacurta, S.; Piccinini, M.; Guidi, M. C.; Marcelli, A.; Corrias, A.; Casula, M. F.; Amenitsch, H.; Innocenzi, P., *Micro. Meso. Mater.* **2007,** *103*, 113.
154 Castro, Y.; Julian, B.; Boissiere, C.; BViana, B.; Amenitsch, H.; Grosso, D.; Sanchez, C., *Nanotechnology* **2007,** *18*, 05705/1.
155 Bilderback, D. H. E., Pascal; Weckert, Edgar, *Journal of Physics B, Molecular and Optical Physics* **2005,** *35*, 773-797.
156 King, S., *Modern Techniques for Polymer Characterisation*. John Wiley: **1999**
157 Lettow, J. S.; Lancaster, T. M.; Glinka, C. J.; Ying, J. Y., *Langmuir* **2004,** *21*, 5738.
158 Eastoe, J.; Gold, S.; Rogers, S.; Wyatt, P.; Steytler, D. C.; Gurgel, A.; Heenan, R. K.; Fan, X.; Beckman, E. J.; Enick, R. M., *Angew. Chem. Int. Ed.* **2006,** *45*, 3675.
159 Eastoe, J.; Paul, A.; Nave, S.; Steytler, D. C.; Robinson, B. H.; Rumsey, E.; Thorpe, M.; Heenan, R. K., *J. Am. Chem. Soc.* **2001,** *123*, 988.
160 Eastoe, J.; Gold, S.; Steytler, D. C., *Langmuir* **2006,** *22*, 9832.
161 Eastoe, J.; Gold, S., *Phys. Chem. Chem. Phys.* **2005,** *7*, 1352.
162 Fratzl, P., *J. Appl. Crystallogr.* **2003,** *36*, 397.
163 Lenaerts, V.; Triqueneaux, C.; Quarton, M.; Riegfalson, F.; Couvreur, P., *Int. J. Pharm.* **1987,** *39*, 121.
164 O'Driscoll, B. M. D.; Hawley, A. M.; Edler, K. J., *J. Coll. Inter. Sci.* **2008,** *317*, 585.
165 Bauer, G. S., *Nuclear Instruments and Methods in Physics Research A* **2001,** *463*, 505.

Chapter 2

Experimental

2.1 Experimental Methods

2.1.1 Materials and Reagents

Hexadecyltrimethylammonium bromide (CTAB) was supplied by Fluka, UK. The polyethylene oxide-polypropylene oxide-polyethylene oxide ($PEO_{100}PPO_{65}PEO_{100}$) tri-block co-polymer F127 and the polyethylene oxide-polypropylene oxide-polyethylene oxide ($PEO_{30}PPO_{65}PEO_{30}$) tri-block co-polymer P123 were supplied by BASF, New Jersey, USA. Deuterium (D_2O) and Brij 56 ($CH_3(CH_2)_{11}EO$) were used as supplied by Sigma-Aldrich. Tetraethyl orthosilicate (TEOS), 2-bis-(triethoxysilyl) ethane (BTESE), the thiol precursor 3-mercaptopropyl-trimethoxy silane (MPTMS), chloroauric acid ($HAuCl_4$) and anhydrous hexane were all supplied by Sigma Aldrich. Di-phenyl germane was supplied by Gelest. All chemicals were used as received.

Table 2.1 A list of surfactants used in this work

Name	Chemical Formula
P123	$PEO_{30}PPO_{65}PEO_{30}$
F127	$PEO_{100}PPO_{65}PEO_{100}$
CTAB	$(C_{16}H_{33})N(CH_3)_3^-Br^+$
Brij 56	$C_{12}H_{33}(OCH_2CH_2)_{10}OH$

2.1.2 Preparation of Liquid Crystals

A stock solution of liquid crystal, which consisted of 50 wt% of surfactant (either F127, Brij 56 or CTAB) in D_2O, was prepared 2 h before SANS measurements were conducted. The surfactant was dissolved in the D_2O while stirring at room temperature. The resultant viscous liquid crystal paste was applied evenly to the entrance window of the pressure cell. In order to prevent the dehydration of the liquid crystal film a wad of cotton wool soaked in D_2O was inserted into the cell to saturate the CO_2 with water. The cell was allowed to equilibrate for up to 30 minutes before SANS data was collected.

2.1.3 Preparation of Micellar Solutions

A stock micellar solution, which consisted of 2.5 wt% of surfactant (either F127 or CTAB) in D_2O, was prepared 2 h before SANS measurements were conducted. The surfactant was dissolved in the D_2O while stirring at room temperature. The resultant solution was placed in high pressure cell and was allowed to equilibrate for up to 30 minutes before SANS data was collected.

2.1.4 Preparation of Ethylene-Bridged PMO Thin Film Gel

Ethylene bridged PMO thin films were prepared from a gel preparation similar to that reported previously by Platschek *et al*. [1]. In a typical synthesis 2.08 g of silica and organo-silica precursor, 3 mL of 0.2 M aq HCl, 1.8 mL of H_2O and 5 mL of ethanol were mixed at 60°C for 1 hour. To this solution, 15 mL of a 5 wt % P123 in ethanol solution was then added and left to stir at room temperature for 1 hour, after which the gel was filtered. This gel was then dropped

onto a Whatman AAM with 200 nm pores until the membrane was completely covered and left to dry under atmospheric conditions or in a controlled humidity atmosphere (various humidities include 20% RH, 40% RH and 80% RH). *In-situ* SAXS experiments were conducted on drying PMO-AAM composites.

2.1.5 Synthesis of Ethane Bridged PMO

Ethane bridged PMO was synthesised following the method proposed by Guo *et al.* [2]. Typically, 1.2 g of P123 and 3.5 g of NaCl were dissolved in 40 mL of 0.5M HCl at 40°C. Then 2.1 mL of BTESE was added quickly under vigorous stirring and left stirring for 20 hours. The gels were then aged at 80℃ for 60 h statically. The resultant white powder material was collected, washed with copious amounts of ethanol and dried at room temperature and under vacuum. The P123 surfactant was removed by subsequent washing in a dilute HCl/ethanol solution and recovered. The washing procedure was repeated a number of times.

2.1.6 Functionalisation of PMO

The PMO powder was suspended in 100 mL dry toluene and heated to 100℃ under nitrogen reflux for 30 min before the thiol-silane precursor (MPTMS) was added to the refluxing mixture. The modification was carried out over 20 h, after which the PMO-Et-Thiol material was quickly recovered and washed with copious amounts of ethanol and dried under vacuum.

2.1.7 Gold Nanoparticle Inclusion in Functionalised PMO

The thiol functionalised PMO material was suspended in an aqueous 0.02M chloroauric acid solution and left for 2 hours under stirring. The basic thiol groups which were incorporated into the PMO material during the functionalisation step now act as reduction centres, which react in a neutralisation reaction with the chloroauric acid resulting in the deposition of metallic gold clusters on the surface and in the pores of the PMO material to produce the pink PMO-Au material.

2.1.8 Germanium Inclusion in PMO-Au Material

The deposition of germanium metal within the pore structure of the Au-PMO-Et was carried out as follows. 10 mg of the pink Au-PMO-Et material was placed in a 1 mL high pressure cell (316 SS from HIP, Indiana), along with di-phenyl germane (10 μL) in 0.6 mL of hexane, see Figure 2.1. The cell was heated to 380°C, reaching that temperature within 10 min and held at temperature for approximately 1 h to degrade germanium precursor before the cell was allowed to cool to ambient conditions and the black material, Ge-Au-PMO-Et-Thiol was collected.

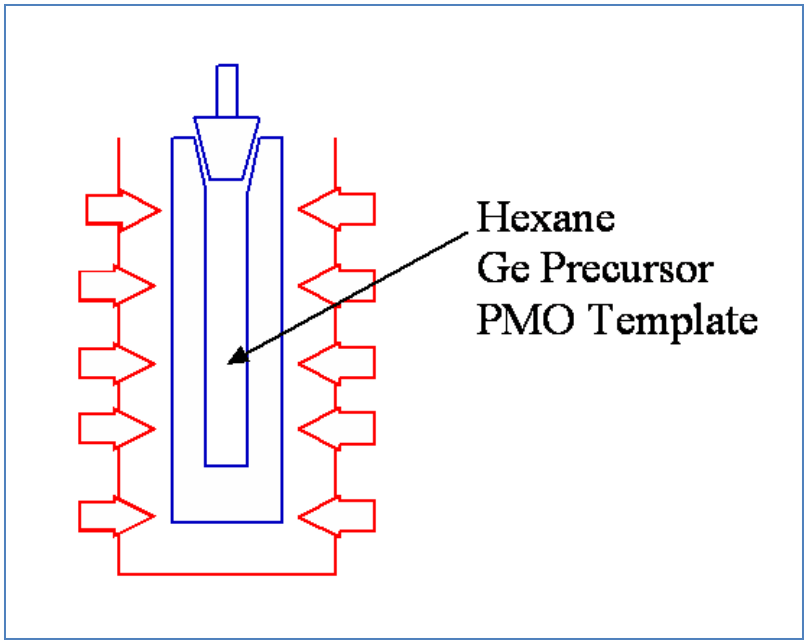


Figure 2.1 A schematic of the "bomb" cells used in the inclusion of germanium metal into the Au-PMO-Et-Thiol material

2.1.9 Polystyrene-*block*-Polymethylmethacrylate Thin Films

The polystyrene-*block*-polymethylmethacrylate (PS-*b*-PMMA) polymer thin films, which consisted of vertical pores in a PS matrix, were kindly donated from Prof. Michael Morris' research group in UCC. The production of the etched PS-PMMA thin films have been reported in Xiao *et al.* [3] but is briefly reviewed here. Vertically orientated pores in a PS matrix are produced on a hydroxyl-terminated silicon wafer with pre-deposited 6 nm PS-b-PMMA random copolymer wetting layer. A 1% (w/w) PS-*b*-PMMA in toluene solution was then spin coated onto the substrate and annealed under vacuum at 180° C for more than 24 h which induces phase separation between the PS and PMMA. To produce the ordered vertical pores in a PS matrix the PMMA phase must be removed. This is accomplished by decomposition of the cylindrical

PMMA cylinders with deep UV exposure, followed by washing with acetic acid and deionised water to remove the degraded PMMA polymer. This etching step is also thought to etch the PS-*b*-PMMA random copolymer wetting layer that exists below the PS-*b*-PMMA layer. This process leaves pores of approximately 50 nm in diameter, 25 nm deep (approx) with a spacing of 25 nm (approx) between pores. Figure 2.2 shows an AFM and hi-res SEM images of the as received PMMA etched PS template.

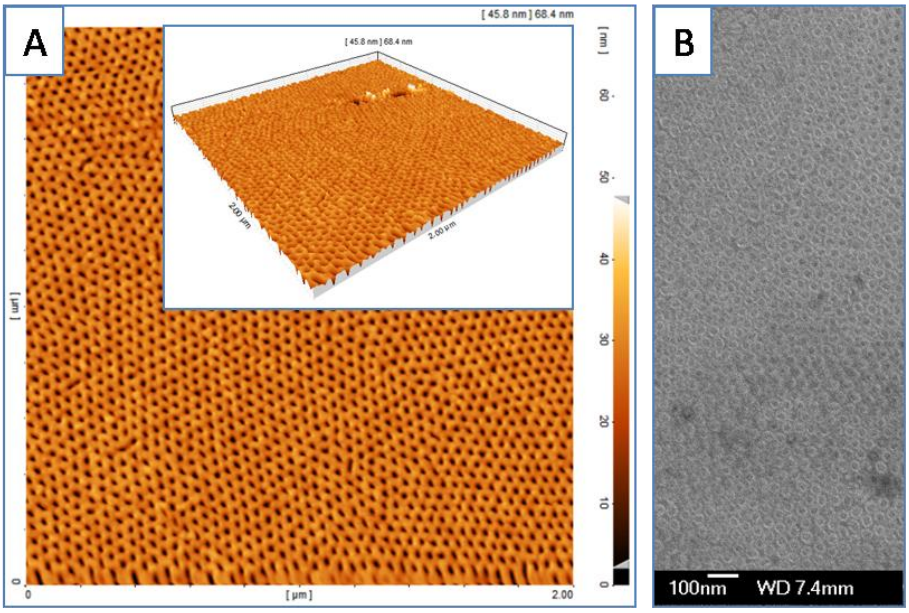


Figure 2.2 (a) AFM image of the hexagonally ordered porous PS matrix after removal of the PMMA block on silicon wafer and (b) an SEM image of the same material showing the hexagonally ordered pore structure of the PS matrix.

2.1.10 Functionalisation of Exposed Silicon on the PS Template

The PS templates were suspended back to back by a Teflon clip in 100 mL dry toluene and heated under reflux and nitrogen for 1 hour before the thiol-silane precursor (MPTMS) was

added to the refluxing solution. The modification was carried out over 5 hours, after which the films were washed with copious amounts of ethanol and left to dry under nitrogen.

2.1.11 Preparation of Thiol-Stabilised Gold Nanoparticles

Thiol stabilised gold nano-particles were synthesised following the procedure outlined in Hostetler *et al.* [4]. The synthesis method is reviewed here. A typical synthesis was carried out as follows; to a 0.31 g of hydrogen tetrachloroaurate trihydrate ($HAuCl_4.3H_2O$) in 25 mL deionised water solution at room temperature was added, under vigorous stirring, a solution of 1.5 g tetraoctyammonium bromide in 80 mL toluene. The aqueous layer quickly cleared while the organic phase became brown with the transfer of the reduced $[AuCl_4]^-$. The organic phase was then separated and to it 0.04 mL (0.053 g) of dodecanethiol was added. The solution was stirred at room temperature while 0.38 g of $NaBH_4$ in 25 mL of deionised water was added over the course of 10 seconds resulting in the organic phase becoming darker in colour. This solution was then transferred to a 30°C water bath where it was continuously stirred for approximately 3 h. Finally the organic phase was collected and solvent removed on a rotary evaporator, the dark waxy product was re-suspended in ethanol and sonicated briefly, filtered and washed with more ethanol. The final product was filtered, recovered and re-suspended in toluene after which it was ready for use. The synthesis resulted in nanoparticles of size range of 5 to 15 nm determined from TEM analysis, see Figure 2.3.

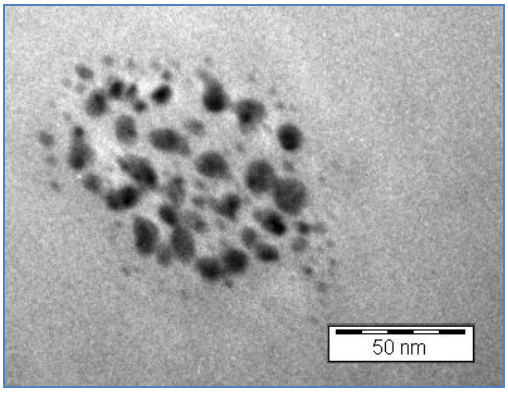


Figure 2.3 TEM micrograph of the thiol stabilised gold nanoparticles

2.1.12 Deposition of Gold Nanoparticles into PS Templates

The thiol functionalised PS template films were suspended in a toluene suspension of gold thiol stabilised nanoparticles and left for approximately 2 h under stirring after which the films were washed with ethanol. The thiol groups on the exposed silicon of the polymer film templates are thought to exchange with the thiol groups stabilising the Au nanoparticles and results in the deposition of clusters of Au nanoparticles within the vertical pores of the polymer template. A schematic of the whole process from unetched PS-PMMA phase separated polymer film to etched PS template to exposed silica functionalisation to gold nanoparticle inclusion is shown in Figure 2.4.

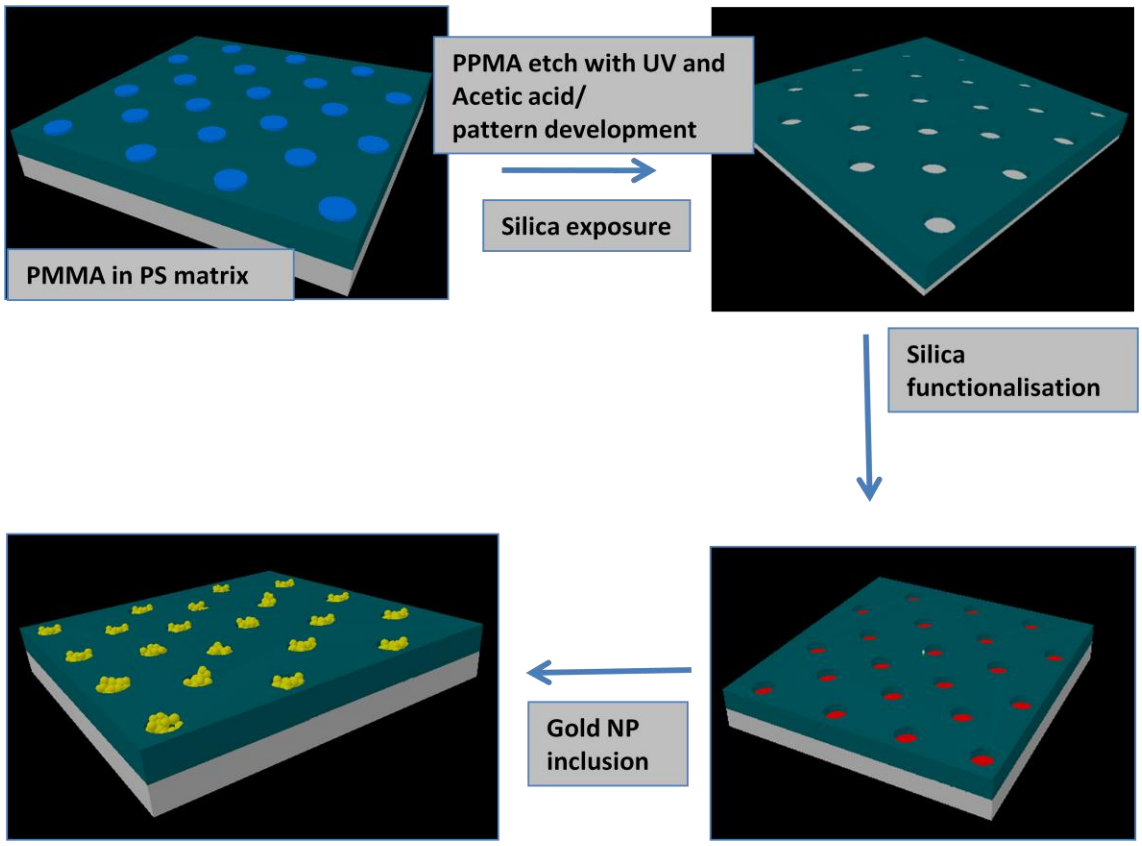


Figure 2.4 Schematic showing the deposition of gold nanoparticles in the PS polymer template.

2.1.13 Growth of Germanium Nanowires from Gold Nanoparticles in Polymer Templates

The deposition of germanium metal within the pore structure of the PS template was carried out in a similar fashion to that described above for the PMO material, but a larger cell was used to accommodate the polymer substrates. The PS template (approx 1 cm by 2 cm) substrate with the deposited thiol stabilised gold nanoparticles was placed in a 25 mL high pressure cell, along with 0.1 mL of di-phenyl germane in 10 mL of hexane, see the representation in Figure 2.5. The cell

was placed in a tube furnace and pressurised with CO_2 to 4000 psi using an Teledyne ISCO syringe pump (Lincoln, NE) heated to 380°C, at a ramp rate of 5°C/min and held at temperature for approximately 1 h to degrade the germanium precursor before the cell was allowed to cool to ambient conditions and substrates recovered, washed with ethanol and left to dry under a flow of N_2 gas.

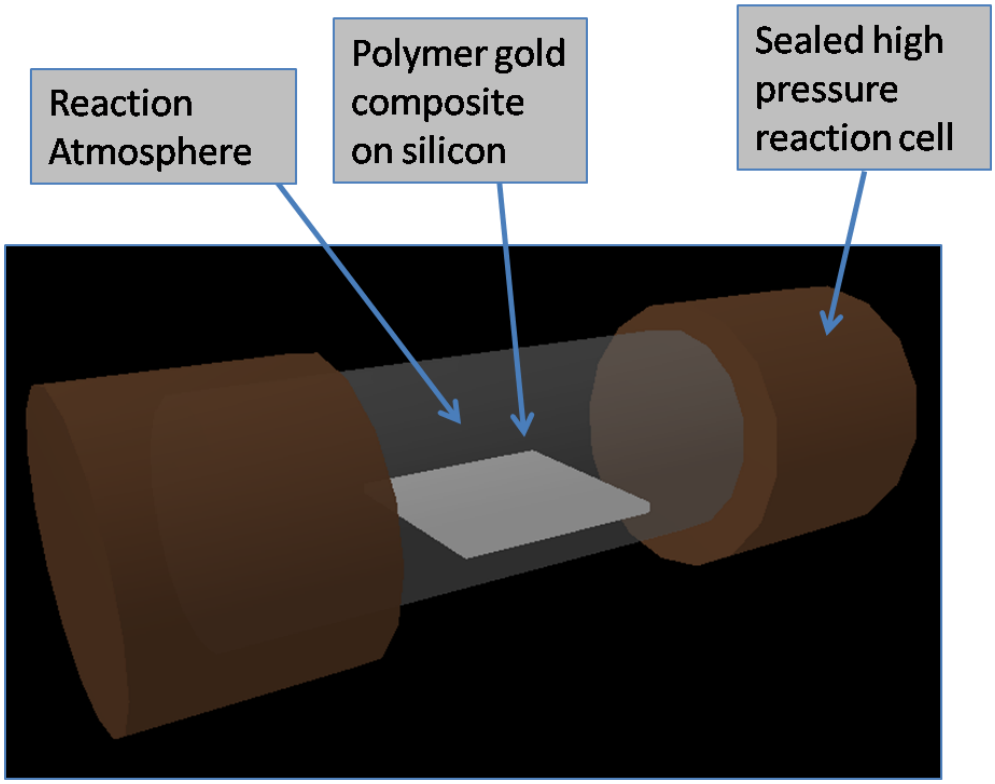


Figure 2.5 Schematic showing the high pressure reaction cell with the polymer gold composite on a silicon wafer.

2.1.14 Growth of Germanium Nanowires from a Silicon Wafer

Germanium nanowires were also grown from gold nanoparticles deposited on a clean silicon wafer using the same functionalisation and deposition technique and similar gold nanoparticles as those described above. Figure 2.6 shows an AFM image of the deposited gold nanoparticles.

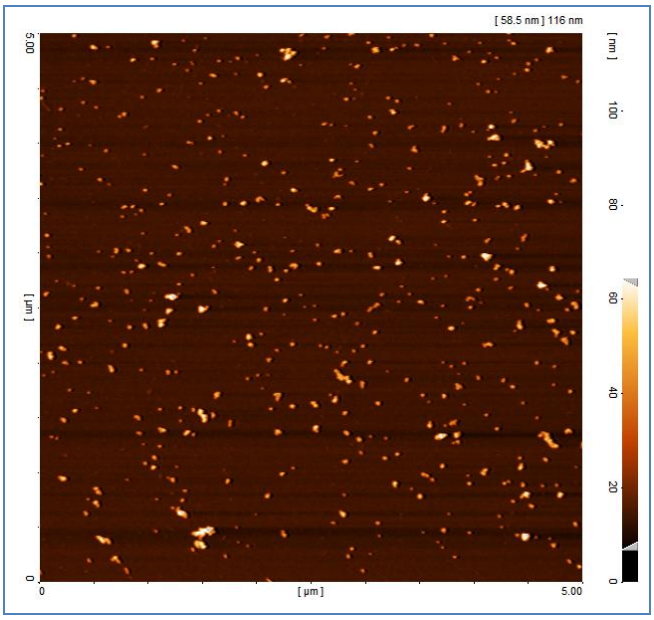


Figure 2.6 AFM image showing the deposited gold nanoparticles on a clean silicon substrate from which germanium nanowires were grown.

2.2 Characterisation Techniques

2.2.1 Powder X-Ray Diffraction

Powder X-Ray Diffraction (PXRD) is a technique used to investigate the crystalline atomic structure of a material. X-rays have wavelengths in the range of inter-atomic distances (0.1 Å to 10 Å) which make them suitable for the characterisation of crystalline materials. When x-rays interact with a crystalline material they are scattered or diffracted by the electrons in the atoms of the material. The scattered x-ray maxima are defined by Bragg's Law $n\lambda=2d\sin\theta$, where n is an integer, λ is the wavelength of radiation, d is known as the d-spacing between crystal lattice planes and θ is the angle at which the maxima occur, which correspond to a lattice plane with a specific d-spacing. Figure 2.7 shows a schematic of the interaction and diffraction of x-rays from a crystalline material.

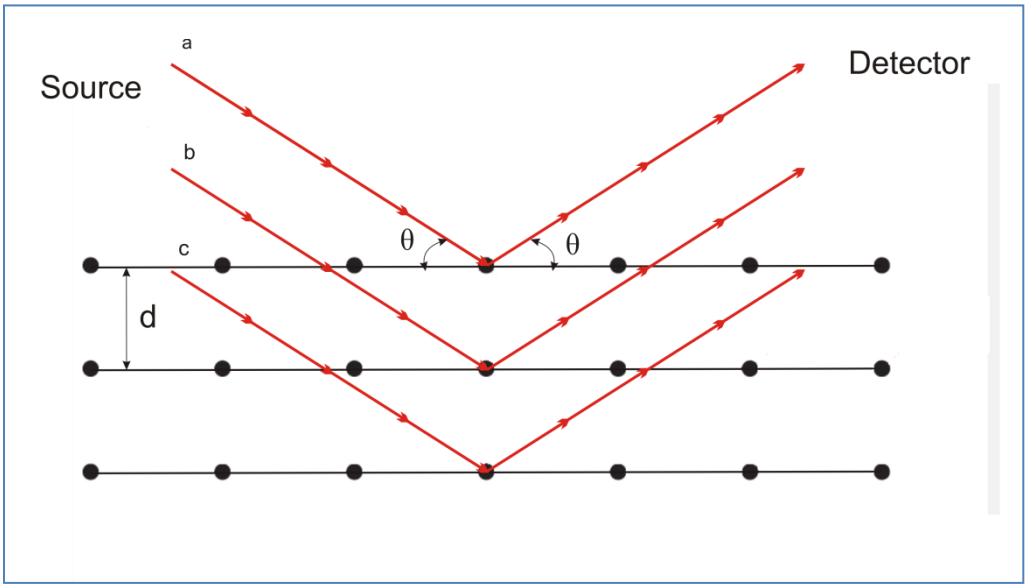


Figure 2.7 Schematic showing the interaction and diffraction of x-rays from a crystalline material. Incident x-rays are on the left with the diffracted x-rays on the right.

During a PXRD measurement the intensity of the diffracted radiation is measured as a function of the angle of diffracted radiation. This gives a diffraction pattern which is characteristic for the material under investigation.

Different materials have characteristic XRD patterns, therefore using a database of known x-ray structures it is possible to determine the composition of a polycrystalline material which consists of a number of different crystalline materials. The PXRD data reported in this thesis were collected on a Phillips X'pert MPD machine operating at 40 kV and 35 mA, using programmable divergent slits to maintain a constant beam footprint on the sample. Scans were conducted using Gonio geometry. Copper radiation (1.54 Å) was used as an x-ray source. A schematic of the x-ray instrument used is shown in Figure 2.8.

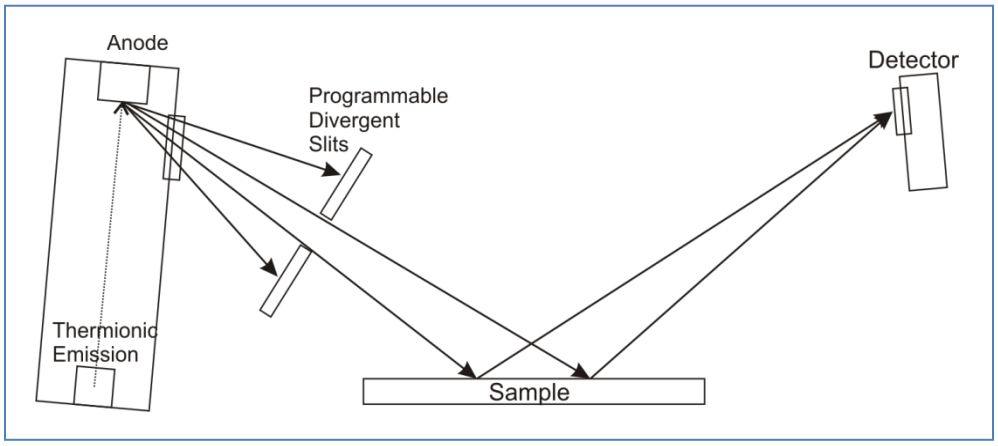


Figure 2.8 A schematic of the PXRD instrument and geometry used to collect data for this thesis.

2.2.2 Nitrogen Adsorption

Isothermal adsorption of nitrogen gas onto the surface of a material is the basis of determining the surface area of a material. The adsorption of nitrogen molecules onto a surface free of contaminants (surface moisture or other adsorbants) at extremely low pressures results firstly in the build up of a monolayer, followed by multi-layers of nitrogen molecules. Knowledge of the diameter of the nitrogen molecule, the amount of adsorbed nitrogen and application of a suitable mathematical model, the surface area of the material can be calculated. If the material possesses an ordered porous network then a pore diameter distribution and total pore volume can also be calculated.

A number of different mathematical models exist to determine the surface area of a sample from the information obtained from a N_2 adsorption experiment. The Brunauer, Emmett and Teller (BET) model which was developed by Stephen Brunauer, Paul Emmett and Edward Teller in 1938 is the standard method to determine the surface area of a material from N_2 adsorption/desorption isotherms [5].

Pore size determination is accomplished by application of the Barrett, Joyner and Halenda (BJH) mathematical model for the capillary condensation or evaporation of the adsorbing gas in the pores of a material under investigation [6]. N_2 adsorption can be used in the pore size analysis of mesopores (between 20 and 500 Å) materials. Pore size determination of microprores (below 20 Å) in materials requires a smaller molecule like krypton or argon and lower vacuum pressures. Macroporous (above 500 Å) measurements require a larger adsorbant molecule, for example Hg (Mercury porosimetry).

Nitrogen adsorption/desorption data were carried out at liquid nitrogen temperatures (77.4 K) on a Micrometrics Gemini 2375 volumetric analyser. The volume of adsorbed nitrogen was measured as a function of the partial pressure of nitrogen P/P_0, where P is the actual pressure of N_2 and P_0 is the pressure at which nitrogen gas condenses to a liquid at 77.4 K. The resulting isotherm is representative of the interaction experienced between the adsorbing gas and the material. There are six different adsorption isotherms as defined by IUPAC [7]. The hysteresis type IV and V is a result of the capillary condensation and capillary evaporation not occurring at the same pressures and is characteristic of mesoporous materials.

2.2.3 Atomic Force Microscopy

Atomic force microscopy (AFM) is based on a very simple principle. An atomically sharp (or as close atomically sharp as possible) tip is scanned over a sample surface at either a constant tip to sample surface distance, or at a constant force experienced between the tip and the sample surface. A Piezo-electric motor allows the distance between the tip and the sample surface to be maintained or changed depending on the scanning mode. A laser reflected from the back of the tip cantilever to a photodiode is used to measures the distance between tip and sample surface. A feed-back loop is then employed to keep the distance or force constant. AFM tips are usually made from silicon nitride (Si_3N_4) or silicon to investigate sample topography but an AFM can be used to measure a number of different surface properties depending on the type of tip used, for example a magnetic tip can be used to investigate different areas of magnetic character or a tip can be contacted with the surface to measure conductivity. A DME 2452 Dualscope AFM using

NCHR-50 silicon tips supplied from Nanoworld was used to collect data on samples reported in this thesis.

2.2.4 Transmission Electron Microscopy

Transmission Electron Microscopy (TEM) is an imaging technique which is widely used to investigate structures on a scale of nanometres [8]. The principle of TEM is based on the imaging of transmitted electrons through a thin sample. The electrons are produced via thermionic emission from a filament and accelerated under high voltage in a vacuum, focused through a number of different lenses to a sample and then finally to an imaging device. A condenser lens focuses the beam of electrons from the electron source on the sample, after the electron beam has passed through the sample the objective and projector lenses image the beam onto the imaging plate or fluorescent screen to produce the magnified image. TEM images presented in this thesis were collected on a JEOL 200FX operating at a voltage of 200 keV. The samples to be imaged were suspended in ethanol and placed in an ultrasonic bath for approximately 10 minutes, a drop of the resultant suspension was placed on copper grid and left to dry under a clean upturned petri dish.

2.2.5 Scanning Electron Microscopy

Scanning Electron Microscopy (SEM) is a popular imaging technique used to image the topography of a sample. Unlike TEM, SEM irradiates a sample with a scanning electron beam and the resulting emission of electrons from the surface of the sample provides topographical information about the sample [8]. When the scanning beam of electrons hits the sample surface the

scanning electrons transfer energy to an electron in an atom at the sample surface, this excited electron (a secondary electron) is subsequently re-emitted. Differences in the topography of the sample will change the amount of secondary electrons emitted and hence provide information about the sample surface. The scanning electrons can also bounce off the sample surface when they collide with surface atoms; atoms with larger atomic numbers back scatter more electrons which provides contrast between different atomic phases. X-rays are also emitted from the irradiation of a sample with the scanning electron beam, these x-rays can be used to determine the chemical composition of the sample, this is known as energy dispersive x-ray spectroscopy and is discussed elsewhere. Low resolution SEM images were collected on a JEOL 5510 SEM with samples mounted on carbon tape on a brass stub. High resolution SEM images were collected on a JSM-6700 field-emission scanning electron microscope operating at a voltage of 10 keV.

2.2.6 Energy Dispersive X-Ray Spectroscopy

The irradiation of a sample with a beam of electron produces x-rays with specific energies or wavelengths depending on the chemical composition of the area irradiated. Analysis of the emitted x-rays gives local chemical composition data depending on the size of the area under investigation/irradiation. This technique is used in conjunction with SEM or TEM. Energy dispersive x-ray analysis (EDXA) of samples reported in this thesis was undertaken on an INCA X-Sight Energy Dispersive X-ray Spectroscopy (Oxford Instruments, Buckinghamshire, UK).

2.2.7 X-Ray Photoelectron Spectroscopy

X-ray photoelectron spectroscopy (XPS) is a technique which measures the binding energies of electrons removed form the core orbital of an atom. Irradiating an atom with specific x-ray photon energies, ionises the atom by ejecting a core electron, measurement of the kinetic energy of the ejected photoelectron allows the determination of the binding energy of that electron. Different elements have different binding energies associated with each core atomic orbital, this way different elements within a sample area can be identified by the different binding energies associated with the ejection of core electrons [9]. XPS is a surface analysis tool because the x-ray photons only penetrate a small distance into the sample. XPS data shown in this thesis was collected in collaboration with Intel Ireland using a Vacuum Generators 210F apparatus using Al Kα anode at 300 W power. Samples were mounted on double sided carbon tape and data was collected at an emission angle of 90° normal to the surface and at a a pass energy of 50 eV.

2.2.8 SANS Characterisation of Liquid Crystals

In-situ high pressure SANS experiments were conducted on the LOQ instrument at ISIS at the Rutherford Appleton Laboratory (RAL) in Oxfordshire, UK. The absolute scattering cross-section I(Q) (cm^{-1}) was measured as a function of the modulus of momentum transfer $Q(A^{-1}) = (4\pi/\lambda)\sin(\theta/2)$ where λ is the incident neutron wavelength (2.2 to 10 Å) and θ is the scattering angle (< 7°). All measurements were taken at 40 °C. Measurements performed on tertiary surfactant/D_2O/CO_2 mixtures were conducted at co-aqueous surfactant concentrations of 50 wt%.

SANS data from the surfactant liquid crystal phase was consistent with the formation of a single pore size suggesting uniform dispersion of the copolymers within the cylindrical micelles which make up the hexagonal liquid crystal phases. The d-spacing (pore-centre-pore centre distance, d) can be calculated using equation 2.1 below [10]:

$$d = \frac{4\pi}{Q_{MAX}\sqrt{3}} \qquad 2.1$$

where Q_{Max} is the position of the scattering peak maximum.

2.2.9 SANS Pressure Cell

The pressure set-up used in the high pressure SANS experiments consisted of the University of East Anglia (UEA) pressure cell in which the micellar solution was placed. During the liquid crystal experiments the liquid crystal solution was placed on the inside of the cell window, a D_2O soaked cotton bud was attached to the internal top of the cell to prevent the liquid crystal solution from drying out when the CO_2 was added to the cell. The cell was pressurised using a hydraulic pressurising mechanism. See Figure 2.9 for a schematic of the set-up.

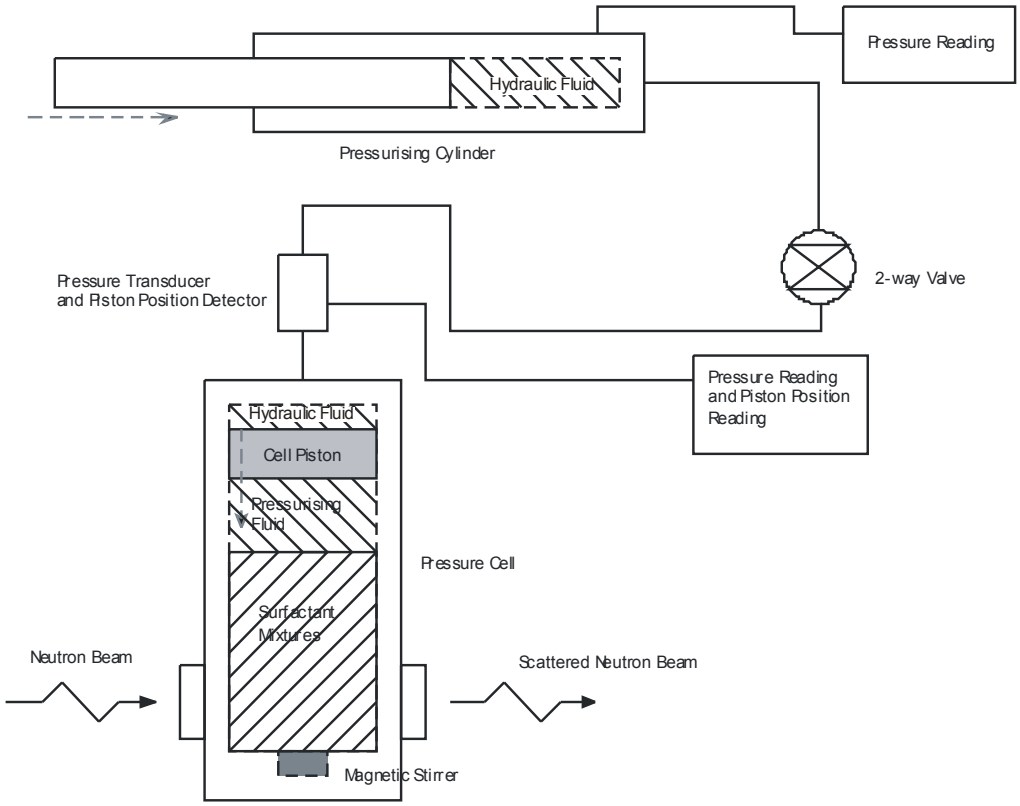


Figure 2.9 The pressure set-up used in the high pressure SANS measurements.

2.2.10 Characterisation of PMO-AAM Composites

Dry PMO-AAM composites were calcined to lift off any excess film material from the surfaces of the AAM. It should also be noted that this calcination step also reduces the size of the PMO filament within the AAM pores. *In-situ* SAXS data at grazing incidence angles were carried out at the ELETTRA Synchrotron facility, Trieste, Italy using a Gabriel CCD detector and monochromatized 8 keV X-rays. TEM images were collected on a JEOL 2000FX transmission electron microscope operating at a voltage of 200 kV. The membranes were prepared for plan-view TEM imaging by dimple grinding, followed by Ar-ion polishing. The dimple grinding was

accomplished using a Gatan model 656 dimple grinder using a 5 μm diamond paste. Further Precision Ion Polishing (PIPS) reduces the thickness of the AAM for TEM analysis which was done at grazing angles of 6° with a 5 kV acceleration voltage on a Gatan, Precision ion polishing system model 691.

2.2.11 Liquid Crystal Solubility Measurements

CO_2 adsorption measurements were performed on a magnetic suspension balance, Rubotherm (Bochum, Germany) in the Institute of Non-Classical Chemistry at the University of Leipzig, Permoserstr, Leipzig, Germany. This method measures the change of weight of a sorbent due to the adsorption of molecules from a surrounding compressed gas phase. The balance can be operated up to 500 bar using a magnetic coupling concept, which isolates the interior of the balance and the surrounding immediate environment. The weight gained by the substance is transmitted by magnetic suspension coupling from a closed and pressure-proof metal container to an external microbalance.

2.3 Central Facility Beamline Parameters

2.3.1 SAXS Beamline Parameters

At the SAXS Beamline at Elettra three different radiation energies were accessible through the use of different monochromotors. The different radiation energies accessible are 5.4, 8 and 16 keV. They correspond to radiation wavelengths of 0.077, 0.154 and 0.23 nm respectively. Samples can be held in the beam between two heating blocks. This is located on top of a sample table that can be moved along two axis of motion. A 2D CCD-detector is used as the detector with a total possible evacuated camera length of 2.3 m. A schematic of the SAXS Beamline at Elettra is shown in Figure 1.8.

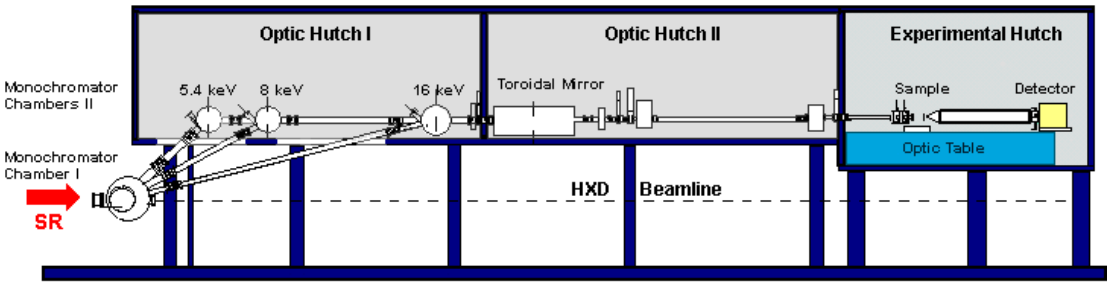


Figure 1.8 Schematic of the SAXS Beamline at Elletra.

2.3.2 LOQ Beamline Parameters

At the LOQ neutron Beamline at ISIS a range of wavelengths are used due to the nature of the spallation source. Due to this fact the detector is in a fixed position at 15.2 m from the moderator with a high angle detector positioned at 11.6 m from the moderator. The main

detector is a 64 cm2 3He gas detector. Due to the characteristics of the beam aperture and other factors that influence the beam before reaching the sample, neutrons of wavelengths between 2.2 to 10 Å are used. The neutron transmission of the sample is detected using a separate scintillator slab detector. A chopper is used to prevent the overlap of slow neutrons from one burst being overtaken by faster neutrons from the next burst.

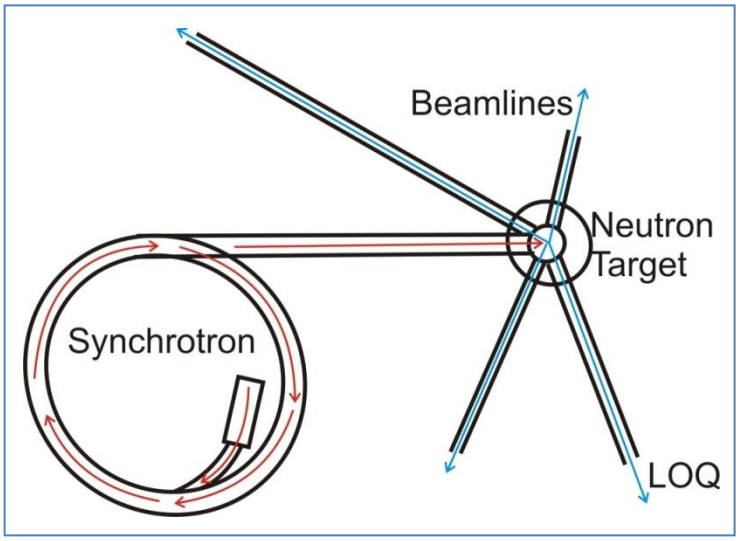


Figure 1.9 A plan of the ISIS facility showing the synchrotron and target used in the production of neutrons which are used in the various Beamlines including the SANS Beamline LOQ

2.4 Small-Angle Scattering Theory

2.4.1 Mathematical Modelling of Small-Angle Neutron Scattering Data from Micelles

Surfactant molecules under the correct solution conditions spontaneously self assemble to form stable aggregated micelles. Micelles are of the size range of tens to hundreds of Ångströms, therefore small-angle neutron scattering (SANS) is a very useful method when investigation of the size, shape and spatial ordering of micelles is required. Obtaining useful structural micelle information from SANS data requires the use of mathematical algorithms to model the neutron scatting patterns from a micellar solution. The SANS technique assumes that the system under investigation comprises of individual but identical particles of small size distribution interacting with each other. The difference between the incident and scattered radiation (the scattering vector) contains information about the scattering particles. The scattering from particles can be separated into two contributions, firstly the form factor P(q) (or F(q)) which represents the shape and size of the particles and the structure factor S(q), which represents the interactions between the individual particles.

2.4.2 Small-Angle Scattering Theory

Small-angle scattering (SAS) is technique employed to determine structural information from a material by the scattering of radiation of a low angle from that material and is an umbrella term for a number of different techniques using different forms of radiation. Small-Angle Neutron Scattering (SANS), Small-Angle X-ray Scattering (SAXS) and Light Scattering (LS) all employ the same fundamental principle. The elastic collisions of radiation with matter and the resulting

scattering pattern is the basis for all small-angle scattering techniques. The scattering pattern resulting from different systems can be modelled and information about the shape, size and orientation of the system under investigation can be extracted. Depending on the type of radiation wavelength used different length scales are investigated. For example neutrons with a typical wavelength of between 0.15 to 2.5 nm are suitable to investigate lengths of 0.5 to 1000 nm, where as hard x-rays having a wavelength of 0.15 nm and can be used to measure sizes of 0.1 to 2500 nm [11]. For example at LoQ, the small-angle neutron scattering instrument at ISIS, wavelengths of between 0.22 and 1 nm are used while at the small-angle x-ray scattering instrument at Elettra has a choice of three different wavelengths, 0.077, 0.154 and 0.23 nm depending on which of the three available x-ray energies are chosen.

Small-angle scattering examines the difference between incident radiation and the scattered radiation, the intensity of the scattered radiation is described by the scattering vector, also known as the wave vector transfer or the momentum transfer [12]. It is known by Q in SANS and by S in SAXS; both have the same units of 1/length and is shown in equation 2.2.

$$q = |q| = |k_s - k_i| = \frac{4\pi n}{\lambda} \sin\left(\frac{\theta}{2}\right) \approx \frac{4\pi}{\lambda} \frac{r_{\text{det}}}{L_{sd}} \qquad 2.2$$

Where r_{det} is height coordinate at the detector and L_{sd} is the length to the detector. K_s is the scattered radiation vector, K_i is the initial radiation vector. Scattered neutrons that arrive at small r_{det} have only been scattered by a small amount, or have only been scattered by a small Q value. Substituting this into Bragg's formula we get equation 2.3.

$$d = \frac{2\pi}{q} \qquad 2.3$$

Where *d* is the length scale under investigation.

The other value measured during a SAS experiment is the differential scattering cross section or the "intensity" of scattered radiation. It is in fact a flux, i.e. the number of neutrons of a particular wavelength, scattered through a particular angle, that arrive at a small area of the detector in unit time [11]. The cross section is dependent on a number of parameters, as can be seen below in equation 2.4.

$$I(q) = [I_0(\lambda)][\Delta\Omega][\eta(\lambda)][T(\lambda)][V_s]\frac{\partial\Sigma}{\partial\Omega}(q) \qquad 2.4$$

The different terms are explained as follows; $I_0(\lambda)$ is incident flux, $\Delta\Omega$ solid angle element defined by the size of the detector pixel, $\eta(\lambda)$ is the detector efficiency, $T(\lambda)$ is the radiation transmission of the sample, V_s is the volume of the sample illuminated with radiation and $\frac{\partial\Sigma}{\partial\Omega}(Q)$, which is that term in which all the structural information is retained.

The first three terms are instrument specific; the last three terms are specific to the sample. The last term is actually the Q term (i.e. the scattering vector) and retains all the structural data.

The differential scattering cross section $\frac{\partial\Sigma}{\partial\Omega}(Q)$ term can be described as a combination of the structural information [11], see equation 2.5;

$$\frac{\partial \Sigma}{\partial \Omega}(q) = NV^2(\Delta\rho)F(q)S(q) + B \qquad 2.5$$

Where N is the number of scattering particles, V is the volume of one scattering centre, $(\Delta\rho)^2$ is the contrast between different phases (for example the contrast between solvent and sample, the Z number in SAXS and the Scattering Length Density in SANS). B is the background signal that is always present due to cosmic radiation, but is removed once the data has been normalised. The $P(Q)$ term is called the form factor and describes the interference between different particles/waves scattered from the same scattering centre. $S(Q)$ is the structure factor and describes the interference between different particles/waves scattered from different scattering centres. The more dilute the number of scattering centres this term tends to unity.

The contrast term (Δρ) is an important term in any scattering experiment; if there is no contrast between the sample material and the matrix that contains it then the sample itself becomes indistinguishable from the matrix material. In SAXS the electron density difference between sample and matrix produces the contrast, in LS it is different refractive indexes which produce the contrast. However, in SANS the equivalent factor is called the scattering length density, ρ which produces contrast between different materials.

The form factor P(Q) and the scattering factor S(Q) are modelled to obtained data about the system under investigation. These terms will change as the geometry and interaction of the

different scatters change from system to system. In SANS it is in the scattering cross section that all the information about the size, shape and the interactions of different scatters (atoms or molecules) is contained.

2.4.3 The Pluronic Micelle Model

As stated above the differential scattering cross section is the term that is modelled to retrieve the structural data from a scattering pattern. Many models exist for the retrieval of structural data from the scattering data of a micelle solution. The model used here has been used in the past to model the structure of Pluronic micellar solutions under different environmental conditions. Mortensen [13] has used the model to investigate different Pluronic systems at different concentrations and at different temperatures. It has been used more recently by Yang *et al.* to investigate the Pluronic L64 at various temperatures [14] and Goldmints *et al.* [15] who investigated micelle formation of the Pluronic P85. A least squares fitting routine was used to model the experimental data with the modelled data.

As stated above the SANS scattering intensity *I(q)* (differential scattering cross section) can be described as a product of the form factor and scattering factor, see equation 2.6.

$$I(q) = (\Delta\rho)^2 NF(q)S(q) \qquad 2.6$$

Where $\Delta\rho$ is the difference in neurton scattering length densities (SLDs) between the scattering particles and the surrounding medium (i.e. solvent) and N is the number scattering particles. B is

a constant that describes incoherent background scattering. The form factor describes the structure of the scattering particle and the structure factor describes the interaction between scattering particles.

2.4.4 Form Factor

The form factor of a uniform spherical particle is shown in equation 2.7.

$$F(q) = \{\frac{3[\sin(qR) - qR\cos(qR)]}{(qR)^3}\}^2 \qquad 2.7$$

Where *R* is the radius of the sphere. However, to accurately describe the core shell structure of a Pluronic micelle this form factor needs to be expanded. For the F127 micellar system the dry PPO core which has a low SLD is surrounded by the D_2O saturated PEO corona with a relatively high SLD. This difference gives good contrast and a sharp interface between the core, corona and solvent where three distinct regions and interfaces can be distinguished 1) the micelle PPO core, 2) the D_2O hydrated PEO micelle corona and 3) the D_2O solvent itself. However this assumes a large amount of water is present in the PEO corona and a low amount of water is present in the PPO core and PPO and PEO do not mix once above the critical micelle temperature. Taking this into account, equation 2.8 describes the scattering for a core/shell particle.

$$I(q) = N\{\frac{4\pi R_1^3}{3})(\rho_{core} - \rho_{shell})[\frac{3J_1(X_1)}{X_1}] + \left(\frac{4\pi R_2^3}{3}\right)(\rho_{shell} - \rho_w)[\frac{3J_1(X_2)}{X_2}]\}^2 S(q) + B \qquad 2.8$$

In equation 2.8, R_1 and R_2 are the core radii and the core + corona radii respectively, ρ_{core}, ρ_{shell} and ρ_w are the scattering length densities (SLDs) of the core, corona and solvent respectively. J_1 is the first order Bessel function and is used in representing spherical coordinates, J_1 is shown in equation 2.9.

$$J_1 = \frac{[\sin(x) - x\cos(x)]}{x^2} \qquad 2.9$$

One assumption used in this model is that the core consists of PPO, a small known amount of water and whichever solvent is swelling the micelle core. The corona only consists of PEO and a larger known amount of water. The corona is not thought to responsible for any changes in the micelle size during swelling. The composition of the core and corona reflect the SLDs of the core, ρ_{core} and corona, ρ_{shell}. The SLD of the core (ρ_{core}) is a function of the volume fraction of PPO, water and swelling agent in the core α_{ppo}, $fracW_{core}$ and fracS respectively. The SLD of the shell (ρ_{shell}) is a function of the volume fraction of PEO and water, α_{ppo}, $fracW_{shell}$ respectively. Both ρ_{core} and ρ_{shell} are shown in equations 2.10 and 2.11.

$$\rho_{core} = \alpha_{ppo}(\rho_{PPO}) + fracW_{core}(\rho_W) + fracS(\rho S) \qquad 2.10$$

$$\rho_{shell} = \alpha_{peo}(\rho_{PEO}) + fracW_{shell}(\rho_W) \qquad 2.11$$

The SLDs of dry PPO and PEO are $\rho_{PPO} = 0.325 \times 10^{10}$ cm^{-2}, $\rho_{PEO} = 0.549 \times 10^{10}$ cm^{-2} respectively. The SLD of D_2O is $\rho_W = 6.44 \times 10^{10}$ cm^{-2}. The volume fractions of PPO (α_{PPO}) and PEO (α_{PEO}) are shown in equations 2.12 and 2.13. The amount of water in the core and the corona were determined from separate experiments and were not thought to change unless the temperature of the system was changed.

$$\alpha_{ppo} = 1 - fracW_{core} - fracS \qquad 2.12$$

$$\alpha_{peo} = 1 - fracW_{shell} \qquad 2.13$$

The volume of 70 PPO units is $V_{PPO} = 6678$ Å^3 and the volume of 200 PEO units is $V_{PEO} = 14{,}480$ Å^3 as determined by the volumes given in Morttensen *et al.* [16] for individual PPO and PEO units. The volume fraction of the swelling solvent was determined from the change in micelle core volume and is shown in the equation 2.14.

$$fracS = \frac{(V_1 - V_0)}{(V_1 - V_0) + N_{agg}V_{ppo}} \qquad 2.14$$

The initial aggregation number ($N_{agg,0}$) was calculated from equation 2.15. Subsequent aggregation numbers for the swollen micelles were calculated from a constant interfacial surface area per surfactant monomer using equation 2.16.

$$N_{agg,0} = \frac{(4/3)\pi R_{1,0}^3(\alpha_{ppo})}{V_{ppo}} \qquad 2.15$$

$$N_{agg} = N_{agg,0}\left(\frac{R_{1,0}}{R_1}\right)^2 \qquad 2.16$$

The fitting parameters which are modelled with this form factor are the core radius, R_1, the core plus corona radii, R_2, the micelle aggregation number N_{agg} and the volume fraction of swelling solvent in the core, *fracS*.

2.4.5 Inter-particle Structure Factor

The pronounced correlation peak (especially evident at high pressures and elevated temperatures) seen in the scattering data in chapter 3 is indicative of strong interactions between neighbouring micelles. The hard sphere structure factor is based on the Ornstein-Zernike and the Percus-Yevick approximations [17]. The structure factor described in equation 2.17 represents the intermicellar interaction which is determined from hard sphere interactions radius R_{hs} and the micelle volume fraction ϕ [16, 18].

$$S(q) = \frac{1}{[1 + 24\Phi G(2qR_{hs})/(2qR_{hs})} \qquad 2.17$$

Where ϕ is the micellar volume fraction, R_{hs} is the micelle hard sphere radius and G is a trigonometric function of A, where A = QR_{hs} and ϕ is shown in equation 2.18.

$$G(A)=\frac{\alpha(\sin A-A\cos A)}{A^2}+\frac{\beta(2A\sin A-(2-A^2)\cos A-2)}{A^3}+\frac{\gamma(-A^4\cos A+4((3A^2-6)\cos A+(A^3-6A)\sin A+6)}{A^5} \quad 2.18$$

Where α, β and γ are expressed by equations 2.19, 2.20 and 2.21 respectively.

$$\alpha=(1+24\Phi)^2/(1-\Phi)^4 \quad 2.19$$

$$\beta=-6\Phi(1+\Phi/2)^2/(1-\Phi)^4 \quad 2.20$$

$$\gamma=(\Phi/2)(1+2\Phi)^2/(1-\Phi)^4 \quad 2.21$$

As stated above the micelle volume fraction, ϕ is dependent on the concentration of surfactant and is of course dependant on the volume of PEO and PPO and the radii of the micelle, i.e. R_1 and R_2. In this model the micelle volume fraction was calculated using the expression shown in equation 2.22.

$$\Phi=C(\frac{V_{PPO}}{\alpha_1}+\frac{V_{PEO}}{\alpha_2})(V_{PPO}+V_{PEO}) \quad 2.22$$

The above equations describe the model used here to determine the core radius, R_1, the core plus corona radius, R_2, the micelle interaction radius, R_{hs} and C is the copolymer concentration

2.4.6 The CTAB Model

The fitting program FISH [19] was used to model the scattering data from CTAB micelles placed under liquid CO_2, sc-CO_2 and liquid propane atmospheres. The model that was chosen to fit the CTAB data was a Hayter-Penfold charged particle with an elliptical morphology, which is the model of choice when fitting scattering data from CTAB micelles [20, 21] or other charged particles with elliptical shapes [22] such as SDS micelles. The elliptical nature of the CTAB micelles makes for more complicated mathematical modelling of the scattering data when compared with the scattering from spherical micelles like those of the F127 micelles above.

The scattering intensity (differential scattering cross section) of monodispersed interacting anisotropic particles with no preferred interactions can be described as in equation 2.23;

$$I(q) = N[\langle F^2(q)\rangle + \langle F(q)\rangle^2 (S(q) - 1)] \qquad 2.23$$

Where *n* denotes the number density of micelles and *F(q)* is the form factor which represents the micelle shape and *S(q)* is the scattering factor which describes the interaction of neighbouring micelles. The elliptical nature of the CTAB micelles requires numerical integration of *F(q)* and $F(q)^2$ factors to account for all possible orientations of the elliptical particles with respect to the direction of the incident radiation, as seen in equations 2.24 and 2.25.

$$\langle F^2(q)\rangle = \int_0^1 [F(q,\mu)]^2 \, d\mu \qquad 2.24$$

$$\langle F(q)\rangle^2 = \left[\int_0^1 F(q,\mu)d\mu\right]^2 \qquad 2.25$$

Where F(q,μ) is stated in equation 2.26.

$$F(q,\mu) = \frac{3(\sin x - x\cos x)}{x^3} \qquad 2.26$$

And *x* is stated in equation 2.27.

$$x = q[a^2\mu^2 + b^2(1-\mu^2)]^{1/2} \qquad 2.27$$

Here *a* and *b* are the semi-minor and semi-major axis of the ellipsoid micelle, where for a prolate ellipse a=b<c, μ is the cosine of the angle between the axis of revolution of the micelle and the direction of radiation.

CTAB micelles are charged elliptical particles which experience a screened Coulombic repulsion force between each aggregate. Van der Waals forces between each aggregate are neglected due to the fact that they are much weaker than the Colombic interactions experienced between charged particles. The structure factor S(q) used in the fitting of the CTAB data describes the interaction between charged spheres which adequately describes the processes occurring within a dilute elliptical CTAB micelle solution. This assumption is known as the mean spherical approximation [20] which gives the effective spherical radius of the elliptical micelle σ, as

$\sigma=2(a^2b)^{1/3}$. The repulsion force depends on the ionic strength, the size and volume fraction and the net charge of the micelles. The expressions which describes this interaction of charged spheres was determined by Hayter and Penfold [23] and Hansen and Hayter [24] and it is the Fourier transform of the radial distribution function (g(r)) for the mass centres of the micelles [25]. The Hayter-Penfold model is also described in Penfold *et al.*[26]. The Fourier transform of the radial distribution function is shown in equation 2.28.

$$S(q) = 1 + C(q)n_m \int \exp(iQ.r)[g(r) - 1]dr \qquad 2.28$$

Where C(q) is shown in equation 2.29.

$$C(q) = F(q)^{-1}(\int_0^1 F(q,u)d\mu)^2 \qquad 2.29$$

In calculating the Fourier transform of the radial distribution function the screened Coulomb potential is needed as the charged micelles are interacting through a screened Coulomb potential, see equation 2.30.

$$u(r) = u_0 \frac{\sigma}{r} \exp[-\kappa(r - \sigma)] \qquad 2.30$$

Where κ is the inverse Debye screen length and u_0 is the contact potential between two charged micelles in solution and ζ is the effective spherical radius.

The inverse Debye screening length, κ is the length at which charged species screen electric potential, which in this case is the dissociated Br^- ions screening the cationic charge of CTA^+ micelle. The initial Debye screening length (κ=1/rd) was calculated using the following expressions in equation 2.32;

$$rd = \sqrt{\frac{\varepsilon K_r RT}{2\rho N_a{}^2 e^2 I_c}} \qquad 2.32$$

Where ε is the permittivity of free space, K_r is the permittivity of D_2O at 40° C, R is the Boltzmann constant, T is the temperature in degrees Kelvin. Below the line ρ is the bulk density of the medium (in this case D_2O at 40° C), N_a is Avogadro's number, e is the charge on the electron and I_c is the ionic strength. The use of the mean spherical approximation is suitable to dilute micelle solution where the elliptical shape of the micelles is approximately a sphere.

The hard-sphere volume fraction was independently calculated using the following expression taken from Griffiths *et al.* [27] (equation 2.33).

$$\phi_{Hard-Sphere} = \left(\frac{4\pi R_{eq}{}^3}{3}\right)\left(\frac{[Conc]N_a}{N_{agg}}\right) \qquad 2.33$$

Where R_{eq}, is also the equivalent sphere radius of an ellipse ($R_{eq} = x^{1/3}b$, where x is the ellipticity of the CTAB micelle and b is the semi-major axis of the CTAB micelle).

Modelling the CTAB scattering data revealed information about the size and shape of the micelles. The aggregation number was calculated using the following expression shown as equation 2.34.

$$N_{Agg} = \frac{MicelleVolume}{CTA^{+}Volume} \qquad 2.34$$

2.5 References

1 Platschek, B.; Petkov, N.; Bein, T., *Angew. Chem. Int. Ed.* **2006,** *45*, 1134.
2 Guo, W. P.; Park, J. Y.; Oh, M. O.; Jeong, H. W.; Cho, W. J.; Kim, I.; Ha, C. S., *Chem. Mater.* **2003,** *15*, 2295.
3 Xiao, S. G.; Yang, X. M.; Edwards, E. W.; La, Y. H.; Nealey, P. F., *Nanotechnol.* **2005,** *16*, S324.
4 Hostetler, M. J.; Wingate, J. E.; Zhong, C. J.; Harris, J. E.; Vachet, R. W.; Clark, M. R.; Londono, J. D.; Green, S. J.; Stokes, J. J.; Wignall, G. D.; Glish, G. L.; Porter, M. D.; Evans, N. D.; Murray, R. W., *Langmuir* **1998,** *14*, 17.
5 Brunauer, S.; Emmett, P. H.; Teller, E., *J. Am. Chem. Soc.* **1938,** *60*, 309.
6 Barrett, E. P.; Joyner, L. G.; Halanda, P. P., *J. Am. Chem. Soc.* **1951,** *73*, 373.
7 Webb, P. A.; Orr, C., *Analytical methods in Fine Particle Technology* micromeritics Instrument Corp.: **1997**
8 Flewitt, P. E. J.; Wild, R. K., *Physical Methods for Materials Characterisation*. Bristol Institute of Physics: **1994**
9 Berton, E. P., *Introduction to X-Ray Spectrometric Analysis*. Plenum Press: New York: **1978**
10 Hanrahan, J. P.; Copley, M. P.; Ziegler, K. J.; Spalding, T. R.; Morris, M. A.; Steytler, D. C.; Heenan, R. K.; Schweins, R.; Holmes, J. D., *Langmuir* **2005,** *21*, 4163-4167.
11 King, S., *Chp. 7, Small- Angle Neutron Scattering*. John Wiley & Sons Ltd.: **1999**
12 Fratzl, P., *J. Appl. Cryst.* **2003,** *36*, 397.
13 Morttensen, K., *J. Phys.: Condens. Matter* **1996,** *8*, A103.
14 Yang, L.; Alexandridis, P.; Steytler, D. C.; Kositza, M.; Holzwarth, J. F., *Langmuir* **2000,** *16*, 8555.
15 Goldmints, I.; Yu, G. E.; Booth, C.; Smith, K. A.; Hatton, T. A., *Langmuir* **1999,** *15*, 1651.
16 Mortensen, K.; Pedersen, J. S., *Macromolecules* **1993,** *26*, 805.
17 Percus, J. K.; Yevick, G. J., *J. Phys. Rev* **1958,** *110*, 1.
18 Kinning, D. J.; Thomas, E. L., *Macromolecules* **1984,** *17*, 1712.
19 Heenan, R. K. *FISH Data Analysis Program*; Rutherford Appleton Laboratory Report RAL 89-129: Didcot, U.K., 1989.
20 Aswal, V. K.; Goyal, P. S., *Phys. Rev. E: Stat. Nonlinear Soft Matter Phys.* **2000,** *61*, 2947.
21 Quirion, F.; Magid, L. J., *J. Phys. Chem.* **1986,** *90*, 5435.
22 Griffiths, P. C.; Paul, A.; Heenan, R. K.; Penfold, J.; Ranganathan, R.; Bales, B. L., *J. Phys. Chem. B* **2004,** *108*, 3810.
23 Hayter, J. B.; Penfold, J., *Mol. Phys.* **1981,** *42*, 109.
24 Hansen, J. P.; Hayter, J. B., *Mol. Phys.* **1982,** *46*, 651.
25 Hayter, J. B.; Penfold, J., *Coll. Polym. Sci.* **1983,** *261*, 1022.
26 Penfold, J.; Staples, E.; Thompson, L.; Tucker, I.; Hines, J.; Thomas, R. K.; Lu, J. R.; Warren, N., *J. Phys. Chem. B* **1999,** *103*, 5204.
27 Griffiths, P. C.; Paul, A.; K.;, H. R.; Penfold, J.; Ranganathan, R.; Bales, B. L., *J. Phys. Chem.* **2004,** *108*, 3810.

Chapter 3

Swelling of Liquid Crystal Films

3.1 Abstract

The influence of supercritical carbon dioxide and pressurised propane gas on the structural properties of both ionic and non ionic surfactant-based liquid crystal films is discussed in this chapter. The liquid crystal solution was applied as a film but can essentially be described as a sample of bulk liquid crystal solution. Swelling of the liquid crystal films, measured using *in-situ* small-angle neutron scattering (SANS), was found to be dependent on the solubility of the propane/carbon dioxide in micelles of the respective liquid crystals. Additionally, under certain pressure conditions the structural properties of some of the films were observed to change, ultimately leading to the loss of order in the micellar arrays of the liquid crystals.

3.2 Introduction

Amphiphilic block copolymer liquid crystals have emerged as cheap and valuable supramolecular templates for mesostructured materials possessing long-range order. Liquid crystal templating methods have been developed by a number of research groups to prepare stable mesoporous materials from short chain ethylene oxide surfactants, for example in Attard *et al.* [1]. Liquid crystals of tri-block copolymers containing poly(ethylene oxide) (PEO) and poly(propylene oxide) (PPO) segments have also been used in the synthesis of mesoporous silica in the past [2, 3].

Pluronic block copolymer surfactants are ideal as mesoporous templates as they are cheap and readily available due to their use in numerous commercial applications such as the pharmaceutical and cosmetic industries as cleaning, antifoaming and thickening agents. Liu *et al.* [4] reported the synthesis of thiol functionalised mesoporous silica template from the hexagonal liquid phase of Brij 56. El-Safty *et al.* [5] also produced ordered mesoporous silica templated from the liquid crystal phase of Brij 76. Mesoporous membranes were prepared from the liquid crystal phase of C_{12}TAB or C_{16}TAB in Klotz *et al.* [6].

Swollen liquid crystals (SLCs) of cetylpyridinium chloride, sodiumdodecyl sulfate and cetyltrimethylammonium bromide have been utilized in the production of nanotemplated materials such as Zirconia nanoneedles and ZnSe nanomaterials by dos Santos *et al.* [7, 8].

Liquid crystals are also used as potential drug delivery vehicles. Makai *et al.* [9] investigated the use a lamellar structured Brij 96 liquid crystal for the delivery and controlled release of poorly

water soluble drugs. Other liquid crystalline systems of interest in drug release include the cubic phase of glyceryl monooleate which was investigated by Shah *et al.* [10], due its robust and stable cubic structure offering protection to enzymes in the gastric environment and provides delayed and controlled release with no initial concentration burst after oral administration. Yusuf *et al.* [11] utilized low molecular weight liquid crystals (4-n-pentyl-4-cyanobiphenyl and 4-methoxy-benzilidene-4butyl-naniline) to swell thin films of polymethyl-hydrogen-siloxane.

The ability of liquid crystals to absorb significant amounts of gas and consequently swell when subjected to high-pressure gases is crucial to liquid crystal processing and the production of novel nanoscale materials. Swelling liquid crystals affords opportunities for the synthesis of novel materials with controllable size and structures which in turn could control the optical or electronic properties of nanoscale materials. In this chapter the swelling of liquid crystals templated from both ionic and non ionic surfactants with sc-CO_2 and propane gas is investigated.

3.3 Experimental

3.3.1 Supercritical Fluids

A supercritical fluid (SCF) is a compound, mixture or element that is above its critical points, both its critical temperature C_T and critical pressure C_P, both of which are characteristic of the material and are below the pressure and temperature required to condense it into a solid. The critical points depend on the intermolecular attractions between the gas molecules that will drive the condensation of a gas and the thermal energy that the gas possesses as a result of the movement of gas molecules. Supercritical fluids may be considered as high pressure gases that cannot condense to a liquid even if its density is increased. At high temperatures the thermal movement is greater than the attractive forces felt between the gas molecules which make it impossible for the gas to condense. However as the density increases the mean intermolecular distance decreases and the molecular distribution resembles that of a liquid, but the molecular movement resembles that of a gas. This is why the supercritical state is considered to be between that of a liquid and a gas, with diffusivity comparable to that of a gas but with solubility of a liquid [12]. The density, diffusivity/surface tension, polarity, solubility and viscosity of an SCF may all be altered by changing either the temperature or the pressure. Carbon dioxide and nitrous oxide, with their easily reachable critical points [13] are often employed as supercritical fluids. In this chapter liquid crystal films are exposed to supercritical carbon dioxide (sc-CO_2) at various pressures and the resulting changes in the spacing between the neighbouring micelles are determined using SANS.

3.3.2 Experimental Design and Sample Description

A number of experiments were designed to study to effects that various environmental conditions would have on the micellar d-spacing of Pluronic F127 Liquid crystal. A stock F127 micelle solution, which consisted of 50 wt% of surfactant (F127, Brij 56 or CTAB) in D_2O, was prepared 2 hours before any SANS measurements were conducted. Previous studies from the literature show that at these conditions (40°C) a 50 wt% aqueous solution of F127 is comprised of a single cubic mesophase [14], a 50 wt% aqueous solution of CTAB [15] and Brij 56 [16] both consists of a single hexagonal phase. The surfactant was dissolved in the D_2O while stirring at room temperature. The resultant highly viscous surfactant (either F127, Brij 56 or CTAB) in D_2O paste was place on the inside window of the high pressure cell and allowed to equilibrate for up to 30 minutes before the experiment was conducted. All scattering data was normalised by LOQ beamline scientist Dr. Richard Heenan.

3.4 Results and Discussion

Figures 3.1(a), (b) and (c) show the effect of increasing supercritical carbon dioxide (sc-CO_2) pressure has on the neutron scattering pattern of the liquid crystals of the Pluronic surfactant F127, the non-ionic surfactant Brij 56 and the ionic surfactant CTAB respectively. The narrow scattering peak observed in all scattering pattern suggests a single liquid crystal phase. With increasing CO_2 gas and sc-CO_2 pressure the d-spacing between the liquid crystal micelles increases for all three liquid crystal samples as observed by the shift of Q_{max} to lower Q values. Structural data of the liquid crystal micelles would require greater investigation of the morphology of each liquid crystal which was not undertaken here. Since the swelling of the aqueous phase of the micelle is minimal (the solubility of CO_2 in water is negligible) this increase in the d-spacing can be attributed solely to an increase in the micelle to micelle distance as the volume of the non-aqueous phase of the micelles swells with the uptake of CO_2. The corresponding increase in d-spacing obtained, by application of equation 3.1 [17] to the Q_{max} SANS data of Figure 3.1, is shown as a function of sc-CO_2 pressure Figure 3.2.

$$d = \frac{4\pi}{Q_{MAX}\sqrt{3}} \qquad (3.1)$$

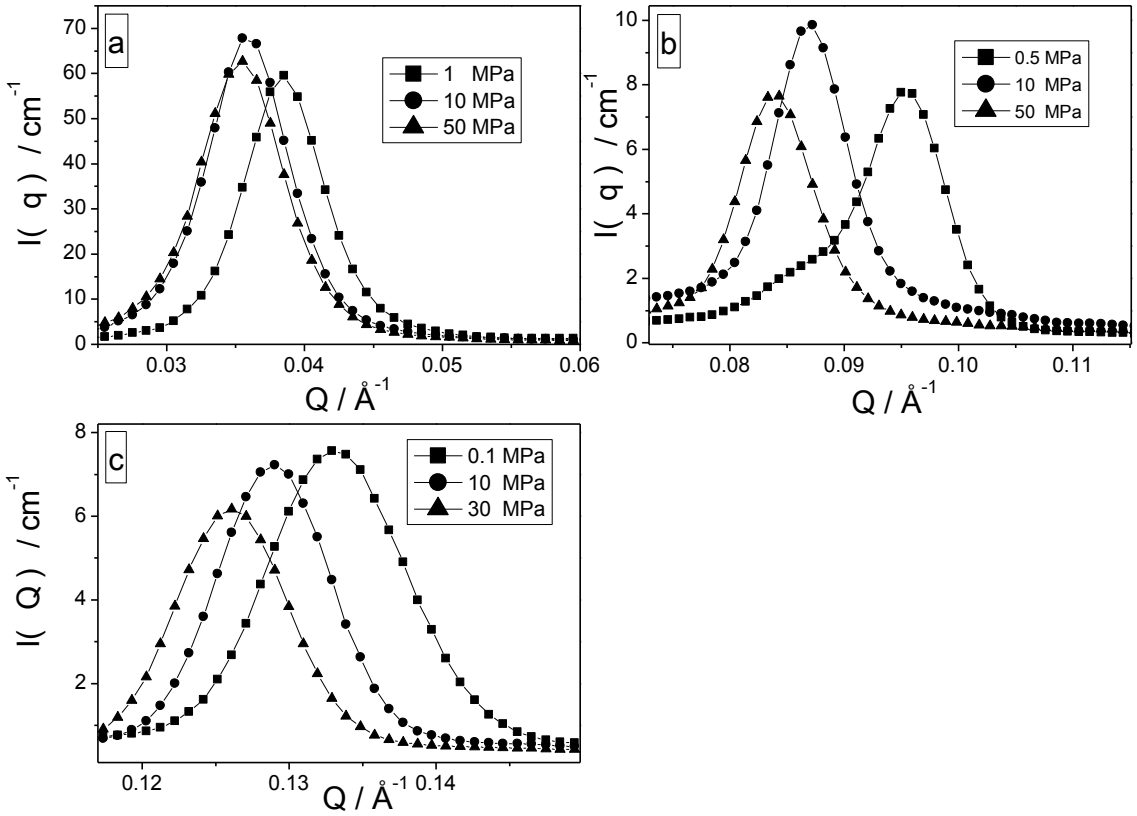


Figure 3.1 SANS scattering pattern observed for different surfactants in CO_2 and sc-CO_2 atmosphere at selected pressures. (a), (b) and (c) show the effects of sc-CO_2 pressure on the F127, Brij 56 and CTAB liquid crystals respectively

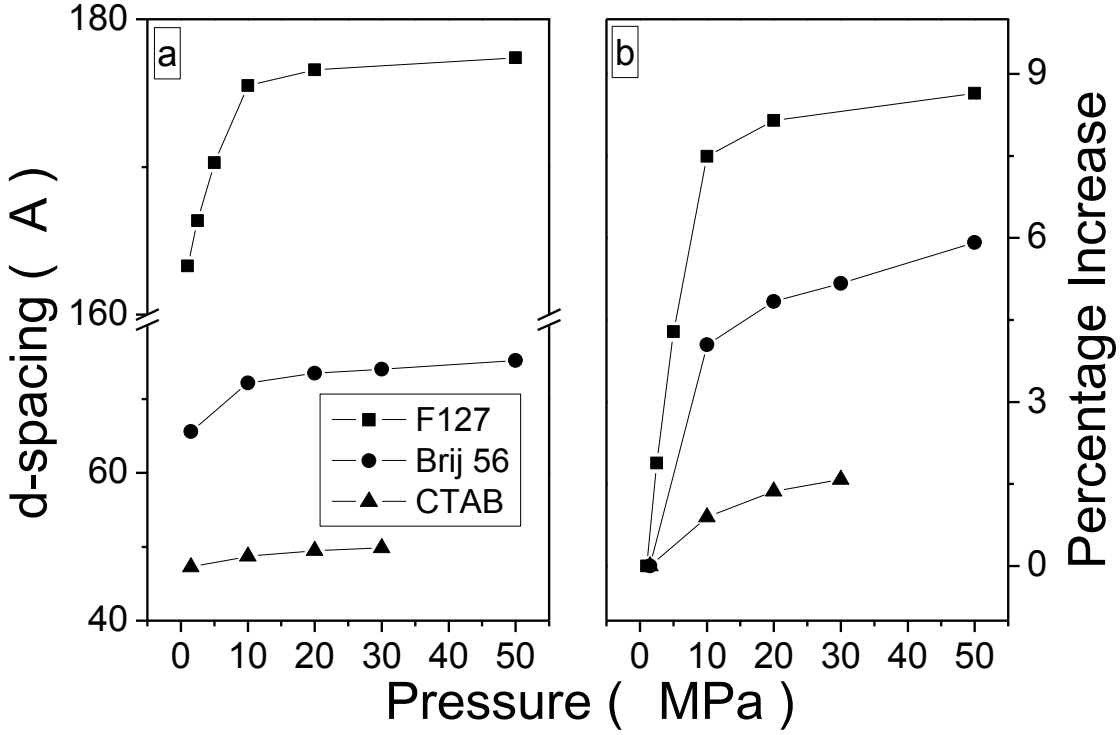


Figure 3.2 An overview of structural changes observed in the liquid crystals under CO_2 and sc-CO_2 pressure. Figure 3.2(a) shows the changes in d-spacings of the F127 (■), Brij 56 (●) and CTAB (▲) liquid crystals in sc-CO_2 at 40°C. Figure 3.2(b) shows the percentage increase in d-spacing (same legend) for the liquid crystal under the same conditions.

3.4.1 F127 CO_2 Swelling

From Figures 3.2(a) and Figure 3.2(b) it can be seen that the initial swelling of the F127 liquid crystal in CO_2 is represented by a d-spacing increase from 0.163 Å to 0.175 Å upon increasing the pressure from 0.1 MPa to 10 MPa respectively, corresponding to a percentage increase of 7.4 %. However, the increase in the d-spacing from 10 MPa to 50 MPa is very small, only 1.5 %.

The majority of the swelling takes place before 10 MPa which is consistent with data reported for other Pluronic systems under sc-CO_2 pressure reported by Hanrahran *et al.* [18]. The swelling trend seen in the Pluronic F127 liquid crystal swelling with CO_2 is also seen when the solubility of CO_2 in the liquid crystal of the Pluronic copolymer P123 ($PEO_{20}PPO_{70}PEO_{20}$), which has the same number of PPO units as F127, is investigated, see Figure 3.3.

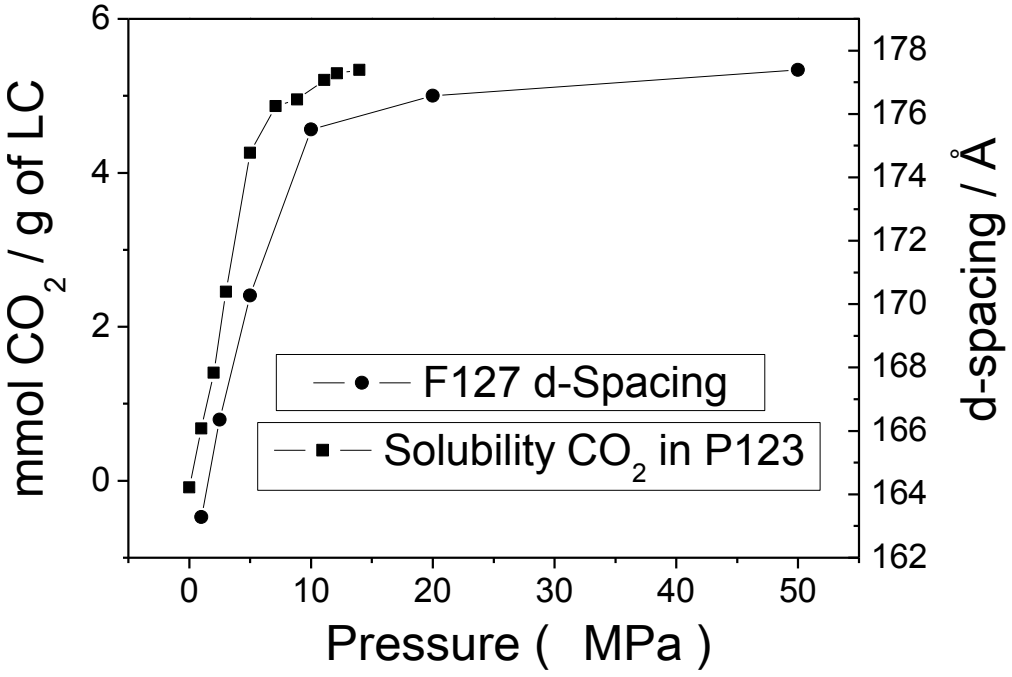


Figure 3.3 The adsorption of CO_2 in a P123 ($PEO_{20}PPO_{70}PEO_{20}$) liquid crystal and d-spacing of the F127 liquid crystal ($PEO_{100}PPO_{70}PEO_{100}$), determined by mass balance experiments.

A CO_2 uptake is seen up to a maximum at 7 MPa, the approximate critical pressure for CO_2, where CO_2 is highly compressible [19, 20]. At higher pressures the solubility is seen to level out, which was also seen by Zhang *et al.* who investigated the sorption of CO_2 and sc-CO_2 in a

variety of block copolymers [21]. This result corresponds well with the SANS data obtained for the F127 liquid crystal indicating that the solubility of the CO_2 in Pluronic surfactant results in the swelling of the liquid crystal micelles. This result also corresponds to SANS data obtained for the swelling of P123 with sc-CO_2 [18].

From the solubility data presented above it can be suggested that the ability of CO_2 to swell the F127 micelle is due to the chemical composition of the micelle, a PPO core surrounded by a PEO corona [22-24]. As with hydrocarbon solubilisation it is mainly in the hydrophobic polypropylene oxide (PPO) micelle core of the micelle that the CO_2 dissolves. It is the CO_2 – ether interactions in the PPO polymer that makes CO_2 so soluble in PPO core [25].

The effect of hydrostatic pressure on the phase of a Pluronic liquid crystal has been reported in the past to induce a melting of the liquid crystal phase [26] but this occurs at pressures twice the maximum pressure reported here. Since CO_2 swells the PPO core of the micelles, the percentage of PPO present in the liquid crystal micelle has a key influence upon the degree of d-spacing increase. A greater extent of micelle expansion is seen in those Pluronic surfactants with a higher ratio of PPO to PEO. This is illustrated in Figure 3.4 for the three Pluronics examined F127 (19%), P85 (25%), P123 (45%) where the % PPO is given in brackets. P85 and P123 swelling data were taken form Hanrahran *et al.* [27].

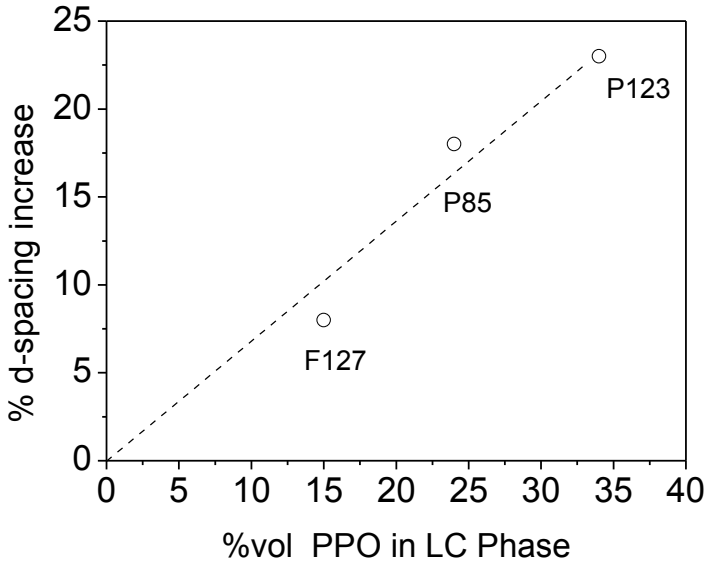


Figure 3.4 Degree of swelling is seen to increase as percentage of PPO in each Pluronic surfactant is increased. The composition of each Pluronic is P123: $PEO_{20}PPO_{70}PEO_{20}$, F127: $PEO_{100}PPO_{70}PEO_{100}$ and P85: $PEO_{26}PPO_{40}PEO_{26}$.

3.4.2 Brij 56 and CTAB Swelling in CO_2

CO_2 swelling of the Brij 56 and CTAB liquid crystals (Figure 1(b) and 1(c) respectively) also show a significant shift of Q_{max} with increasing sc-CO_2 pressure. Swelling of the Brij 56 and CTAB liquid crystals resulted in an increase in the d-spacing of the liquid crystal films by 5.0% and 1.0% respectively at 50 MPa sc-CO_2 pressure. These liquid crystal micelles are comprised of alkyl chain hydrophobic cores and the CO_2 swelling can be partly explained by consideration of the varying solubility of CO_2 in n-alkanes. The solubility of sc-CO_2 in alkanes has previously been reported to decrease as the length of the alkane chain increases [28]. Hence more sc-CO_2 would be expected to dissolve in the core of the Brij 56 (C_{12}) relative to the CTAB (C_{16}) liquid crystal micelles, which is the reflected in the swelling of the liquid crystals by CO_2.

Interestingly, the swelling plateau observed for the F127 liquid crystal in sc-CO_2 is also seen in the Brij 56 and CTAB liquid crystals in sc-CO_2; see Figure 3.2.

3.4.3 Temperature Swelling of F127 in CO_2

As stated above the F127 LC is composed of a hydrophobic PPO micelle core and a hydrophilic PEO corona/interface and it is the CO_2 – ether interactions that makes CO_2 so soluble in PPO core. Figure 3.5 shows the changes in d-spacing of the F127 liquid crystal pressurised to 20 MPa as a function of changing temperature. What is immediately noticeable in Figure 3.5 is the inactive swelling below the critical temperature (T_C) of CO_2 but once the T_C of CO_2 is reached swelling of the F127 liquid crystal micelles begins. It has also been determined that a degree of polarity is necessary to establish CO_2 solubility which is present in the PPO block but lacking in the PEO block [29]. The solubility of CO_2 gas in any polymer system can be explained by the plasticisation effect of CO_2 gas on the polymer [30]. At increased pressure, gas molecules are forced between the polymer chains and expand the spacing between the polymer chains which increases mobility. This results in more gas (or liquid or supercritical fluid depending on the pressure) molecules to be absorbed within the chains once gas pressure is increased [31].

It is thought that the "schizophrenic" nature, *i.e.* density fluctuations between CO_2 in the gas phase and CO_2 in the liquid phase and the tendency of CO_2 to prefer either gas or liquid at near critical conditions [32, 33], is not of concern in this work due to the fact that measurements were not conducted around the critical point of CO_2. Measurements were conducted above and below the critical point. A detailed swelling study around the critical points of CO_2 may illustrate

anomalous swelling and/or CO_2 uptake due to density fluctuation domains in the inhomogeneous fluid.

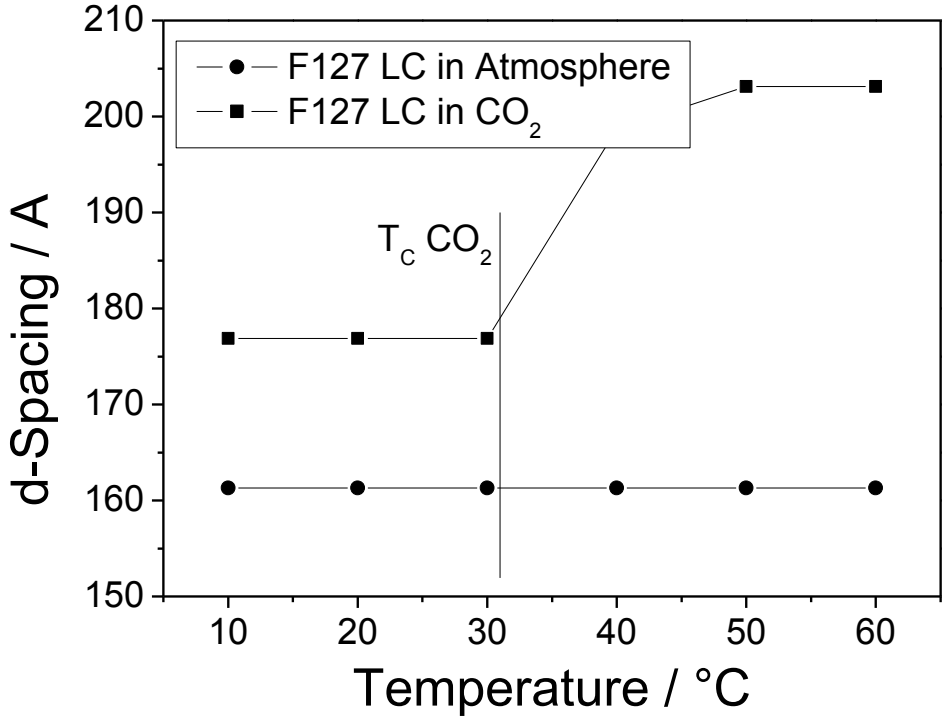


Figure 3.5 The influence of sc-CO_2 (■) on the d-spacing of the F127 liquid crystal as a function of temperature, at a constant pressure of 20 MPa. Also shown (●) is the change in d-spacing of the F127 liquid crystal as a function of temperature in air.

Also shown in Figure 3.5 is the F127 liquid crystal under the same temperature profile but in the absence of CO_2; no change in the micelle d-spacing was observed. Increasing the d-spacing of porous films with CO_2 was also reported by Ghosh *et al.* [34, 35], who reported the increasing of

mesoporous silica thin films synthesised using fluorintated surfactants and post synthesis processing in a pressured CO_2 atmosphere.

3.4.4 Propane Swelling of F127, Brig 56 and CTAB

Figure 3.6(a), (b) and (c) show how Q_{max} for the 50 wt% F127, the Brij 56 and CTAB liquid crystals respectively changes as a function of propane pressure.

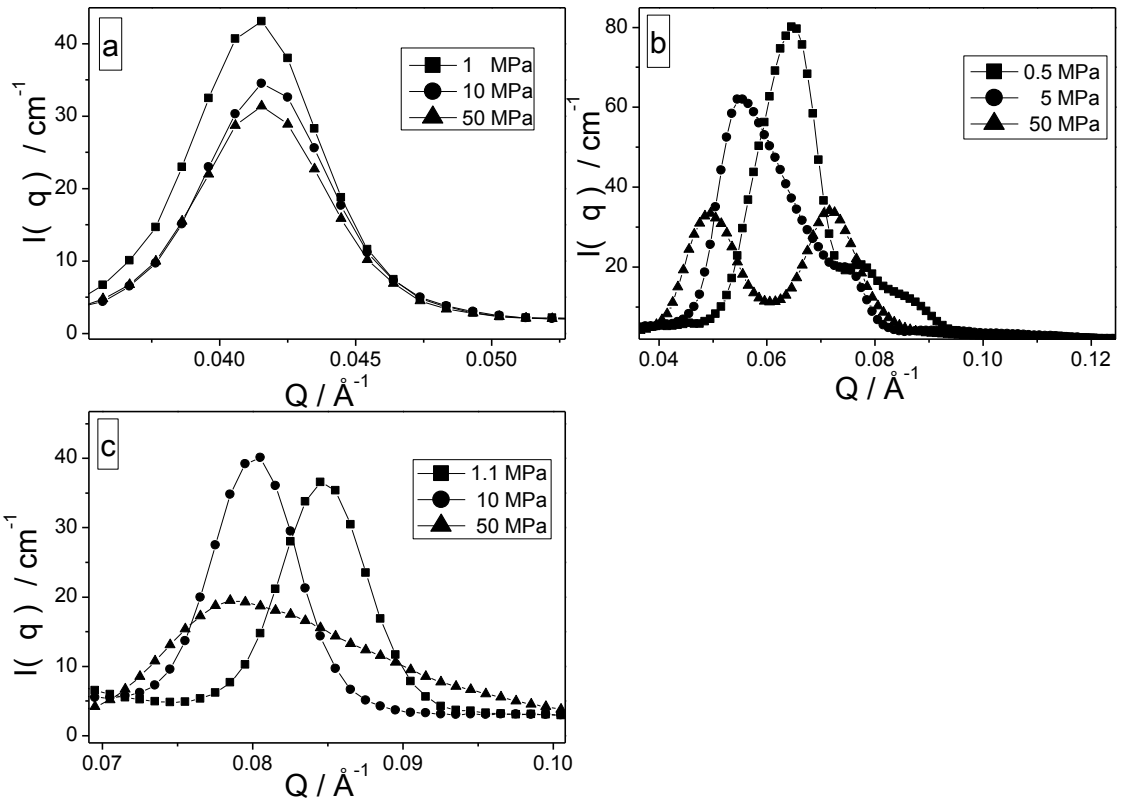


Figure 3.6 SANS scattering pattern observed for different surfactants in a propane atmosphere at selected pressures. Figure 3.6(a), (b) and (c) show the effects of propane pressure on the F127, Brij 56 and CTAB liquid crystals respectively.

3.4.5 Propane Swelling of F127

From the scattering pattern shown in Figure 3.6(a) it is clear that propane has no effect on the F127 liquid crystal micelles since there is no change in d-spacing (Figure 3.7). King *et al.* [36] have previously reported that propane uptake decreases with increasing Pluronic polymer size and since F127 is heavier than the polymer surfactants studied in that report the lack of swelling can be attributed to the low solubility of propane in the heavier Pluronic tri-block copolymer F127.

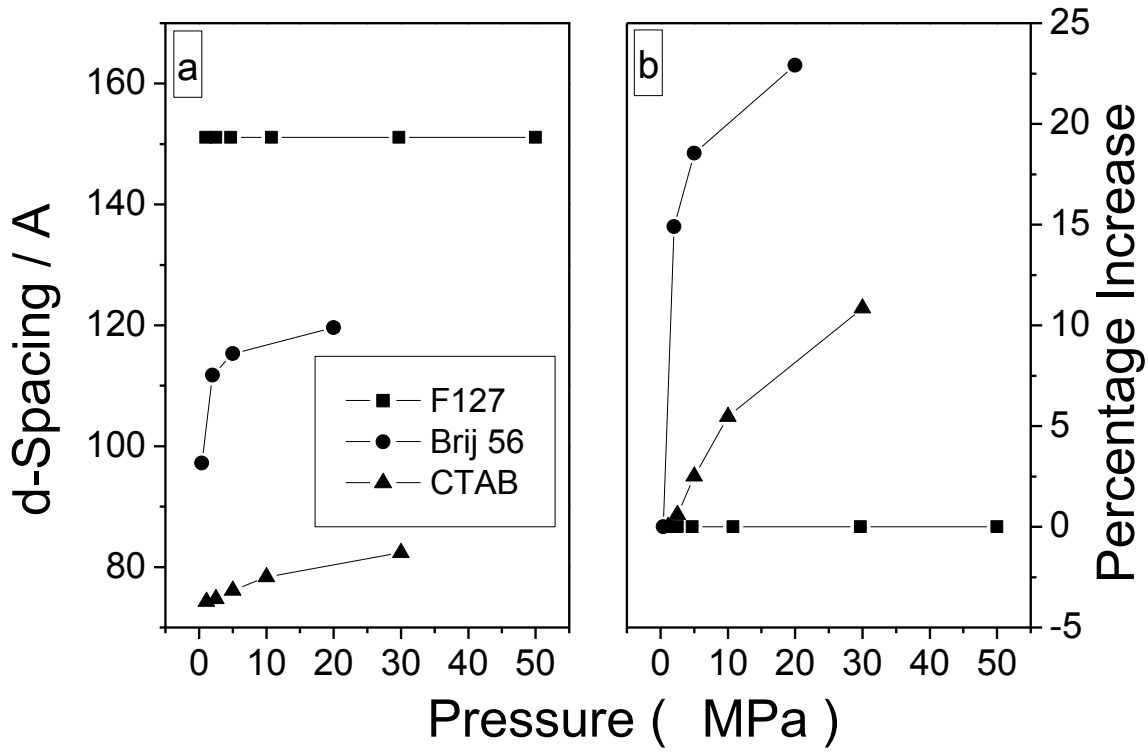


Figure 3.7 An overview of structural changes observed in the liquid crystal under propane pressure. Figure shows the changes in d-spacings of F127 (■), Brij 56 (●) and CTAB (▲) liquid crystal in propane.

3.4.6 Propane Swelling of Brij 56 and CTAB

In contrast Q_{max} was observed to decrease with increasing propane pressure for both the 50 wt% CTAB and Brij 56 liquid crystals, indicating an increase in d-spacing in both liquid crystals. However, after prolonged exposure at high propane pressure both of these liquid crystal templates appear to either destabilise or change in morphology as shown in Figures 3.6(b) and (c). In the case of Brij 56, Q_{max} was observed to split into two separate peaks and lose intensity as the propane pressure was increased in the cell. This peak splitting may be the result of a change in morphology, from hexagonally ordered Brij 56 micelle cylinders to a different arrangement of micelles. Additives to a micellar solution can result in changes of micellar phase and even destabilisation of the micelle system, for example Kumar *et al.* [37] observed changes in SDS solution viscosity after the addition of various alkanols which indicates a morphology change. Also the increased propane pressure may have melting effect (similar to that of reducing the temperature of the liquid crystal) on the liquid crystal phase [26]. The structure of the CTAB liquid crystal was retained until approximately 30 MPa, whereby similar to Brij 56 liquid crystal films, there is a loss of peak intensity and peak shape in the SANS scattering pattern. Shown in Figure 3.6(c) prior to the destabilisation of the CTAB liquid crystal by propane, is a very intense Q_{MAX} peak at approximately 0.084 $Å^{-1}$ at low propane pressure which drastically loses intensity on approaching a pressure of 30 MPa. After prolonged time in the pressurised propane atmosphere the CTAB SANS pattern was almost reduced to background scattering (Figure 3.6(c)). Figure 3.7 shows the changes in d-spacing in the F127, Brij 56 and CTAB liquid crystals with increasing propane pressure before the liquid crystals destabilise.

The differences observed in the amount of swelling in the CTAB liquid crystal when sc-CO_2 and propane gas were used as swelling agents is indicative of the solubility of sc-CO_2 and propane gas in the CTAB liquid crystal. Swelling the CTAB liquid crystal at 30 MPa (sc-CO_2) gives a 2 % increase in d-spacing, compared with a 4.7 % increase in d-spacing at the same pressure for propane. The ability of propane to swell the CTAB liquid crystal to a greater extent can be explained by its increased solubility in the long chain alkane core of the CTAB micelle. The better solubility of propane, compared to CO_2, in CTAB is in agreement to that reported by Roy and co-workers [38], who stated that above the critical micelle concentration (CMC) the degree of solubilisation is greater for propane than it is for CO_2 in both CTAB and sodium dodecylsulphate (SDS).

In the case of the Brij 56 liquid crystal in propane it was shown by Beckman *et al.*, who studied the effect of liquid propane and ethane pressure on the structure of Brij 52 and Brij 30 microemulsions, that as the pressure of propane increases, the affinity of propane to the alkane tail of the Brij surfactants is increased [39]. For this reason it is thought that propane swells the Brij 56 liquid crystal.

3.5 Conclusion

The data presented here demonstrate the swelling of surfactant liquid crystal in supercritical carbon dioxide and propane gas. Small-angle neutron scattering showed the structural changes of the liquid crystals and swelling of the liquid crystals was seen to be dependent on the solubility of propane or sc-CO_2 in the respective liquid crystal micelles. It was also seen that the solubility of CO_2 in Pluronic liquid crystal, which was independently measured, strongly resembled the swelling seen in Pluronic liquid crystal.

Differences were also seen in the stability of the liquid crystals in the propane gas environment. All the liquid crystals were very stable in sc-CO_2. However in propane liquid some of the liquid crystals lost ordering or changed morphology. This was seen as a change in peak shape, peak splitting and loss of peak intensity. This work demonstrates the advantages of using supercritical CO_2 over conventional swelling methods (hydrocarbon swelling) and it is considered that the novel properties of sc-CO_2 play an integral role in the swelling of the surfactant liquid crystal.

3.6 References

1 Attard, G. S.; Glyde, J. C.; Goltner, C. G., *Nature* **1995,** *378*, 366.
2 Huo, Q. S.; Margolese, D. I.; Ciesla, U.; Demuth, D. G.; Feng, P. Y.; Gier, T. E.; Sieger, P.; Firouzi, A.; Chmelka, B. F.; Schuth, F.; Stucky, G. D., *Chem. Mater.* **1994,** *6*, 1176.
3 Huo, Q. S.; Margolese, D. I.; Stucky, G. D., *Chem. Mater.* **1996,** *8*, 1147.
4 Liu, D.; Lei, J. H.; Guo, L. P.; Du, X. D.; Zeng, K., *Microporous Mesoporous Mater.* **2009,** *117*, 67.
5 El-Safty, S. A.; Evans, J., *J. Mater. Chem.* **2002,** *12*, 117.
6 Klotz, M.; Ayral, A.; Guizard, C.; Cot, L., *Sep. Purif. Technol.* **2001,** *25*, 71.
7 dos Santos, E. P.; Santilli, C. V.; Pulcinelli, S. H.; Prouzet, E., *Chem. Mater.* **2004,** *16*, 4187.
8 dos Santos, E. P.; Tokumoto, M. S.; Surendran, G.; Remita, H.; Bourgaux, C.; Dieudonne, P.; Prouzet, E.; Ramos, L., *Langmuir* **2005,** *21*, 4362.
9 Makai, A.; Csanyi, E.; Nemeth, Z.; Palinkas, J.; Eros, I., *Int. J. Pharm.* **2003,** *256*, 95.
10 Shah, M. H.; Paradkar, A., *Int. J. Pharm.* **2005,** *294*, 161.
11 Yusuf, Y.; Ono, Y.; Sumisaki, Y.; Cladis, P. E.; Brand, H. R.; Finkelmann, H.; Kai, S., *Phys. Rev. E: Stat. Nonlinear Soft Matter Phys.* **2004,** *69*, -.
12 Fukushima, Y., *R&D Review of Toyota CRDL 35*,
13 Cansell, F.; Aymonier, C.; Loppinet-Serani, A., *Curr. Opin. Coll. Inter. Sci.* **2003,** *7*, 331.
14 Wanka, G.; Hoffmann, H.; Ulbricht, W., *Macromolecules* **1994,** *27*, 4145.
15 Auvray, X.; Anthore, R.; Petipas, C.; Rico, I.; Lattes, A., *Comptes Rendus De L Academie Des Sciences Serie Ii* **1988,** *306*, 695-698.
16 Coleman, N. R. B.; Attard, G. S., *Microporous and Mesoporous Materials* **2001,** *44*, 73-80.
17 Bacon, G. E., *Neutron Diffraction*. Oxford University Press: **1975**
18 Hanrahan, J. P.; Copley, M. P.; Ziegler, K. J.; Spalding, T. R.; Morris, M. A.; Steytler, D. C.; Heenan, R. K.; Schweins, R.; Holmes, J. D., *Langmuir* **2005,** *21*, 4163-4167.
19 Sirard, S. M.; Green, P. F.; Johnston, K. P., *J. Phys. Chem. B* **2001,** *105*, 766.
20 Sirard, S. M.; Ziegler, K. J.; Sanchez, I. C.; Green, P. F.; Johnston, K. P., *Macromolecules* **2002,** *35*, 1928.
21 Zhang, Y.; Gangwani, K. K.; Lemert, R. M., *J. Supercrit. Fluids* **1997,** *11*, 115.
22 Lettow, J. S.; Lancaster, T. M.; Glinka, C. J.; Ying, J. Y., *Langmuir* **2005,** *21*, 5738.
23 Nagarajan, R., *Colloid Surface B* **1999,** *16*, 55.
24 Sommer, C.; Pederson, J. S.; Garamus, V. M., *Langmuir* **2005,** *21*, 2137.
25 Shen, Z.; McHugh, M. A.; Xu, J.; Belardi, J.; Kilic, S.; Mesoano, A.; Bane, S.; Karnikas, C.; Beckman, E.; Enick, R., *Polymer* **2003,** *44*, 1491.
26 Mortensen, K.; Schwahn, D.; Janssen, S., *Physical Review Letters* **1993,** *71*, 1728-1731.
27 Hanrahan, J. P.; Copley, M. P.; Ziegler, K. J.; Spalding, T. R.; Morris, M. A.; Steytler, D. C.; Heenan, R. K.; Schweins, R.; Holmes, J. D., *Langmuir* **2005,** *21*, 4163.
28 Jha, S. K.; Madras, G., *Fluid Phase Equilibra* **2004,** *225*, 59-62.
29 Rindfleisch, F.; DiNoia, T. P.; McHugh, M. A., *J. Phys. Chem.* **19996,** *100*, 15581.

30 Woods, H. M.; Silva, M. M. C. G.; Nouvel, C.; Shakesheff, K. M.; Howdle, S. M., *J. Mater. Chem.* **2004,** *14*, 1663.
31 Aionicesei, E.; Skerget, M.; Knez, Z., *J. Chem. Eng. Data* **2008,** *53*, 185.
32 Kajimoto, O., *Chem. Rev.* **1999,** *99*, 355.
33 Tucker, S. C., *Chem. Rev.* **1999,** *99*, 391.
34 Ghosh, K.; Vyas, S. M.; Lehmler, H. J.; Rankin, S. E.; Knutson, B. L., *J. Phys. Chem. B* **2007,** *111*, 363.
35 Ghosh, K.; Bashadi, S.; Lehmler, H. J.; Rankin, S. E.; Knutson, B. L., *Microporous Mesoporous Mater.* **2008,** *113*, 106.
36 King, A. D., *J. Colloid Interface Sci.* **2001,** *244*, 123.
37 Kumar, S.; Kirti; Kumari, K.; Kabiruddin, *J. Am. Oil chem. Soc.* **1995,** *72*, 817.
38 Roy, S.; Mehra, A.; Bhowmcik, D., *J. Colloid Interface Sci.* **1997,** *196*, 53.
39 Beckman, E. J.; Smith, R. D., *J. Phys. Chem.* **1990,** *94*, 3729.

Chapter 4

Swelling of Ionic and Non-Ionic Surfactant Micelles by High Pressure Gases

4.1 Abstract

The influence of different environments on the size, shape and characteristics of surfactant micelles of Pluronic F127 and CTAB was investigated by small-angle neutron scattering (SANS). SANS experiments were undertaken on dilute micellar solutions of F127 and CTAB which were exposed to liquid and supercritical carbon dioxide (sc-CO_2), liquid propane, ethane and heptane under various pressures and temperatures. The different swelling from the micelles under the different environments employed could be directly related to the solubility of the solvents in the micelles, especially within the micelle cores. Liquid and supercritical carbon dioxide resulted in the largest swelling of the Pluronic F127 micelles, whilst the less effective swelling by propane and ethane mirrored their poor solubility in the PPO core of the F127 micelle. The effects of solubility were also seen when the swelling of the CTAB micelle was investigated using liquid and supercritical carbon dioxide and propane gas. Greater swelling of the CTAB micelle was achieved using propane rather than liquid and supercritical CO_2, which again reflects the solubility CO_2 and propane in the alkane core of the CTAB micelle.

4.2 Introduction

Surfactant micelles have been extensively studied in the past with many previous studies of micelle systems using small-angle neutron scattering (SANS) [1-6]. SANS is well suited to the characterisation of micellar systems due to the typical size of micelles and their subsequent scattering at low angles. SANS has also been used to show the penetration of oil into micelles using contrast variation experiments [7] and the changes in micellar structure that result with the addition of suitable solvent [8]. Structural studies on Pluronic micelles have been carried out to study the structures and interactions of Pluronic micelles [9-12]. Pluronic polyethylene oxide-polypropylene oxide-polyethylene oxide (PEO-PPO-PEO) tri-block copolymers have found uses in a variety of applications [13], from drug delivery [14-16] to the synthesis of mesoporous materials [17-19]. While exploiting the phase behaviour of Pluronic surfactants (and other types of surfactants) in the synthesis of inorganic mesoporous materials, researchers have found that addition of a suitable swelling agent, such as triethylbenzene [20] or tributylphosphate [21, 22] leads to the formation of unique mesostructures. There have been studies on the uptake of various gases by Pluronic micelles, most notably by King [23-25]. Also studies on the uptake of guest molecules in to Pluronic micelles have been carried out Ruthstein *et al.* [26].

Cetyltrimethylammonium bromide (CTAB) has also found many uses in a variety of applications such as controlling the growth of nanoparticles [27, 28], and as templates in the production of mesoporous materials [29]. The structure of CTAB micelles have also been studied in the past [30, 31], and extensively studied using small-angle neutron scattering techniques; see Aswal *et al.* [32, 33]. The effects of additives on CTAB micellar structure have also been extensively studied using

SANS in the past [34-36]. The addition of oils [36] or different electrolytes [37] to the a CTAB solution alters the structure of the cationic micelle.

High pressure gases such as sc-CO_2 and appropriate hydrocarbons were selected due to their use in other swelling studies conducted in Chapter 3 of this thesis. The unique properties of sc-CO_2, which in the past has shown the swelling effects on Pluronic liquid crystals [38] was thought to have similar effects on the micelles of F127.

In this Chapter a structural investigation is carried out to determine the effects that high pressure atmospheres (sc-CO_2 and selected hydrocarbons) have on the micelle structure of the Pluronic F127 and CTAB micelles. *In-situ* high pressure SANS measurements were conducted on micellar solutions of F127 and CTAB and using an appropriate core-shell mathematical model for the F127 micelle scattering as outlined in Chapter 2, the neutron scattering form the swollen micelles was modelled and information concerning the size, shape and composition of the micelles was determined. The CTAB micelle scattering was modelled using a well used ellipsoidal charged particle model.

4.3 Experimental

4.3.1 Sample Description

In-situ high-pressure SANS experiments was conducted on the LOQ instrument at ISIS at the Rutherford Appleton Laboratory (RAL) in Oxfordshire, UK. All measurements were conducted at 40°C using a high pressure SANS cell described in detail in Chapter 2. A stock solution of the micellar solution, which consisted of 2.5 wt% surfactant (either F127 or CTAB) in D_2O was prepared 2 hr before any SANS measurements were conducted. The surfactant was dissolved in D_2O while stirring at room temperature before being placing in the high pressure cell. The high pressure cell and aqueous micellar solution were allowed to equilibrate, at both the desired temperature and pressure, for up to 30 min before any SANS data was collected.

A least square fitting routine was used to model the F127 micelle scattering data using a core-shell mathematical model, which is also described in Chapter 2. The modelled micelle parameters were the core radius R_1, the micelle radius R_2, the hard sphere radius R_{HS}, the volume fractions of the core components (PPO, water and swelling solvent) and the micelle volume fraction. The aggregation number of the micelle was calculated from a constant micelle core surface area per F127 molecule.

The fitting program FISH [39] was used to model the scattering data from CTAB micelles. The model that was chosen to fit the CTAB data was a Hayter-Penfold charged particle with an elliptical morphology, which is the model of choice when fitting scattering data from CTAB micelles [33, 40]. The fitted CTAB micelle parameters were the semi-minor axis of the ellipitical

CTAB micelle *a*, the ellipicity of the CTAB micelle *X* and the hard sphere radius R_{HS}. All data was normalised by the LOQ beamline scientist Dr. Richard Heenan.

4.4 Results and Discussion

4.4.1 Swelling F127 Micelles with Carbon Dioxide

Figure 4.1(a) shows the fitted SANS data obtained from a CO_2-swollen 2.5wt% F127 aqueous micellar solution at various pressures. A significant change was observed in the isotropic micelle scattering as the pressure of CO_2 was increased, at a constant temperature of 40°C, which can be attributed to (i) an increase in the mean radius of the F127 micelles with increasing CO_2 pressure, (ii) a decrease in the degree of hydration of the micelle core or (iii) an increase in the micellar number density. From the analysis of the SANS data, and previous experience with other Pluronic systems it was concluded that the increase in *I(q)* intensity is due to an increase in the mean radius of the F127 micelles.

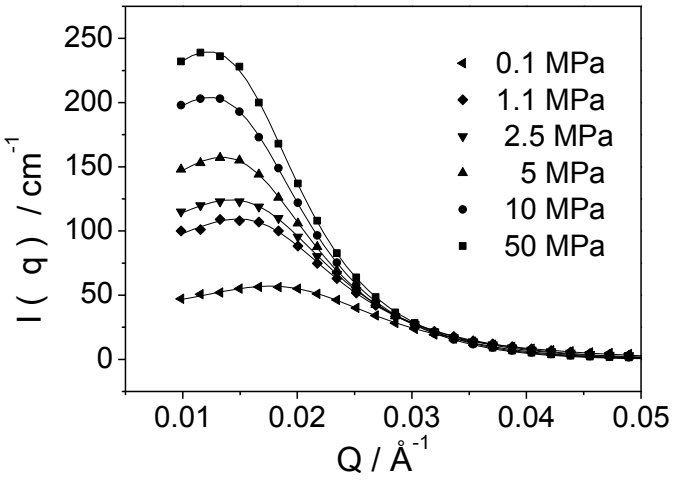


Figure 4.1 Figure 4.1 shows the collected (symbols) and fitted (solid line) SANS data for a 2.5wt% F127 aqueous micellar solution under various CO_2 pressures at 40°C.

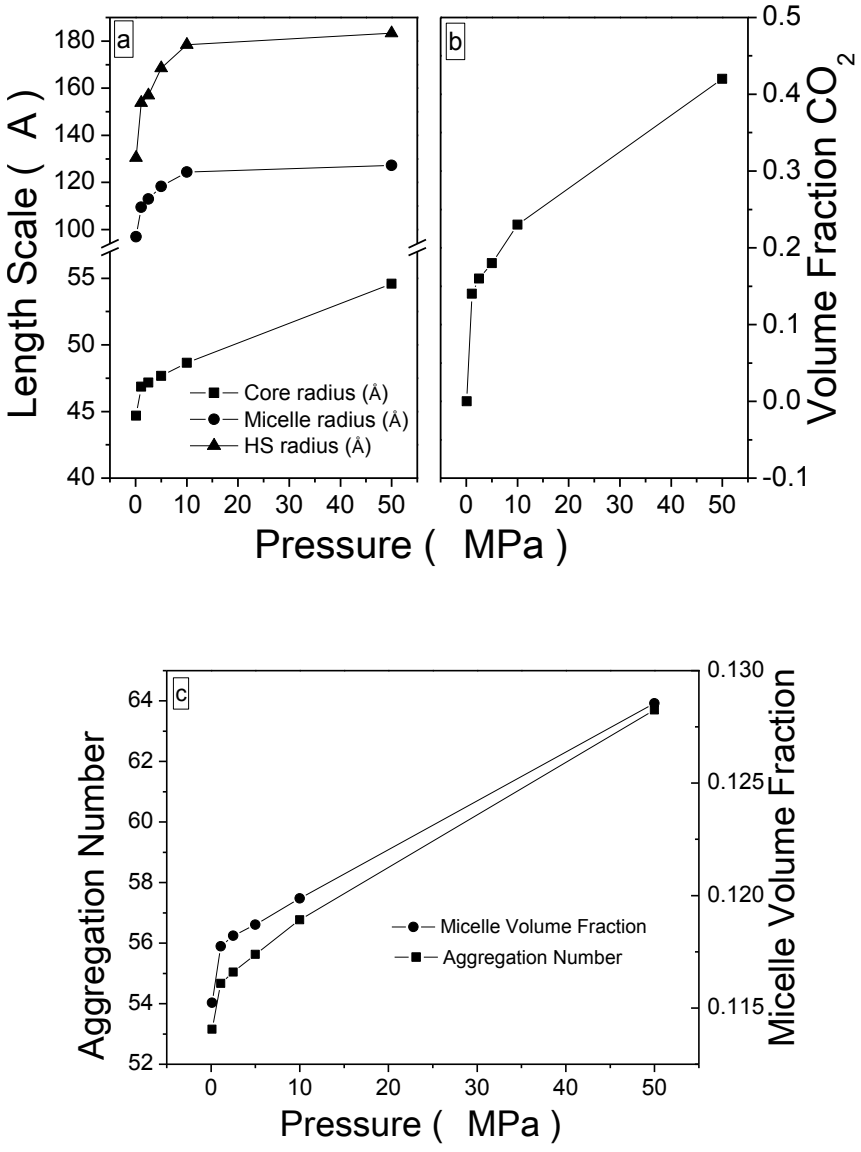


Figure 4.2. Figure 4.2(a) shows the micelle dimensions obtained from the fitting of the data in Figure 4.1. Shown are the core radius R_1, the micelle radius R_2 and the hard sphere radius R_{hs}. Figure 4.1(b) shows the fitted CO_2 volume fractions in the core of the micelle. Figure 4.2(c) shows the fitted micelle volume fraction and the fitted aggregation number for the F127 micelles as a function of CO_2 pressure.

Figure 4.2(a) shows the micelle dimensions core radius (R_1), the micelle radius (R_2) and the hard-sphere radius (R_{hs}) and Figure 4. 2(b) shows the volume fraction of CO_2 in the core of the micelle as a function of pressure obtained by fitting the SANS data at different sc-CO_2 pressures for the swollen F127 micelles. The core radius, consisting of PPO and the corona-core-corona radius, consisting of both PEO and PPO groups and the hard-sphere S(Q) radius show an increase with increasing CO_2 pressure. The core radius was observed to increase from a value of 44 Å at atmospheric pressure, to a value of 54 Å at 50 MPa.

The swelling profile seen in Figure 4.2(a) is very similar to data published in the past where the swelling of the Pluronic micelles with CO_2 is most effective up to approximately 10 MPa and after which the swelling is not as dramatic, even though the density of CO_2 continues to increase at higher pressure [41]. As has been previously reported [42] micellar swelling is due to the solubility of CO_2 in the Pluronic micelles, more specifically the solubility of CO_2 in the micelle hydrophobic polypropylene oxide (PPO) core, which is similar to hydrocarbon solubilisation in Pluronic micelles [23]. Figure 4.2(c) shows an increase of CO_2 in the micelle core as a function of pressure, which was also observed by Sato *et al.* [43] who reported the solubility of CO_2 in PPO increases with pressure. The corresponding micelle radius (R_2) also increases during the experiment but is not thought that the PEO block takes part in the swelling process, however the corona thickness is surprisingly small especially seeing as it is composed of on average 100 PEO units. The large number of PEO units present in the corona of the micelle results in the interface between the hydrated PEO shell and the D_2O solvent phase being poorly defined, in terms of scattering length densities (SLDs) as say compared to the core-corona interface. The boundary between the PEO corona and the solvent becomes blurred as the PEO chains disperse in the

solvent phase, which is consistent with the Pluronic micelle model of a dense PPO core with a highly hydrated PEO corona [44]. This poorly defined interface ultimately results in an inaccurate corona thickness.

The hard sphere S(Q) radius (R_{hs}) is also observed to increase consistently as the pressure increases (Figure 4.1(c)). The micelle volume fraction of the F127 micelle at room pressure and 40° C is in agreement with previous reports for low wt% F127 micellar solutions [45] and is seen to increase from 0.11 to 0.13 during the course of the experiment which is consistent with a micelle of increasing volume.

Assuming that any increase in the micellar volume is solely due to the uptake of CO_2 into the micelle core then aggregation number was seen to increase from a value of 53 at atmospheric pressure to 63 at 50 MPa, see Figure 4.2(c). The larger aggregation number reported here is a characteristic of the larger micelles observed. An aggregation number of 44 for F127 micelles at 40°C has previously been reported by Rassing *et al.* [46] and an aggregation number of 35 for F127 micelles under similar conditions in the article by Nagarajan [47].

4.4.2 Swelling F127 Micelles with Propane and Ethane

Figures 4.3(a) and 4.3(b) show both the experimental and modelled SANS data from propane and ethane swollen micellar solutions of F127 as a function of pressure. The SANS patterns obtained from the ethane swollen micelles have a more pronounced peak compared to those obtained when using propane as the solvent, indicating a greater interaction between

neighbouring micelles during the ethane experiments. It is worth noting that above 5 MPa (approx) ethane becomes supercritical.

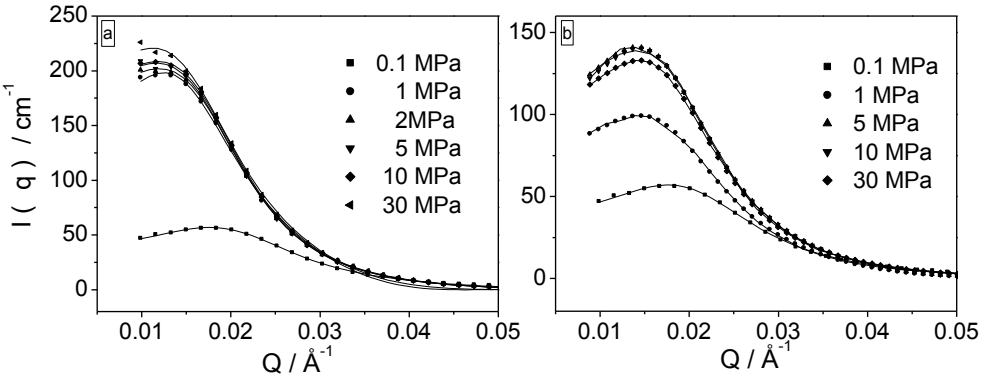


Figure 4.3 Figure 4.3(a) and 4.3(b) shows the collected (square dots) and fitted (solid line) SANS data for a 2.5wt% F127 aqueous micellar solution under various propane and ethane pressures respectively at 40°C.

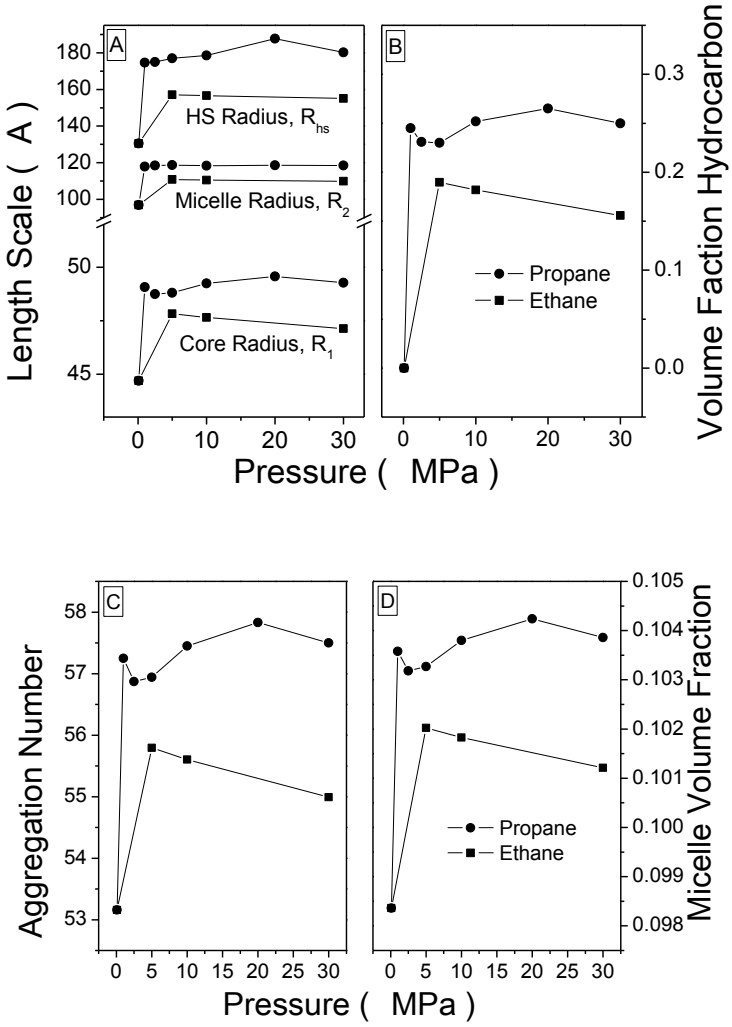


Figure 4.4. Figure 4.4(a) shows the resulting micelle dimension obtained from the fitting of the data in Figure 4.3(a). Shown in Figure 4.4(a) is the core radius (R_1), the micelle radius (R_2) and the hard-sphere radius (R_{hs}) of the F217 micelle. Figure 4.4(b) shows the volume fraction of hydrocarbon taken up by the F127 micelle. Figure 4.4(c) shows the micelle aggregation number at different pressures, while Figure 4.4(d) the changing micelle volume fraction with pressure. Ethane experiments are (■) and propane experiments are (●) in all graphs in Figure 4.4.

It has been reported that heavier hydrocarbons are more soluble in PPO relative to lighter hydrocarbons [23, 24] and is reflected in Figures 4.4(a) through 4.4(d) which show the modelled micelle radii and volume fraction of ethane and propane in the F127 micelle core and the micelle aggregation number and the micelle volume fraction as a function of pressure. Figure 4.4(a) shows the greater swollen micelle core radii (core radius, micelle radius and hard-sphere radius) achieved using the propane compared to using ethane which may also be due to the greater density of propane [48] compared to ethane [49] at the experimental pressures.

The corona thickness remains constant during the swelling process at 60 Å (approx) during both experiments. The trend of greater solubility of the heavier hydrocarbon in the PPO core of the micelle is also shown in the other modelled micelle parameters. Figure 4.4 (b) shows the differences in hydrocarbon uptake in the core of the F127 micelle and it is clearly seen that there is a greater uptake of propane in the core relative to ethane. As with the carbon dioxide experiments there is an increase in the aggregation number in both the ethane and propane experiments as the micelle volume increases with pressure, going from 53 at atmospheric pressure to 57 at 30 MPa during the propane experiments and from 53 at atmospheric pressure to 54 at 30 MPa during the ethane experiments, see Figure 4.4(c). Figure 4.4(d) shows the increasing F127 micelle volume fraction as the hydrocarbon pressure is increased reflecting the increased volume of the micelle as the radius increases with the uptake of hydrocarbon.

4.4.3 Temperature Dependent Swelling of F127 Micelles

SANS data was collected from F127 micellar solutions at 40, 50 and 60°C at atmospheric pressure and at a constant pressure of 20 MPa for ethane, propane and heptane solvents at all temperatures. Figures 4.5(a) to (c) show the changes in the SANS scattering profiles of the F127 micellar solutions as a function of temperature at constant pressure. Initial values of the volume fraction of PPO and water in the micelle core were determined from changing temperature experiments conducted in the absence of any swelling solvent (*i.e.* under atmospheric conditions); these values were then used in the pressurised hydrocarbon temperature experiments. The data obtained from these experiments were used in the pressurized hydrocarbon temperature experiments, where it was assumed that the addition of a hydrocarbon environment to the micellar solution would not alter the degree of hydration of the micelle core or corona.

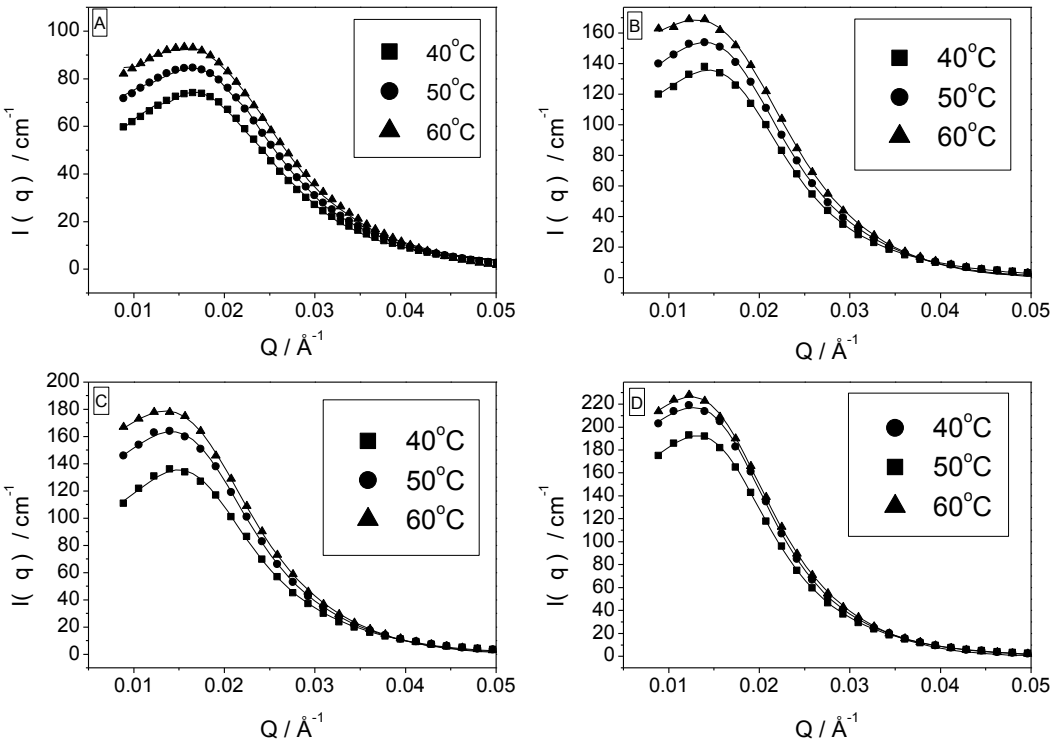


Figure 4.5 SANS data showing the scattering pattern from the F127 micellar solutions as a function of temperature under (a) atmospheric conditions, (b) 20 MPa ethane pressure, (c) 20 MPa propane pressure and (d) under 20 MPa heptane pressure. Collected data is shown as square dots and the modelled profiles are shown as solid lines.

The temperature dependent experiments conducted in the absence of any swelling solvent resulted in well known characteristics of a Pluronic micelle solution at different temperatures, most notably increasing aggregation number with temperature but with very little change in micelle size [50] and an increase in the volume fraction of PPO in the core as the volume fraction

of water in the core decreases. The decreasing volume fraction of water in the PPO core is due to the lower solubility of water in PPO at higher temperatures [51]. The micelle volume fraction is also seen to decrease slightly after 40°C, which has also been observed in previous studies [45] and can be attributed to the decrease in micelle volume as water is lost from the core and corona and dehydration of the PEO and PPO segments at elevated temperatures.

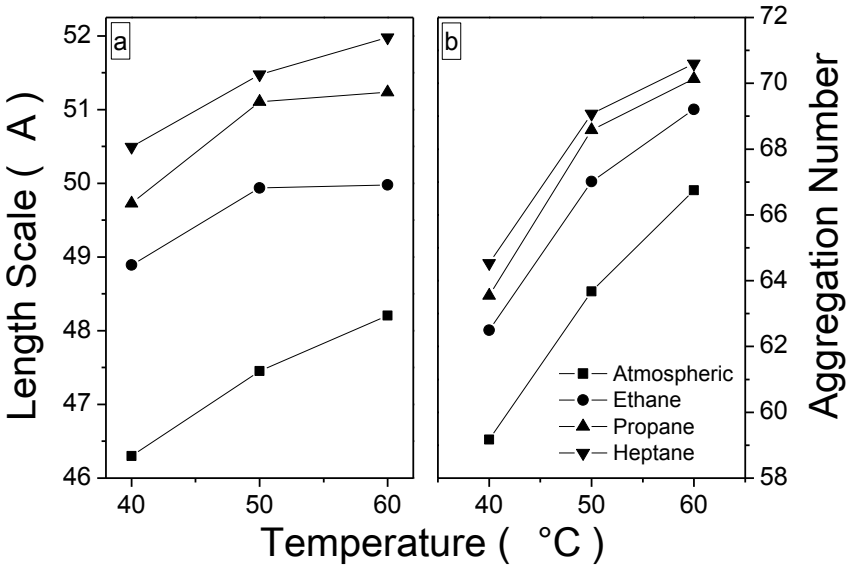


Figure 4.6 Figure 4.6(a) shows the changes in the core radius of F127 micelles over the temperature range between 40 to 60 °C under atmospheric conditions and 20 MPa ethane, propane and heptane pressure. Figure 4.6(b) shows the changing aggregation number of the micelles at different pressures. The same legend can be applied to Figure 4.6(a) and Figure 4.6(b).

Figure 4.6(a) details the small change in the core radius (R_1) of the F127 micelles as a function of temperature, under atmospheric conditions and in ethane, propane and heptane environments. The initial values of R_1 under different solvent environments are insignificant however when

modelling error is taken into account. The mean core radius R_1 is larger for the heavier hydrocarbon solvents, *i.e.* 49 Å for ethane compared to 50.5 Å for heptane, which can be attributed to the different degree of hydrocarbon solubility in the PPO core. From previous studies on which the Pluronic model here is based, the error associated with the core radius is small and in the order of ±0.5 Å [50]. There is also an insignificant change in the aggregation number data shown in Figure 4.6 for the ethane, propane and heptane experiments. The aggregation number does not change because there is very little change in the R_1, which is also shown in Figure 4.6. It should also be noted that the aggregation number is an positive integer. King *et al.* [23] previously showed that the solubility of propane in a Pluronic micellar solution was greater than that of ethane due to the dominant dispersion forces experienced by the heavier hydrocarbons which dictate the solvent-solute interaction of the system. This solubility trend is reflected in the R_1 values obtained for propane and heptane compared to ethane in our experiments. The volume fraction of hydrocarbon in the core of the F127 micelles at each temperature was also calculated and was found to decrease in the following order, $C_7H_{16}>C_3H_8>C_2H_6$, which again reflects the solubility of the various hydrocarbons in the Pluronic micelles. Figure 5(b) shows the increasing aggregation number of the F127 micelles as the temperature is increased, the larger micelles having the greater aggregation number.

4.4.4 CO_2 Swelling of CTAB Micelles

The influence of CO_2 on the structural properties of a 2.5 wt% CTAB micelle solutions at 40°C was also investigated by SANS. SANS measurements were recorded at CO_2 pressures up to 50 MPa. The Hayter-Penfold *S(q)* ellipsoid model as described in Chapter 2 was successfully used

to fit the SANS data from the swollen CTAB micelles as shown in Figure 4.6. The volume fraction of the CO_2 could not be refined using this model, but the fact that the swelling seen by CO_2 is so minimal indicates that any changes in the SLD of the CTAB core with the incorporation of CO_2 would also be minimal.

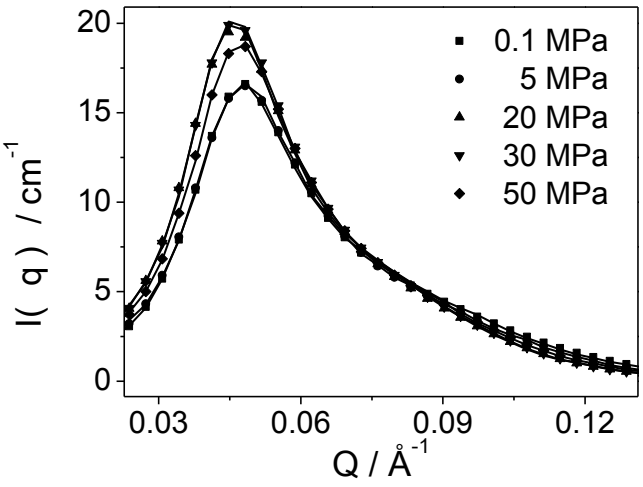


Figure 4.7 Figure 4.7 shows the collected neutron scattering data from CO_2-swollen CTAB micellar solutions at a constant temperature of 40° (black dots) and modelled scattering data (continuous line).

Figure 4.7 shows the changing neutron scattering from the CTAB micellar solution as the CO_2 pressure is increased. The pronounced correlation peak in Figure 4.7 illustrates the strong repulsive interactions experienced between the positively charged CTAB micelles.

Table 4.1 lists some CTAB micelle dimensions obtained from fitting the modelled SANS data shown in Figure 4.7. The size of the semi-minor (a=b<c for a prolate ellipse) axis reported here 23 Å is in agreement with Aswal *et al.* [32]. The size of the micelle remains effectively unchanged

as does the resulting aggregation number, which reflects the very limited uptake of CO_2 into the $C_{16}H_{33}$ core. Very minimal swelling of CTAB with CO_2 was also observed in previous studies, where the swelling of a CTAB templated liquid crystal was also noted to be minimal [42].

Table 4.1 Fitted micelle characteristics as a function of pressure obtained by application of the Hayter-Penfold *S(q)* ellipsoid model to the 2.5 wt% CTAB scattering data seen in Figure 4.6.

	0.1 MPa	5 MPa	20 MPa	30 MPa	50 MPa
a = b (Å)$^{\alpha}$	23	24	26	26	25
X, $c = X.a^{\beta}$	1.65	1.49	1.49	1.48	1.51
H-P *S(q)* Sphere Radius Å$^{\gamma}$	25	24	25	24	23

α: is the semi-minor axis of the ellipitical CTAB micelle
β: is the ellipicity of the CTAB micelle, the closer to unit this is the more spherical the micelle becomes
γ: this is the *S(q)* hard sphere radius

The Hayter-Penfold *S(q)* sphere radius also remains constant throughout this series of experiments, as does the charge on each micelle and the inverse Debye screening length. The constant Debye screening length (43 Å) result is not surprising seeing as no electrolyte was added to the micellar solution during the experiments. The inverse Debye screening length was calculated from Griffiths *et al.* [52] and refined during the modelling process, however the value of the inverse Debye screening length changed very little during modelling, staying approximately 0.023 Å^{-1}. The fractional charge (charge per micelle/aggregation number) was determined to be 0.144 at 0.1 MPa and has an average of 0.146 over all pressures. The micelle dimensions quoted

in Table 4.1 have been determined to be typical of the size, shape and nature of CTAB micelles in a dilute aqueous solution [40, 53].

4.4.5 Swelling of CTAB Micelles with Propane

The effect that liquid propane pressure (the critical points of propane are never reached during these experiments) has on the size, shape and characteristics of the CTAB micelles was also investigated. A very different response was noted from the CTAB micelles when swollen with propane compared to CO_2. Figure 4.8 shows the application of the same model (Hayter-Penfold S(q) ellipsoid model) to a 2.5wt% aqueous CTAB solution under varying liquid propane pressures at 40° C. The correlation peak intensity again indicates the strong repulsive interactions felt between neighbouring micelles. The fitting results obtained for this series of experiments are shown in Table 2.

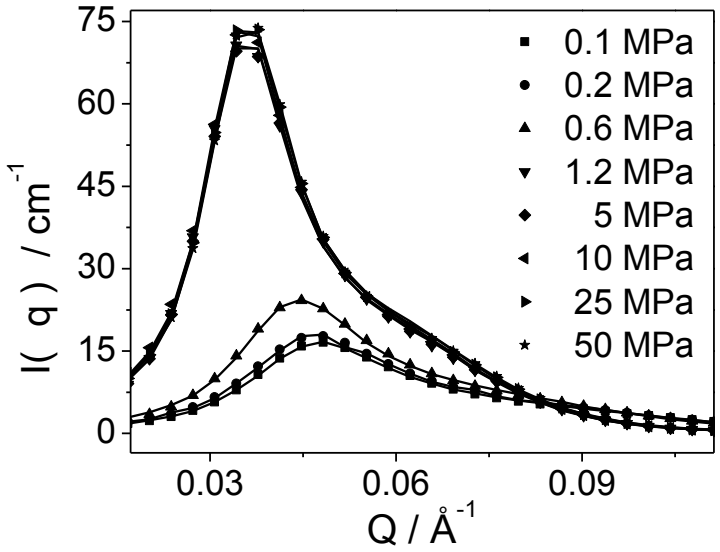


Figure 4.8 Shown here is the collected SANS data (dots) and fitted (solid lines) scattering curves for 2.5wt% aqueous CTAB solution at 40° C under varying liquid propane pressure at 40°C.

From Table 4.2 it is clear that propane has a more substantial effect on the CTAB micelles than CO_2. The increase in the size of the CTAB micelles is a reflection of the high solubility of propane in the C_{16} alkane core of the CTAB micelle compared to CO_2. Hayduk *et al.* [54] showed the higher solubility of propane in hexadecane over CO_2. Roy *et al.* [55] investigated the solubility of a number of non-polar gases including CO_2 and propane in both SDS and CTAB, and reported that the solubility of propane was greatest in both the CTAB and SDS micellar solutions and decreases in the order of propane > ethane > CO_2 > methane. This solubility data mirrors the swelling seen here for both CO_2 and propane.

The other micelle characteristics quoted in Table 4.2 also describe the swelling of the CTAB micelle process which takes place as the propane pressure is increased. The shape of the micelle remains that of a prolate ellipse throughout the whole range of pressures with only a slight decrease in the ellipicity value, which may be due to the change in fractional charge on the micelles as the pressure is increased. Basically these systems become propane in water CTAB stabilised microemulsions.

Table 4.2 The results of the modelled micelle scattering seen in Figure 4.7 at each propane pressure obtained by application of the Hayter-Penfold *S(q)* ellipsoid model to the 2.5 wt% CTAB scattering data.

	0.1 MPa	0.6 MPa	1.2 MPa	4.7 MPa	10 MPa	25 MPa	50 MPa
a = b (Å)$^{\alpha}$	23	26	34	34	35	34	34
X, c = X.a$^{\beta}$	1.65	1.49	1.47	1.47	1.46	1.46	1.47
H-P *S(q)* Sphere Radius Å$^{\gamma}$	25	23	29	29	30	28	28

α: is the semi-minor axis of the ellipitical CTAB micelle
β: is the ellipicity of the CTAB micelle, the closer to unit this is the more spherical the micelle becomes
γ: this is the *S(q)* hard sphere radius

The experiment indicates an increase in the charge per micelle as a result of the greater size of the swollen micelles. The addition of pressurized propane to the CTAB micellar solution is not thought to any neutralising effect that say KCl had in the experiments reported Goyal *et al* [37]. Berr *et al.* [56] proposed that as the ellipitical axial ratio decreases there are less bound counter ions

at the micelle interface, *i.e.* counter ion dissociation is promoted, to accommodate the surfactant head groups moving further apart with changing micelles shape with increasing propane pressure. This increased micelle surface charge is also be responsible for the narrowing of the correlation peak in the neutron scatting pattern as micelles with greater surface charge repulse neighbouring micelles to a greater extent.

4.5 Conclusions

Successful modelling of the SANS data from micellar solutions of F127 and CTAB surfactants using well established models, revealed important details of swelling processes occurring at evaluated pressures and temperatures. Not only was the size of the micelles observed to change but the composition of the micelle was also seen to vary as different swelling solvents were incorporated into the core of each micelle. The compositions of the Pluronic micelle was refined during the modelling process and illustrated the increasing volume fraction of swelling solvent, be it CO_2 or propane, within the core of the micelle. The importance of the solubility of each swelling solvent within the PPO core of the micelle was seen to be the driving force in the micelle swelling. The effect of changing temperature on a micelle solution, already well characterised, was complicated by the addition of a high pressure environment to the system and was successfully taken into account during the modelling process undertaken here. The combination of pressure effects and temperature effects occurring simultaneously were both taken into account when the neutron scattering data was modelled. The interaction between neighbouring micelles was influenced greatly by the conditions each system was placed under. Well characterised results were seen along with unique micelle responses to the changing pressures of the CO_2, sc-CO_2, propane, ethane and heptane environments. Modelling of the ionic CTAB solution also showed interesting results. Not only was the size of the CTAB micelle investigated but also the shape of the micelle was seen to change with varying pressures as a result of the changing cationic character of micelle surface. This is the first time that a change in the ionic character of the CTAB micelle was influenced not by adding different electrolyte but by influencing the shape of the micelle.

4.6 References

1 ChilluraMartino, D.; Triolo, R.; McClain, J. B.; Combes, J. R.; Betts, D. E.; Canelas, D. A.; DeSimone, J. M.; Samulski, E. T.; Cochran, H. D.; Londono, J. D., *J. Mol. Struct.* **1996,** *383*, 3.

2 Full, A. P.; Kaler, E. W., *Langmuir* **1994,** *10*, 2929.

3 Gambi, C. M. C.; Giordano, R.; Chittofrati, A.; Pieri, R.; Baglioni, P.; Teixeira, J., *Appl. Phys. A-Mater. Sci. Processing* **2002,** *74*, S436.

4 Aswal, V. K.; Haldar, J.; Goyal, P. S.; Bhattacharya, S., *Appl. Phys. A-Mater. Sci. Processing* **2002,** *74*, S352.

5 Okamura, H.; Imae, T.; Takagi, K.; Sawaki, Y.; Furusaka, M., *J. Coll. Inter. Sci.* **1996,** *180*, 98.

6 Hollamby, M. J.; Tabor, R.; Mutch, K. J.; Trickett, K.; Eastoe, J.; Heenan, R. K.; Grillo, I., *Langmuir* **2008,** *24*, 12235.

7 Barlow, D. J.; Lawrence, M. J.; Zuberi, T.; Zuberi, S.; Heenan, R. K., *Langmuir* **2000,** *16*, 10398.

8 Causse, J.; Lagerge, S.; de Menorval, L. C.; Faure, S., *Journal of Colloid and Interface Science* **2006,** *300*, 713-723.

9 Bedrov, D.; Smith, G. D.; Yoon, J. Y., *Langmuir* **2007,** *23*, 12032.

10 Roux, A. H.; Douheret, G.; Roux-Desgranges, G., *Colloids and Surfaces a-Physicochemical and Engineering Aspects* **2005,** *252*, 43.

11 Wright, M.; Kurumada, K.; Robinson, B., *Trends in Colloid and Interface Science Xvi* **2004,** *123*, 8-11.

12 Su, Y. L.; Wang, J.; Liu, H. Z., *Macromolecules* **2002,** *35*, 6426.

13 Alexandridis, P.; Hatton, T. A., *Colloids Surf., A* **1995,** *96*, 1.

14 Guzman, M.; Garcia, F. F.; Molpeceres, J.; Aberturas, M. R., *Int. J. Pharm.* **1992,** *80*, 119.

15 Kabanov, A. V.; Batrakova, E. V.; Meliknubarov, N. S.; Fedoseev, N. A.; Dorodnich, T. Y.; Alakhov, V. Y.; Chekhonin, V. P.; Nazarova, I. R.; Kabanov, V. A., *J. Controlled Release* **1992,** *22*, 141.

16 Ugarenko, M.; Chan, C. K.; Nudelman, A.; Rephaeli, A.; Cutts, S. M.; Phillips, D. R., *Oncol. Res.* **2008,** *17*, 283.

17 Baute, D.; Goldfarb, D., *J. Phys. Chem. B* **2007,** *111*, 10931.

18 Ruthstein, S.; Frydman, V.; Goldfarb, D., *J. Phys. Chem. B* **2004,** *108*, 9016.

19 Ruthstein, S.; Frydman, V.; Kababya, S.; Landau, M.; Goldfarb, D., *J. Phys. Chem. B* **2003,** *107*, 1739.

20 Cao, L. A.; Man, T.; Kruk, M., *Chem. Mater.* **2009,** *21*, 1144.

21 Causse, J.; Lagerge, S.; de Menorval, L. C.; Faure, S., *J. Coll. Inter. Sci.* **2006,** *300*, 724.

22 Causse, J.; Lagerge, S.; de Menorval, L. C.; Faure, S., *J. Coll. Inter. Sci.* **2006,** *300*, 713.

23 King, A. D., *J. Coll. Inter. Sci.* **2001,** *244*, 123.

24 King, A. D., *J. Coll. Inter. Sci.* **2001,** *243*, 457.

25 King, M. B.; Kassim, K.; Alnajjar, H., *Chem. Eng. Sci.* **1977,** *32*, 1247.

26 Ruthstein, S.; Raitsimring, A. M.; Bitton, R.; Frydman, V.; Godt, A.; Goldfarb, D., *Phys. Chem. Chem. Phys.* **2009,** *11*, 148.
27 Berhault, G.; Bausach, M.; Bisson, L.; Becerra, L.; Thomazeau, C.; Uzio, D., *J. Phys. Chem. C* **2007,** *111*, 5915.
28 Lu, L.; Kobayashi, A.; Tawa, K.; Ozaki, Y., *Chem. Mater.* **2006,** *18*, 4894.
29 Frasch, J.; Lebeau, B.; Soulard, M.; Patarin, J.; Zana, R., *Langmuir* **2000,** *16*, 9049.
30 Candau, S. J.; Hirsch, E.; Zana, R., *J. Phys. Chem.* **1984,** *45*, 1263.
31 Dorshow, R.; Briggs, J.; Bunton, C. A.; Nicoli, D. F., *J. Phys. Chem.* **1982,** *86*, 2388.
32 Aswal, V. K.; Goyal, P. S., *Chem. Phys. Lett.* **2002,** *357*, 491.
33 Aswal, V. K.; Goyal, P. S., *Phys. Rev. E: Stat. Nonlinear Soft Matter Phys.* **2000,** *61*, 2947.
34 Kuperkar, K.; Abezgauz, L.; Danino, D.; Verma, G.; Hassan, P. A.; Aswal, V. K.; Varade, D.; Bahadur, P., *J. Coll. Inter. Sci.* **2008,** *323*, 403.
35 Goyal, P. S.; Chakravarthy, R.; Dasannacharya, B. A.; Desa, J. A. E.; Kelkar, V. K.; Manohar, C.; Narasimhan, S. L.; Rao, K. R.; Valaulikar, B. S., *Physica B* **1989,** *156*, 471.
36 Prasad, C. D.; Singh, H. N.; Goyal, P. S.; Rao, K. S., *J. Coll. Inter. Sci.* **1993,** *155*, 415.
37 Goyal, P. S.; Menon, S. V. G.; Dasannacharya, B. A.; Rajagopalan, V., *Chem. Phys. Lett.* **1993,** *211*, 559.
38 Hanrahan, J. P.; Copley, M. P.; Ziegler, K. J.; Spalding, T. R.; Morris, M. A.; Steytler, D. C.; Heenan, R. K.; Schweins, R.; Holmes, J. D., *Langmuir* **2005,** *21*, 4163.
39 Heenan, R. K. *FISH Data Analysis Program*; Rutherford Appleton Laboratory Report RAL 89-129: Didcot, U.K., 1989.
40 Quirion, F.; Magid, L. J., *J. Phys. Chem.* **1986,** *90*, 5435.
41 Span, R.; Wagner, W., *Journal of Physical and Chemical Reference Data* **1996,** *25*, 1509-1596.
42 O'Callaghan, J. M.; Copley, M. P.; Hanrahan, J. P.; Morris, M. A.; Steytler, D. C.; Heenan, R. K.; Staudt, R.; Holmes, J. D., *Langmuir* **2008,** *24*, 6959.
43 Sato, Y.; Takikawa, T.; Yamane, M.; Takishima, S.; Masuoka, H., *Fluid Phase Equilib.* **2002,** *194*, 847.
44 Mortensen, K., *Polym. Adv. Tech.* **2001,** *12*, 2.
45 Mortensen, K.; Talmon, Y., *Macromolecules* **1995,** *28*, 8829.
46 Rassing, J.; Attwood, D., *Int. J. Pharm.* **1982,** *13*, 47.
47 Nagarajan, R., *Colloids Surf., B* **1999,** *16*, 55.
48 Miyamoto, H.; Watanabe, K., *Int. J. Thermophys.* **2000,** *21*, 1045-1072.
49 Friend, D. G.; Ingham, H.; Ely, J. F., *J. Phys. Chem. Ref. Data* **1991,** *20*, 275-347.
50 Yang, L.; Alexandridis, P.; Steytler, D. C.; Kositza, M. J.; Holzwarth, J. F., *Langmuir* **2000,** *16*, 8555.
51 Goldmints, I.; vonGottberg, F. K.; Smith, K. A.; Hatton, T. A., *Langmuir* **1997,** *13*, 3659.
52 Griffiths, P. C.; Paul, A.; Heenan, R. K.; Penfold, J.; Ranganathan, R.; Bales, B. L., *J. Phys. Chem. B* **2004,** *108*, 3810.
53 Pal, O. R.; Gaikar, V. G.; Joshi, J. V.; Goyal, P. S.; Aswal, V. K., *Langmuir* **2002,** *18*, 6764-6768.
54 Hayduk, W.; Walter, E. B.; Simpson, P., *J. Chem. Eng. Data* **1972,** *17*, 59.
55 Roy, S.; Mehra, A.; Bhowmick, D., *J. Coll. Inter. Sci.* **1997,** *196*, 53.
56 Berr, S. S., *J. Phys. Chem.* **1987,** *91*, 4760-4765.

Chapter 5

Time resolved SAXS Studies of Periodic Mesoporous Organosilicas in Anodic Alumina Membranes

5.1 Abstract

A method for producing oriented periodic mesoporous organosilica filaments within the confined channels of anodic alumina membranes is presented. Deposition of the mesoporous filaments were performed under a variety of conditions, which favoured the evaporation induced self-assembly of the mesoporous material. The experimental conditions examined included different drying rates, over a range of humidity values, and sol composition, *i.e.* varying amounts of the organosilica component. The deposition process was followed *in-situ* by time resolved small angle x-ray scattering which was essential for evaluating the formation mechanism of the mesophase structures. Through careful control of the deposition environment, the structure and orientation of the mesoporous filaments could readily be varied.

5.2 Introduction

Mesoporous silica can have many different morphologies, including powders and spheres [1], thin films [2] and fibres [3, 4]. Mesoporous thin films offer the most useful morphology due to the parallel orientation of mesopores with respect to the substrate. However without the proper control during the initial synthesis and use of the correct substrates [5], mesoporous thin films are essentially a random collection of domains each with their own pore direction. The preparation of mesoporous thin films via the evaporation induced self assembly (EISA) mechanism, within the confines of an existing structure leads to the formation of mesoporous silica filaments [6, 7]. These filaments possess long range order which cannot be obtained without the use of a confined architecture during synthesis of the mesoporous material. Confinement of mesoporous silica within the architectures of anodic alumina membranes (AAM) has lead to the development of mesoporous silica filaments with long range order induced by the physical confinement within the AAM [6, 8, 9]. AAMs are porous alumina membranes composes of straight channels with varying diameters [10].

Periodic mesoporous organosilicas (PMOs), as stated in Chapter 1 are a very useful class of mesoporous materials. They possess the rigidity and a well ordered pore structure of mesoporous silica with the added functionality and characteristics of an organic bridging unit within the structure [11-15]. PMOs have found use in a wide range of applications including in catalysis, as separation membranes or for templates in the production of nanostructures [16, 17].

In this Chapter the synthesis of PMOs, through a sol-gel process, within the pores of AAMs is described. The effects of the deposition conditions, *e.g.* reduced humidity as well as the organic

– inorganic ratio, on the resultant porous structure were investigated to enable a detailed understanding of the dynamics of the disorder-to-order transitions in these systems and to subsequently control the orientation of the mesostructured phases.

5.3 Experimental

P123 was supplied by BASF. Tetraethyl orthosilicate (TEOS), 2-bis-(triethoxysilyl) ethane (BTESE) were supplied by Sigma-Aldrich. All chemicals were used as received. Ethylene-bridged PMO materials within the AAMs were prepared using a sol-gel method similar to that reported previously by Platschek *et al*. [18]. In a typical synthesis 2.08 g (w/w) of silica (TEOS) and organo-silica (BTESE) precursors, 3 mL of 0.2 M aq HCl, 1.8 mL of H_2O and 5 mL of ethanol were mixed at 60 °C for 1 h. To this solution, 15 mL of a 5 wt% P123 in ethanol was then added and left to stir at room temperature for 1 h, after which the gel was filtered. The gel was then dropped onto a Whatman AAM, with 100 nm pores, until the membrane was completely covered and left to dry under vacuum or in a controlled humidity atmosphere. Dry AAM-PMO composites where calcined at 450°C in air to lift off any excess film material from the surfaces of the membrane. It should be noted that the calcination step also reduces the size of the PMO filament within the AAM pores and adhesion between the PMO filament and the AAM wall is lost. The SAXS experiments were first conducted *ex-situ* on already structured (dry) membranes followed by *in-situ* time resolved experiments on some selected samples. This however resulted in a mesoporous film deposited on top of the membrane which interfered with but did not obstruct the analysis of the mesoporous filament within the AAM channels. This surface film is unavoidable when conducting *in-situ* measurements, where otherwise it would be removed via calcination or polishing.

In-situ SAXS experiments were carried out at the Austrian SAXS beamLine of the ELETTRA Synchrotron facility, Trieste, Italy using an image intensified 2D-CCD-camera (CV12, Photonic Science Ltd, Millham, UK) and 8 keV x-ray energy. The sample to detector distance was 1.478

m. Briefly, the AAMs were completely covered with the PMO gel in a sealed chamber in which the humidity was controlled. In some cases the evaporation rate was accelerated by evacuating the chamber to a reduced pressure of approximately 1 mbar. d-spacings were calculated using a standard (silver behenate) of known d-spacing.

TEM images were collected on a JEOL 2000FX transmission electron microscope operating at a voltage of 200 kV. The membranes were prepared for plan-view TEM imaging by dimple grinding, followed by Ar-ion polishing. The dimple grinding was accomplished using a Gatan model 656 dimple grinder using 5 μm diamond paste. Further Precision Ion Polishing (PIPS) reduces the thickness of the AAM for TEM analysis which was done at grazing angles of 6° with a 5 kV acceleration voltage on a Gatan, Precision ion polishing system model 691.

5.4 Results and Discussion

SAXS measurements of AAMs loaded with a mesoporous material will result in different scattering patterns due to the orientation of the mesostructure within the AAM channels, see Figure 5.1. These scattering patterns are much like those reported for normal mesoporous thin films like those reported by Grosso *et al.* [19, 20]. However due to the confinement effects of the AAM channel different scattering patterns are observed [9, 21, 22]. A very good overview of such x-ray reflections, the responsible structures in direct space and reciprocal space are given in Platschek *et al.* [23] but is briefly repeated here for completeness.

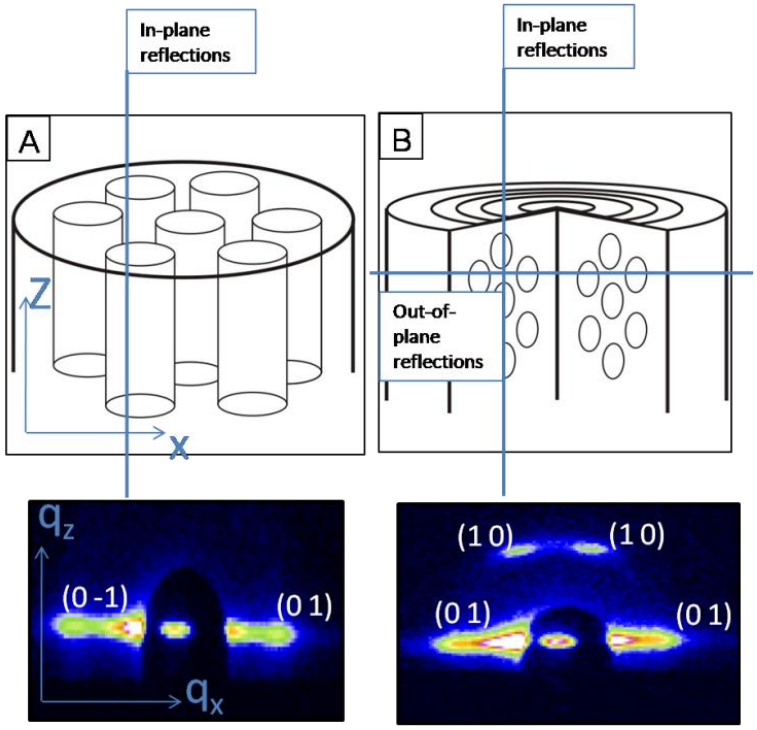


Figure 5.1 Schematics of the mesoporous structures within the channels of AAMs with the corresponding SAXS patterns: (a) columnar hexagonal, (b) circular hexagonal orientated mesoporous structure.

Figure 5.1(a) shows the columnar hexagonal mesoporous structure and the scattering pattern which results from the high rotational symmetry of the columnar structure around the axis of the AAM channels. Figure 5.1(b) illustrates the circular hexagonal mesoporous structure consisting of concentric circles of hexagonally arranged pores wound around the AAM channels, and an example of the resulting scattering pattern from the circular hexagonal pores. The additional scattering spots are hidden from view due to the beam stop. Additionally, a lamellar mesophase (concentric lamellar sheets wound around the axis of the AAM channels) has also been reported [18, 23] however such a structure was not observed in this work. SAXS data was not the only technique used to identify the mesoporous structures present in the AAM channels, as SAXS data may lead to misleading conclusions, so complementary TEM data, similar to that used in Wang *et al.* [24], was used to identify the mesoporous structures within the AAMs.

The EISA mechanism that determines the final structure of a PMO materials can be influenced by many factors [25, 26], none more important than the chemical composition of the deposited gel [27, 28]. Humidity effects play a significant role during the condensation of a silica precursor during the deposition of any mesoporous material. Water is vital to both the condensation of the silica precursor [29] and to the formation of stable micelles of the structure directing agent (in this case P123) above the critical micelle concentration of the structure directing agent [27] and ethanol is widely used during EISA synthesis because of its low vapour pressure [26]. The effect of humidity on the final mesoporous structure within the AAM channels from a sol composed of 50% w/w organosilica precursor and 50% w/w silica precursor measured *ex-situ* is shown in Figure 5.2.

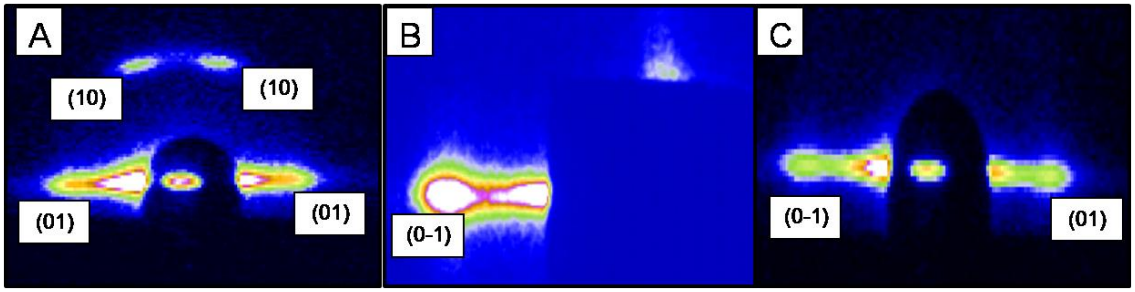


Figure 5.2 The influence of the humidity during the deposition of the mesoporous material from a sol composed of 50% w/w organosilica precursor and 50% w/w silica precursor measured: (a) high humidity (80%), (b) moderate humidity (40%) and (c) low humidity (20%).

The presence of the (10) and (01) scattering spots shown in Figure 5.2(a) indicate both in-plane and out-of-plane scattering resulting from circular hexagonal mesopores within the AAM channels. In contrast samples deposited at reduced humidity show scattering patterns where only the in-plane reflections are present (Figures 5.2(b) and 5.2(c)) which results from the mesopores ordered in a columnar hexagonal fashion. The additional scatting spots are hidden by the beam stop. As explained previously, in order to uniquely identify these structures as columnar, complementary TEM data is required. Figure 5.3 shows plan-view TEM images for two samples deposited at high and low humidity from the same synthetic mixture containing 50% organosilica and 50% silica precursor in the deposited gel. The appearance of a lamellar phase in Figure 5.3(b) cannot be entirely ruled out. The TEM images clearly show that the sample deposited at high humidity is primarily circular phase whereas the sample prepared at reduced humidity has largely columnar pores. In both cases a partial mixture of phases exists. In Figure 5.3(a) it can be seen that the ordering of the hexagonal columnar phase is very well structured at

the extremities of the mesoporous filament, which has been proposed is a result of increased P123 micelle ordering near the AAM channel walls which becomes less ordered further away from the channel walls [30, 31].

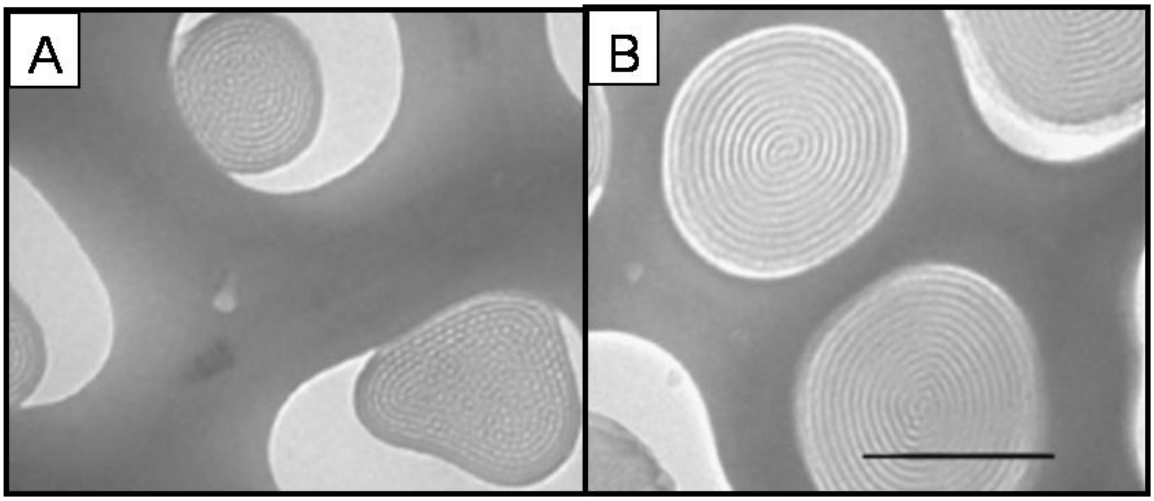


Figure 5.3 Plan view TEM images of mesoporous structures deposited from a gel containing 50% organosilica precursor and 50% silica precursor deposited at (a) 20% and (b) 80% relative humidity. Scale bar corresponds to 100 nm.

A gel used to deposit mesoporous thin films, similar to the one used in this work, can be described as a pseudo liquid crystal which, depending on the rate of evaporation of ethanol and water, and the resulting concentration of the structure directing agent (SDA), determines the structure of the final mesophase formed [26, 32]. The rate of condensation of the mesoporous framework is constant at any given humidity, however when the mesoporous framework is no longer flexible enough to adapt to the changing micelle shape, after prolonged condensation for example, the resulting mesophase is determined [33]. During this study the gel deposition at higher humidity results in the slower evaporation of both ethanol and water, by the diffusion of water

from the surrounding atmosphere into the thin film gel. This has been seen to result in the circular hexagonal ordered mesopores, the circular structure observed in the SAXS pattern in Figure 5.2(a). In a less humid atmosphere ethanol and water evaporate much faster resulting in columnar mesopores, as seen in the SAXS patterns shown in Figures 5.2(b) and 5.2(c).

During the evolution of mesoporous systems the volatile components of the mesoporous sol-gel evaporate over time which leads to a surfactant and silica precursor rich gel [26]. At the same time the acidic component of the gel initiates the condensation of the silica precursor. As both these processes progress the mesoporous network experiences a contraction in the porous structure during synthesis [34]. This contraction is continued if the mesoporous material is further calcined at any temperature [29, 35]. On a thin film the contraction is perpendicular to the surface of the substrate [36, 37] and has been known in some cases to contribute to changes in the pore morphology [38]. This contraction is also experienced by the mesoporous filaments within the AAMs and results in the contact failure between the mesoporous filament and the AAM pore walls. It is postulated that when the mesoporous gel used here dries in a low humidity atmosphere the volatile gel components (ethanol, water and HCl) evaporate at a much faster rate and the PMO network experiences different contraction stresses compared to when it dries in a high humidity atmosphere, where the gel components evaporate more slowly. These different contraction stresses are also thought to be responsible for the different structures produced at different humidity [37].

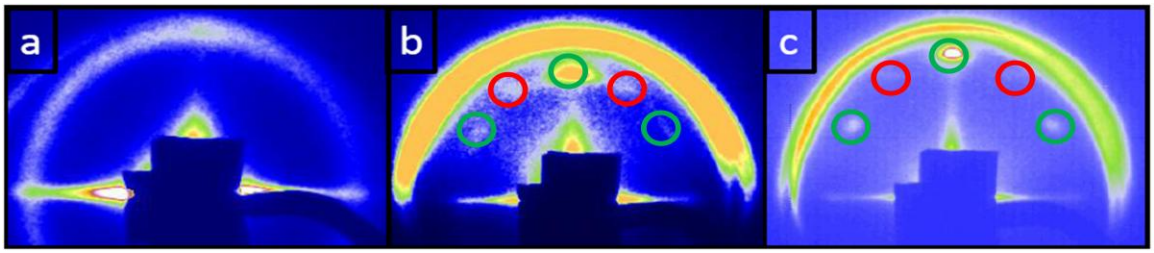


Figure 5.4 SAXS patterns of mesoporous structures deposited at 20% relative humidity from gels containing (a) 50%, (b) 75% and (c) 100% w/w organosilica precursor. The circled regions in Figure 5.4 (b) and (c) are explained in the text.

The drying rate and hence the condensation and disorder-to-order transition process is also thought to be influenced by the amount of organosilica precursor in the deposition gel. Figure 5.4 shows how the SAXS patterns of the composite membranes change when the amount of organic component is changed in the deposition gel. There is a definite change in the mesoporous structure as the organosilica component of the gel is increased from (a) 50% to (b) 75% and (c) 100% at a constant humidity of 20%. This change in mesophase from a columnar to circular pore structure can be attributed to the increase of the organic component and is thought to be due to the organosilica precursor influencing and changing the normal surfactant-TEOS interactions (see Figure 5.4(c)). There is also a slight increase in the d-spacing of 20 Å when the amount of organosilica precursor in the gel is increased from 50% to 100%.

Figures 5.4(b) and 5.4(c) also shows scattering from the surface film of the AAM-silica composite. The intense green circled scattering spots are thought to originate from a 2 D hexagonal mesoporous film on the surface of the AAMs and the red scattering spots originate from the circular pore structure of mesoporous-AAM filaments. These green circled spots can

be indexed as 2 dimensional hexagonal (01), (10) and (01) from left to right and as can be seen to occur at different positions from the mesoporous structures within the AAM channels, circled in red. This surface film hinders the deposition of the gel within the channels of the AAMs resulting in a film which blocks the mass transfer of gel into the channels of the AAMs. The presence of this surface film is further verified by time resolved SAXS measurements discussed below. The intense scatting arc at larger q-values (larger distance from the beam centre) is thought to result from an unordered material also present on the surface of the silica-AAM composite.

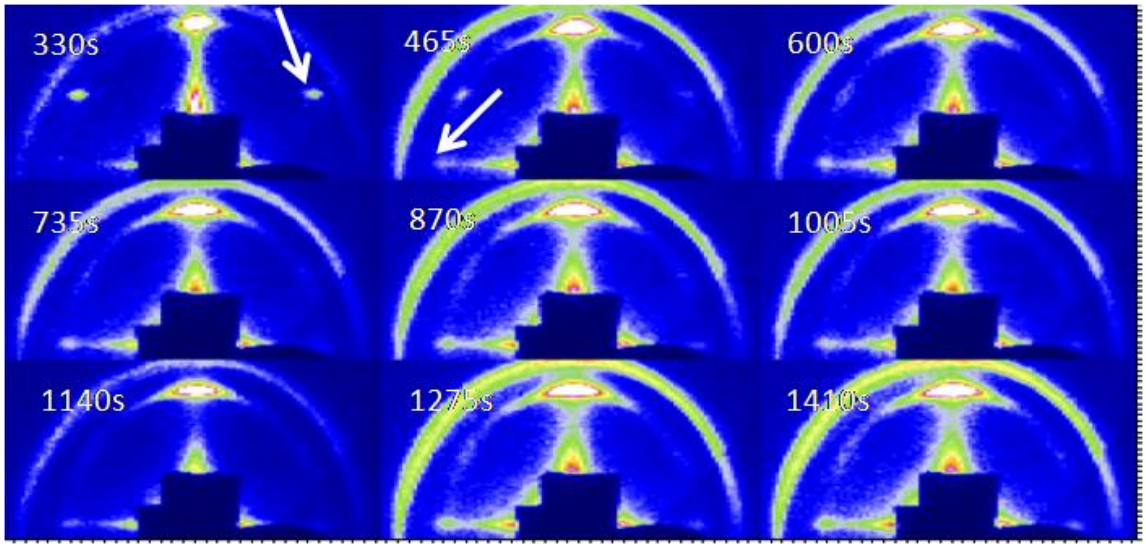


Figure 5.5 Time resolved SAXS patterns of mesoporous structure deposited from a gel containing 50% organosilica precursor at a relative humidity of 20%. The gel was dropped onto the surface of the membrane, positioned in a humidity chamber and the relative humidity was set to 20%. The measurements started 5 min after the sol gel was introduced on the membrane surface.

The number of different mesoporous structures observed at varying deposition conditions and reaction mixtures stimulated a study to be undertaken of the evolution process occurring during the formation of mesoporous structures within AAMs channels. Figures 5.5 show time-resolved SAXS measurements conducted on a 50% w/w organosilica gel deposited at 20% relative humidity. Scattering patterns from the organosilica gel deposited at 20% relative humidity emerges after approximately 120 s (see Figure 5.6 for a more detailed image), with the formation of a (0-1) reflection (due to the columnar structure) at a d-spacing of 116 Å (Figure 5.5 and 5.6). The position of this reflection remains constant until approximately 600 s, at which point the columnar structure experiences a slight contraction. The intensity of the (0-1) reflection remains constant from the initial emergence of structure until the end of the experiment.

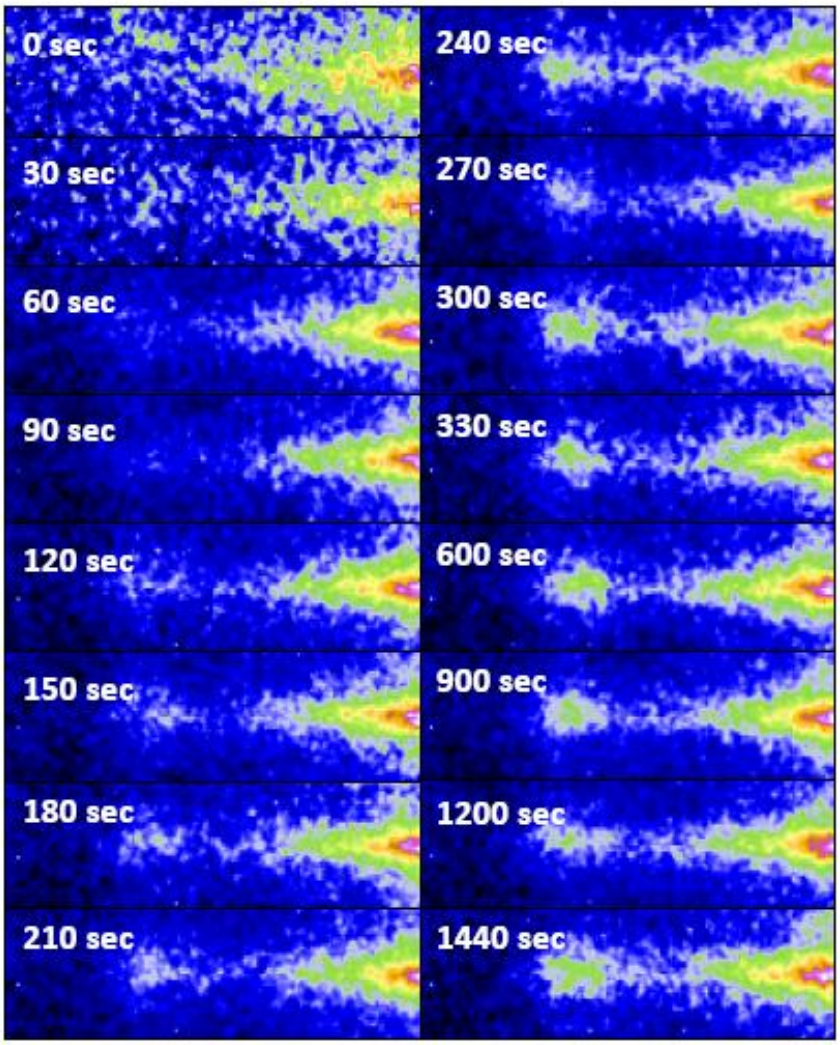


Figure 5.6 Time resolved SAXS measurement of a 50:50 organic/inorganic PMO material, left to dry in ambient conditions. Relative humidity was 20%.

The evolution of structure of the PMO-AAM composite was also studied with respect to time when the drying was induced by rapid application of vacuum, see Figure 5.7 and 5.8. Scattering patterns from the organosilica gel deposited under vacuum emerges approximately 20 s after the vacuum is applied (shown in Figure 5.8). Throughout the duration of the experiment the d-spacing of the (0-1) reflection (again due to the columnar hexagonal structure) remains constant

at 86 Å, with only a drift of 1 or 2 Å during the course of the experiment. The intensity of the (0-1) reflection also remains constant throughout the experiment. The variation in d-spacings seen between the reduced humidity and vacuum experiments is thought to be due to the more complete drying achieved using vacuum, and therefore more contraction of the framework experienced by the vacuum dried sample.

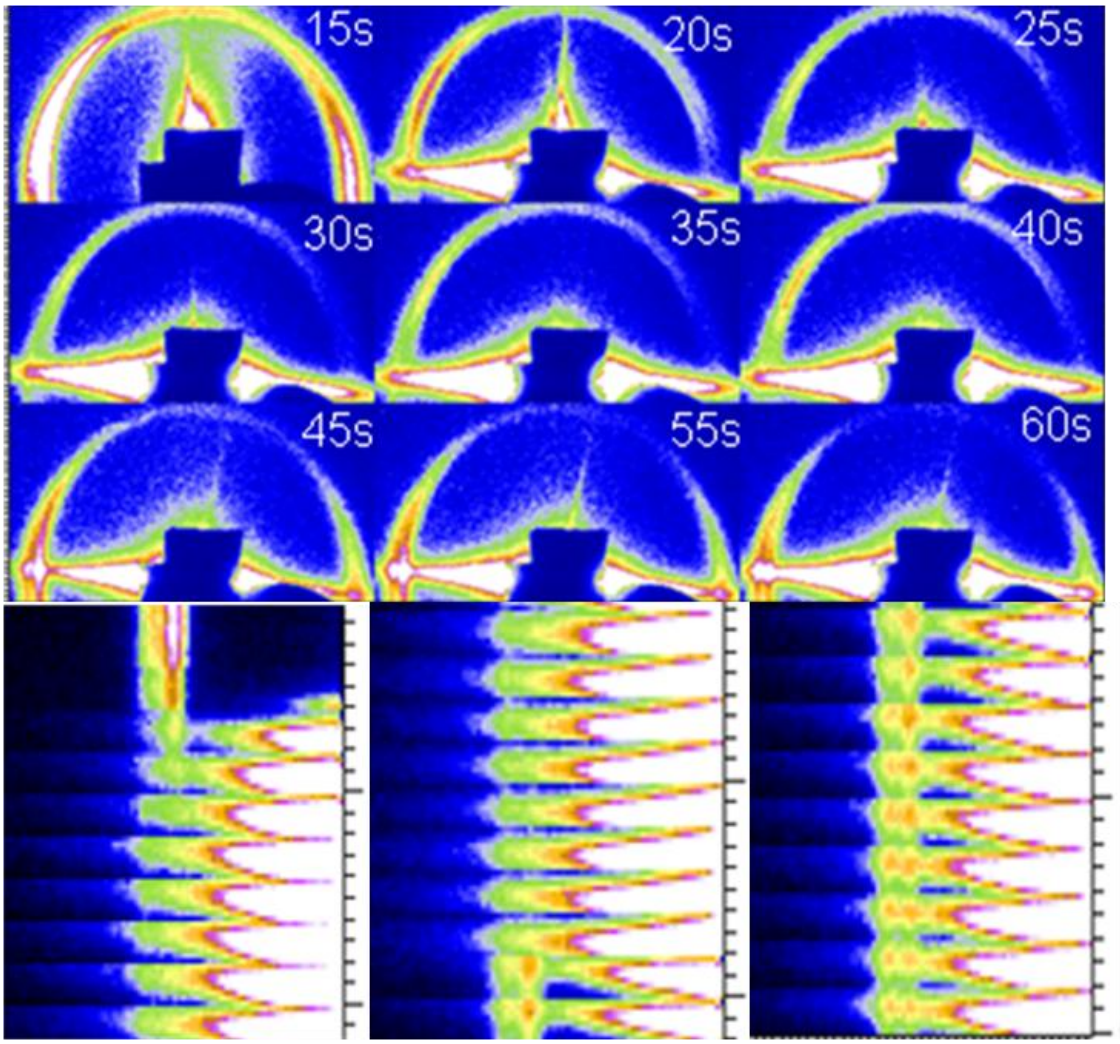


Figure 5.7 Time resolved SAXS patterns of mesophase structures deposited from a gel containing 50% organosilica precursor under vacuum. The sol gel was drop casted on the surface of the membrane, positioned in a vacuum chamber and the vacuum was introduced 10 s after the start of the measurement.

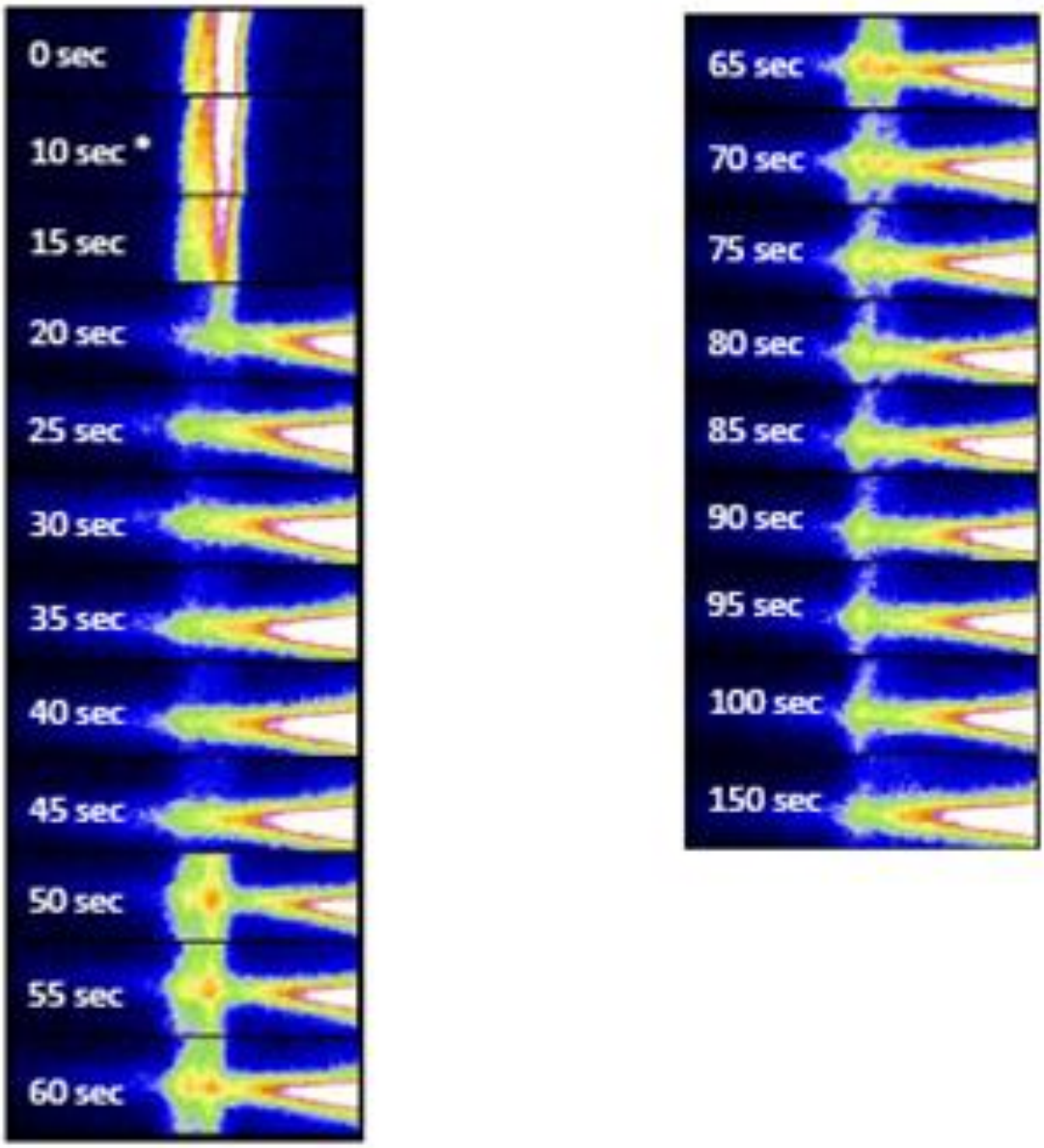


Figure 5.8 Time resolved SAXS measurement of a 50:50 organic/inorganic PMO material. To induce rapid drying a vacuum was used which was applied at frame 10 which was 10 s from the beginning of the measurement. Relative humidity was 20%.

As expected the rate of evolution of the mesoporous structure is dependent on the rate of solvent evaporation, *i.e.* under vacuum the evaporation of the volatile components proceeds almost instantaneously, seemingly the first stage of ordering appears at approximately 20 s (Figure 5.8). However, it takes more than 2 min for the structure to evolve when the gel is left to dry in reduced humidity conditions (Figure 5.6), Brinker *et al.* reported a greater ethanol content in the thin film gel leads to longer drying times [39]. In both cases, in the early stages of the deposition process, isotropic scattering from the surface 2 dimensional hexagonal over-layer is present before the disorder-to-order transition is detected. The isotropic ring suggests that the deposition gel solution contains micelles of similar sizes but lacks order in both direction and orientation. Generally, in both cases the expected columnar structure is obtained, however careful examination of the scattering pattern sequences show that the mesoporous structures are evolving differently as time progresses (see the bottom half of Figure 5.7). For example after approximately 300 s for the sample in Figure 5.5, the mesoporous ordering is observed on the membrane surface (indicated by the arrow in the 330 s frame) due to the accelerated evaporation of ethanol from the surface over-layer gel. The columnar mesoporous structure within the AAM channels starts to appear at approximately 460 s (indicated by the arrow in the 465 s frame) while scattering from the ordered region of the mesophase surface starts to disappear. After 600 s the structure of the mesoporous filaments remains constant with a slight contraction due to continued drying and condensation of the mesoporous framework. Evolution of the mesoporous structure under vacuum (Figure 5.7 and 5.8) shows the diffuse scattering ring has the same d-spacing as the ordered columnar structure observed within the AAM channels. The transformation from diffuse scattering to ordered structure within the AAM is very fast, occurring at about 50 s after the start of the deposition. Interestingly, an additional scattering

spot at a higher "*q*" higher (scattering angle) appears in the in-plane direction at approximately 45 s and stays intact until the end of the experiment and maybe attributed to the appearance of a lamellar phase along with the columnar hexagonal phase already thought to be present in the AAM channels. Hence the fast drying rate induces the quick concentration of non-volatile gel components (silica and organosilica precursors and non-ionic surfactant [27, 40]) which causes formation of the columnar hexagonal phase.

The structures obtained under accelerated drying rates are remarkably different than the structures obtained at the reduced humidity conditions, where normally a single phase material is obtained by slowly reaching the disorder-to-order transition.

5.5 Conclusions

It has been shown that mesoporous silica filaments with a PMO component can be obtained within the channels of AAMs. Additionally, we illustrate the resulting mesoporous structures within the pores of the AAM when the deposition environment is controlled. Depending on the rate of evaporation of the volatile components of the deposition gel and the contraction stresses experienced by the condensing mesostructure, different mesoporous arrangements can be formed. Time resolved measurements showed the evolution of different structures as the silica-AAM composite membranes developed in reduced humidity conditions and under accelerated vacuum drying. This work highlights the importance of the environment on the synthesis of mesoporous materials and the control needed to produce the desired material morphology.

5.6 References

1 Hanrahan, J. P.; Donovan, A.; Morris, M. A.; Holmes, J. D., *J. Mater. Chem.* **2007,** *17*, 3881.
2 Rice, R. L.; Kidd, P.; Holmes, J. D.; Morris, M. A., *Journal of Materials Chemistry* **2005,** *15*, 4032-4040.
3 Wang, J. F.; Tsung, C. K.; Hayward, R. C.; Wu, Y. Y.; Stucky, G. D., *Angew. Chem. Int. Ed.* **2005,** *44*, 332.
4 Marlow, F.; Zhao, D. Y.; Stucky, G. D., *Microporous Mesoporous Mater.* **2000,** *39*, 37.
5 Arnold, D. C.; O'Callaghan, J. M.; Sexton, A.; Tobin, J. M.; Amenitsch, H.; Holmes, J. D.; Morris, M. A., *Appl. Surf. Sci.* **2009,** *255*, 9333.
6 Wu, Y.; Cheng, G.; Katsov, K.; Sides, S. W.; Wang, J.; Tnag, J.; Fredrickson, G. H.; Moskovits, M.; Stucky, G. D., *Nature* **2004,** *3*, 816.
7 Yao, B.; Fleming, D.; Morris, M. A.; Lawrence, S. E., *Chem. Mater.* **2004,** *16*, 4851.
8 Yamaguchi, A.; Uejo, F.; Yoda, T.; Uchida, T.; Tanamura, Y.; Yamashita, T.; Teramae, N., *Nat. Mater.* **2004,** *3*, 337.
9 Ku, A. Y.; Taylor, S. T.; Heward, W. J.; Denault, L.; Loureiro, S. M., *Microporous Mesoporous Mater.* **2006,** *88*, 214.
10 Masuda, H.; Fukuda, K., *Science* **1995,** *268*, 1466.
11 Melde, B. J.; Holland, B. T.; Blanford, C. F.; Stein, A., *Chem. Mater.* **1999,** *11*, 3302.
12 Inagaki, S.; Guan, S.; Fukushima, Y.; Ohsuna, T.; Terasaki, O., *J. Am. Chem. Soc.* **1999,** *121*, 9611.
13 Hatton, B.; Landskron, K.; Whitnall, W.; Perovic, D.; Ozin, G. A., *Accounts of Chemical Research* **2005,** *38*, 305.
14 Yang, Q. H.; Liu, J.; Zhang, L.; Li, C., *J. Mater. Chem.* **2009,** *19*, 1945.
15 Shylesh, S.; Samuel, P. P.; Sisodiya, S.; Singh, A. P., *Catal. Surv. Asia.* **2008,** *12*, 266.
16 Hoffmann, F.; Cornelius, M.; Morell, J.; Froba, M., *J. Nanosci. Nanotechnol.* **2006,** *6*, 265.
17 Petkov, N.; Stock, N.; Bein, T., *J. Phys. Chem. B* **2005,** *109*, 10737.
18 Platschek, B.; Petkov, N.; Bein, T., *Angew. Chem. Int. Ed.* **2006,** *45*, 1134.
19 Grosso, D.; Babonneau, F.; Albouy, P. A.; Amenitsch, H.; Balkenende, A. R.; Brunet-Bruneau, A.; Rivory, J., *Chem. Mater.* **2002,** *14*, 931.
20 Grosso, D.; Babonneau, F.; Sanchez, C.; Soler-Illia, G. J. D. A.; Crepaldi, E. L.; Albouy, P. A.; Amenitsch, H.; Balkenende, A. R.; Brunet-Bruneau, A., *J. Sol-Gel Sci. Tech.* **2003,** *26*, 561.
21 Cauda, V.; Muhlstein, L.; Onida, B.; Bein, T., *Microporous Mesoporous Mater.* **2009,** *118*, 435.
22 Cauda, V.; Onida, B.; Platschek, B.; Muhlstein, L.; Bein, T., *J. Mater. Chem.* **2008,** *18*, 5888.
23 Platschek, B.; Kohn, R.; Doblinger, M.; Bein, T., *Langmuir* **2008,** *24*, 5018.
24 Wang, D. H.; Kou, R.; Yang, Z. L.; He, J. B.; Yang, Z. Z.; Lu, Y. F., *Chem. Comm.* **2005**, 166.
25 Grosso, D.; Babonneau, F.; Albouy, P. A.; Amenitsch, H.; Balkenende, A. R.; Brunet-Bruneau, A.; Rivory, J., *Chemistry of Materials* **2002,** *14*, 931-939.

26 Innocenzi, P.; Malfatti, L.; Costacurta, S.; Kidchob, T.; Piccinini, M.; Marcelli, A., *J. Phys. Chem. A* **2008,** *112*, 6512.
27 Brinker, C. J.; Lu, Y. F.; Sellinger, A.; Fan, H. Y., *Adv. Mater.* **1999,** *11*, 579.
28 Innocenzi, P.; Costacurta, S.; Kidchob, T.; Malfatti, L.; Falcaro, P.; Soler-Illia, G., *Sol-Gel Methods for Materials Processing* **2008**, 105.
29 Grosso, D.; Balkenende, A. R.; Albouy, P. A.; Ayral, A.; Amenitsch, H.; Babonneau, F., *Chem. Mater.* **2001,** *13*, 1848.
30 Lai, P.; Hu, M. Z.; Shi, D.; Blom, D., *Chem. Comm.* **2008**, 1338.
31 Kellogg, G. J.; Walton, D. G.; Mayes, A. M.; Lambooy, P.; Russell, T. P.; Gallagher, P. D.; Satija, S. K., *Phys. Rev. Lett.* **1996,** *76*, 2503.
32 Cagnol, F.; Grosso, D.; Soler-Illia, G. J. D. A. S.; Crepaldi, E. L.; Babonneau, F.; Amenitsch, H.; Sanchez, C., *J. Mater. Chem.* **2003,** *13*, 61.
33 Innocenzi, P.; Malfatti, L.; Kidchob, T.; Falcaro, P.; Guidi, M. C.; Piccinini, M.; Marcelli, A., *Chem. Comm.* **2005**, 2384.
34 Baute, D.; Frydman, V.; Zimmermann, H.; Kababya, S.; Goldfarb, D., *J. Phys. Chem. B* **2005,** *109*, 7807.
35 Tanaka, S.; Tate, M. P.; Nishiyama, N.; Ueyama, K.; Hillhouse, H. W., *Chem. Mater.* **2006,** *18*, 5461.
36 Tate, M. P.; Eggiman, B. W.; Kowalski, J. D.; Hillhouse, H. W., *Langmuir* **2005,** *21*, 10112.
37 Williford, R. E.; Addleman, R. S.; Li, X. S.; Zemanian, T. S.; Birnbaum, J. C.; Fryxell, G. E., *J. Non-Cryst. Solids* **2005,** *351*, 2217.
38 Crepaldi, E. L.; Soler-Illia, G. J. D. A.; Grosso, D.; Cagnol, F.; Ribot, F.; Sanchez, C., *J. Am. Chem. Soc.* **2003,** *125*, 9770.
39 Brinker, C. J.; Frye, G. C.; Hurd, A. J.; Ashley, C. S., *Thin Solid Films* **1991,** *201*, 97.
40 Huang, M. H.; Dunn, B. S.; Zink, J. I., *J. Am. Chem. Soc.* **2000,** *122*, 3739.

Chapter 6

Chemical Modification of Silica Surfaces and their use in the Production of Metallic Nanostructures

6.1 Abstract

Thiol-functionalised periodic mesoporous organosilicas (PMOs) were investigated as templates for the production of germanium nanostructures. The increased hydrophobicitiy of the ethylene-bridged mesoporous silica framework and their reasonable thermal stability makes them potentially suitable templates for the growth of Ge nanostructures. The thiol groups on the surface of the PMO pore walls were used as anchors for gold nanoparticles that acted as seeds for the growth of germanium nanostructures, via a supercritical fluid deposition process. The method developed for functionalising the surface of the PMOs with thiol groups was also applied to the surface of masked silicon wafers. The block co-polymer polystyrene-polymethyl methacrylate (PS-PMMA) mask was spin-coated onto the surface of a silicon wafer and the PMMA block was removed, exposing areas of the silicon substrate which were functionalised with the thiol ligands. As with the PMO materials, the thiol groups were used to anchor gold nanoparticles to the surface of the exposed silicon substrate which were then subsequently used as seeds for growing germanium nanostructures.

6.2 Introduction

Periodic mesoporous organosilicas (PMOs) are an attractive class of ordered mesoporous materials consisting of hybrid structural units, *i.e.* -[$_{1.5}$OSi-R-SiO$_{1.5}$]- (where R is a bridged group, such as -CH_2CH_2-, -CH=CH-, or a phenyl group), where the inorganic and organic moieties in the structure are covalently linked to each other [1-5]. PMO materials offer novel porous structures with different chemical characteristics to the traditional inorganic-based mesoporous materials. These materials combine the rigidity of the silica framework with the added functionality of the organic counterpart. The organic functionality is generated during the initial synthesis of the material by hydrolysis of an appropriate bridged-organosilica precursor. PMOs have found use in a wide range of applications including chromatography [6] and as high-k dielectrics [7], as reviewed by Wight *et. al.* [8] and Hoffmann *et al.* [9]. PMO materials have much more applications than their completely inorganic analogues due to their increased reactivity and functionality. PMOs or the completely inorganic silica analogue can have further organic functionality added, by reaction of surface silanol groups (present on all silica surfaces) with an organo silane. The variety of possible organic functionality is only limited by the availability of stable organo silane precursors.

The use of germanium in the semiconductor industry has again been investigated in favour of silicon due to better electron and hole mobilities [10]. The ongoing miniaturisation in the microelectronics industry of devices and their components has lead to a significant shift towards the research of nanosized device and components, their synthesis, characterisation and

applications. Germanium nanowires have already been utilised in numerous applications, including high speed FETs [11], chemical sensors [12] and light emitting devices [13]. A successful device will require the incorporation of germanium nanostructures into accessible and usable architectures where the orientation and position of nanowires are readily controlled. Crystalline germanium is near impossible to synthesize using solution based chemistry due to the strong covalent bonding that exists in the crystal and the need for high temperature to encourage crystallisation. Other methods of synthesising crystalline germanium include chemical vapour deposition, which require temperatures of up to 415°C [14] if done without the use of metallic catalyst, such as gold [15] which lowers the reaction temperature to 360°C. The growth of germanium nanowires from gold nanoseeds follows the vapour-liquid-solid (VLS) growth mechanism, first described by Wagner and Ellis [16, 17] in 1964 to explain the growth of silicon whiskers from the gas phase by CVD form a surface containing a gold melt. The mechanism dictates that instead of depositing on the surface, the silicon dissolves in a gold droplet to form an alloy of the two metals. When saturation of silicon within the gold-silicon melt occurs silicon precipitates from the melt in the form of a crystalline whisker. The diameter of the whisker is determined by the size of the droplet from which the whisker grows. The temperature at which one metal becomes soluble in another is called the eutectic temperature. The eutectic temperature of most semiconducting materials is high, for example $T(Au:Si)_{eutectic}$=361°C and $T(Au:Ge)_{eutectic}$=360°C. A schematic of the VLS theory can be seen in Figure 6.1.

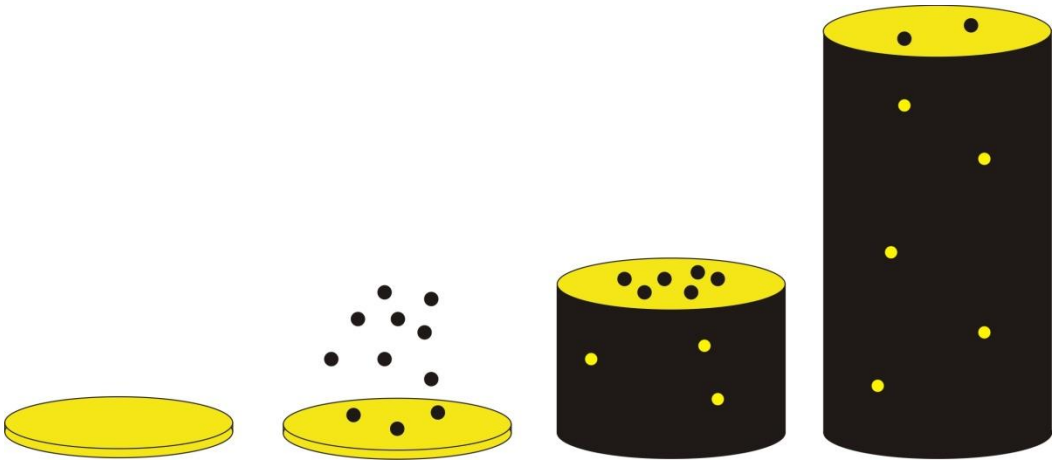


Figure 6.1 A schematic showing the VLS theory starting with a gold seed, followed by germanium inclusion within the gold seed. Next, once saturation of germanium within the gold seed occurs a nano-wire begins to grown. Note that the nanowire also contains traces of gold and the gold seed contains traces of germanium.

Since the eutectic temperatures are obviously above the boiling points of conventional solvents the use of supercritical fluids has been employed in the production of silicon wires [18, 19] and nanocrystals [20, 21] and germanium nanowires [22, 23]. The supercritical fluid process provides the appropriate solvation needed for the ligand stabilised gold nanoparticles and the germanium organo-metallic precursor. This high temperature and high pressure method used to produce crystalline germanium relies on the thermal degradation of an organo-metallic precursor in the presence of a gold nanoparticle catalyst.

Patterns created from self assembling block copolymers present a method to produce nanoscale patterns developed solely by the lithographic capability of the block copolymer. If the desired

control over the orientation and long range order can be achieved lithographic patterns can be cheaply produced. Block copolymer thin films have a limited number of device applications with only speciality polymers having applications in fields such as conducting devices. Current lithography methods used in the microelectronics industry are fast reaching the limits of achieving the required resolution for the next generation of devices. Alternative methods which achieve the desired architecture of the next and future generation devices and limiting the cost of tooling and processing will be an important breakthrough in lithographic methods. Polymer templates can produce the required feature sizes and with the correct processing, long range order [24]. Block copolymers spontaneously organise into arrays of nanostructures which include cylindrical and lamellar domains [24, 25].

Polymer templating requires a polymer with two chemically different blocks that can phase separate and self assemble into an ordered array on a substrate surface. One block can then be removed by a suitable etching process to expose areas of the underlying substrate. Once the desired material has been deposited the remaining polymer block may be removed leaving the patterned material behind.

6.3 Experimental

Ethylene bridged PMO was synthesised, chemically functionalised, embedded with Au nanoparticles and used as templates for the growth of germanium nanowires, the procedure of which is detailed in Chapter 2. Ethylene bridged PMO was synthesised following the method proposed by Guo *et al.* [26] after which the surfactant was removed by repeated washing in a dilute HCl/ethanol solution. The PMO surface was chemically functionalised with thiol groups by refluxing the PMO powder in dry toluene with a suitable thiol-silane precursor. The thiol-functionalised PMO material was suspended in an aqueous chloroauric acid solution where the basic thiol groups act as reaction centres, which reduce the chloroauric acid, resulting in the deposition of metallic gold clusters on the surface and in the pores of the PMO material producing the PMO-Au composite material. The deposition of germanium metal within the pore structure of the Au-PMO was carried out in a 1 mL high pressure cell with hexane and the germanium precursor, di-phenyl germane. The reaction was carried out at 360°C after which the black material, Ge-Au-PMO was collected.

The polymer templates, which consisted of empty vertical pores in a PS matrix, were kindly donated by Prof Michael Morris at UCC. The production of the PMMA etched PS-PMMA thin films have been reported in Xiao *et al.* [27] and described in detail in Chapter 2. A PS-PMMA was then deposited onto a silicon substrate and annealed under vacuum which induces phase separation between the PS and PMMA. The PMMA phase was removed by decomposing the cylindrical PMMA cylinders with deep UV exposure, followed by washing with acetic acid and

deionised water. This etching step is thought to etch the wetting layer that exists below the PS-PMMA layer and the entire PMMA block. This process leaves pores of approximately 50 nm in diameter, 25 nm deep (approx) with a spacing of 25 nm (approx) between pores. The PS templates were refluxed with same thiol-silane as was used for the PMO functionalisation reaction. This step functionalised the exposed areas of silicon wafer not covered by the PS matrix. Thiol-stabilised gold nanoparticles were synthesised following the procedure outlined in Hostetler *et al.* [28]. The synthesis method is described in full in Chapter 2. The thiol functionalised PS template films were suspended in a thiol suspension of thiol stabilised Au nanoparticles. The thiol groups on the exposed silicon of the polymer film are thought to exchange with the thiol groups stabilising the Au nanoparticles and results in the deposition of clusters of Au nanoparticles within the vertical pores of the polymer template. The deposition of germanium metal within the pore structure of the PS template was carried out in a similar fashion to that described above for the PMO material, but a larger reaction cell was used to accommodate the polymer substrates. The PS template with the embedded Au nanoparticles was placed in a 25 mL high pressure cell, along with hexane and the germanium precursor. The cell was placed in a tube furnace and pressurised with CO_2 to 27.5 MPa held at 360°C for approximately 1 h to degrade the germanium precursor before the cell was allowed to cool to ambient conditions and substrates recovered.

6.4 Results and Discussion

6.4.1 Periodic Mesoporous Organosilicas used in Production of Nanostructures

The successful synthesis of ethylene bridged periodic mesoporous organosilica (PMO-Et) was quantified by low angle x-ray diffraction (XRD) and N_2 adsorption experiments. The PMO-Et material synthesised possessed well ordered hexagonal pore structure, as determined from the narrow diffraction peak of the (100) plane in the low angle XRD data (d-spacing at 106 Å), and a narrow pore size distribution with a mean pore diameter of 68 Å as obtained from the Barret-Joyner-Halenda (BJH) calculations of the N_2 adsorption isotherms, the distribution is shown in Figure 6.2(b). The long range ordering of the pore structure is a familiar characteristic of PMO materials[29]. The shift of the (100) peak from a d-spacing of 106 Å to a d-spacing 100 Å (upon application of Braggs Law, see Chapter 2) as shown in Figure 6.2(a) demonstrates the successful removal of the P123 surfactant from the template after the successive washings of the PMO-Et material in a dilute HCl/ethanol solution. The porous structure of the PMO material can be clearly seen in the transmission electron microscopy (TEM) image also shown in Figure 6.2(c).

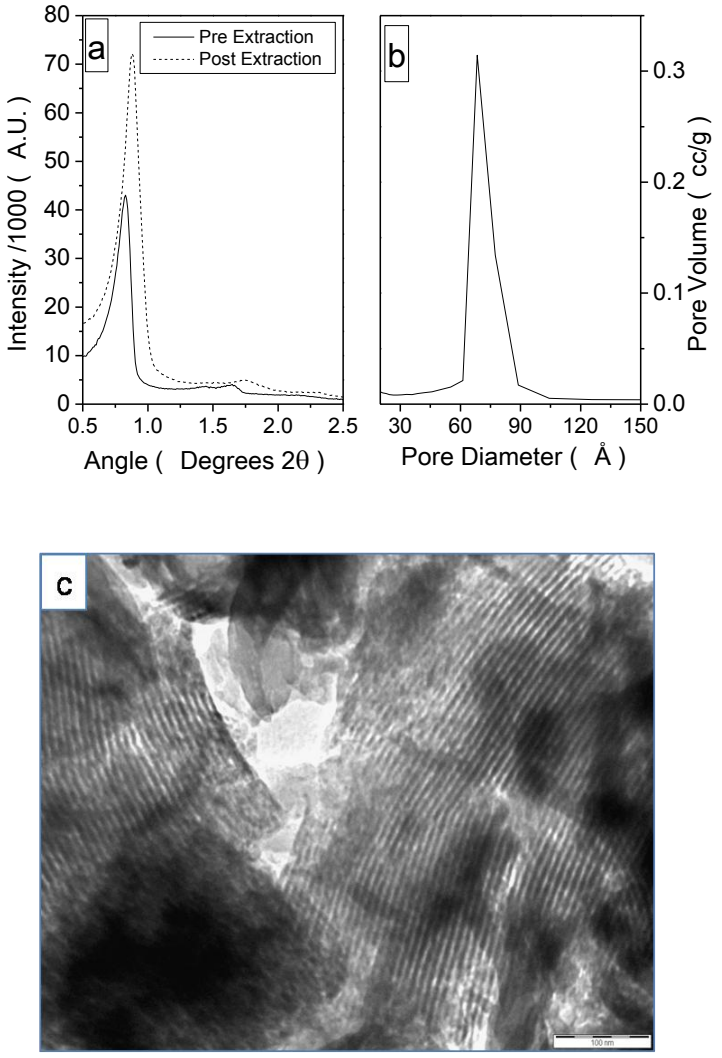


Figure 6.2 (a) Low angle XRD patterns of the as-synthesised PMO-Et material before and after surfactant extracted. (b) The BJH pore size distribution from the nitrogen adsorption isotherm of the same material with a pore sizes of 68 Å, a pore volume of 0.85 cm^3 g^{-1} and a BET surface area of 758 m^2 g^{-1} and (c) shows a TEM image of the porous structure of the PMO material, the scale bar reads 100 nm.

As discussed Chapter 2 it is possible to functionalise the surface of PMO materials, such as the PMO-Et material synthesised here, due to the presence of surface silanol (Si-OH) groups which

act as mildly acidic sites that can react with silane precursors, thereby chemically bonding various functional groups to the silica surface [30]. The bonded functional groups depend on the silane precursor used, here a thiol silane was used which bonds a propyl-thiol group to the surface of the silica. The surface density of silanol groups on a silica surface has been reported by Okron-Schmidt [31] to be between 2-12 hydroxyl groups per nm^2, the average being 5 hydroxyl groups per nm^2. The surface density of silanol groups can be increased by hydrolysing any silica surface with methoxy or ethoxy groups using a KOH solution [32], or oxygen plasma treatment [33].

The thiol functionalisation of the PMO-Et material was carried out in dry toluene and under nitrogen reflux conditions. The thiol silane precursor was added to a refluxing suspension of the PMO material in dry toluene while minimising its exposure to air and moisture. Prolonged exposure to air and moisture would initiate the condensation and polymerisation of the silane [34]. Carrying out the reaction carefully ensures that unwanted condensation and polymerisation of the precursor thiol silane is kept to a minimum and only a small covering of propylthiol on the surface of the ethylene bridged PMO material is achieved [35].

Low angle XRD patterns of the thiol functionalised PMO material shows the retention of a well-organized mesoporous material (there is no change in the d-spacing of the (100) peak) with long range pore ordering, see Figure 6.3(a) and mean pore size of 61 Å, see Figure 6.3(b).

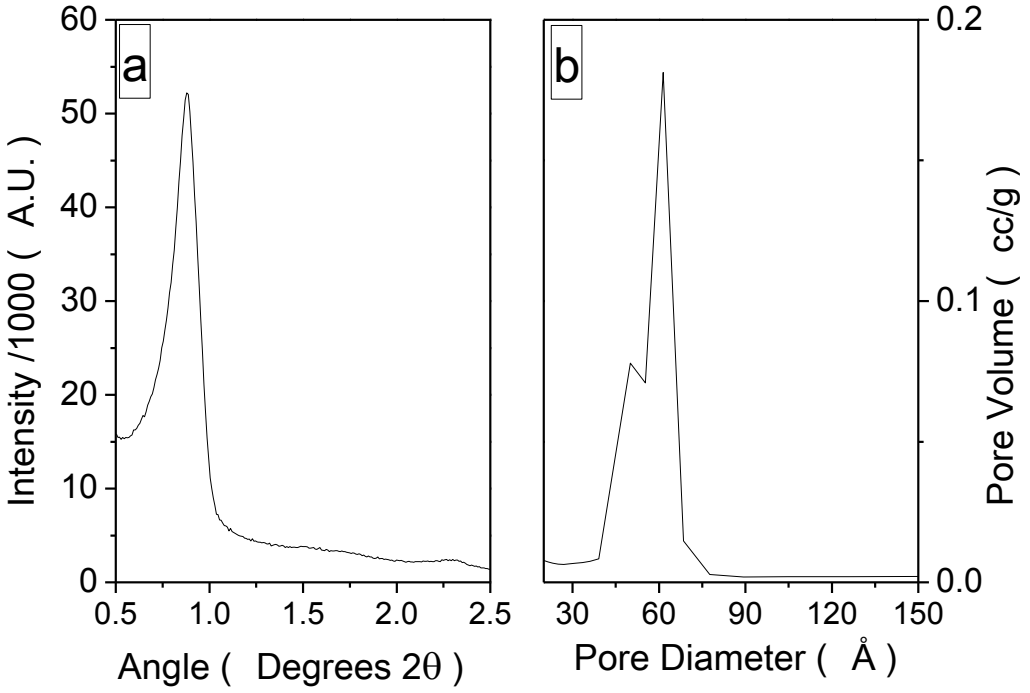


Figure 6.3 (a) Low angle XRD of the thiol functionalised PMO material and (b) pore size distribution of the same material showing a mean pore size of 61 Å, pore volume of 0.5487 cm^3 g^{-1} and a BET surface area of 498 m^2 g^{-1}.

Nitrogen adsorption measurements of the thiol-functionalised PMO samples showed a decrease in pore diameter, pore volume and BET surface area from 68 Å, 0.85 cm^3 g^{-1} and 758 m^2 g^{-1} respectively as shown in Figure 6.2(b) compared to 61 Å, 0.54 cm^3 g^{-1} and 498 m^2 g^{-1} of the non-functionalised PMO sample shown in Figure 6.3(b). The decrease in the pore diameter, pore volume and BET surface area indicates a surface covering of the thiol functionality reducing the pore diameter and pore volume and increasing particle size which reduces the total surface area. Previous solid state NMR work on similar thiol functionalised PMO materials has shown the

attachment of the propyl thiol group to the surface to PMO material [36] via a reaction with the surface silanol groups. The reaction between the surface silanol groups and the thiol siliane precursor is seen as a reduction in the concentration of surface silanol groups and the appearance of the propylthiol group.

The method for the inclusion of Au nanoparticles into the pores of the thiol-functionalised PMO material is described in detail in Chapter 2. The basic thiol groups attached to the surface of the silica surface react with the chloroauric acid in a neutralisation reaction which deposits metallic gold on the surface and within the porous framework of the PMO. Figure 6.4(a) shows an XRD of the PMO material with incorporated Au nanoparticles. The Au incorporated PMO sample showed broad, low intensity XRD peaks at 38.2° 2θ and 44.4° 2θ, representative of gold (111) and (200) peaks respectively. The broad low intensity XRD peaks are characteristic of nanoparticles. Figure 6.4(b) shows BJH data from the PMO material with incorporated Au nanoparticles. From the BJH and N_2 adsorption data for this material a further reduction in the pore diameter, pore volume and BET surface area to 58.9 Å, 0.40 cm^3 g^{-1} and 250 m^2 g^{-1}. The further reduction in the pore diameter and especially pore volume of the PMO material upon incorporation of Au nanoparticles in the PMO material indicates the successful deposition of Au nanoparticles within the porous network of the PMO material.

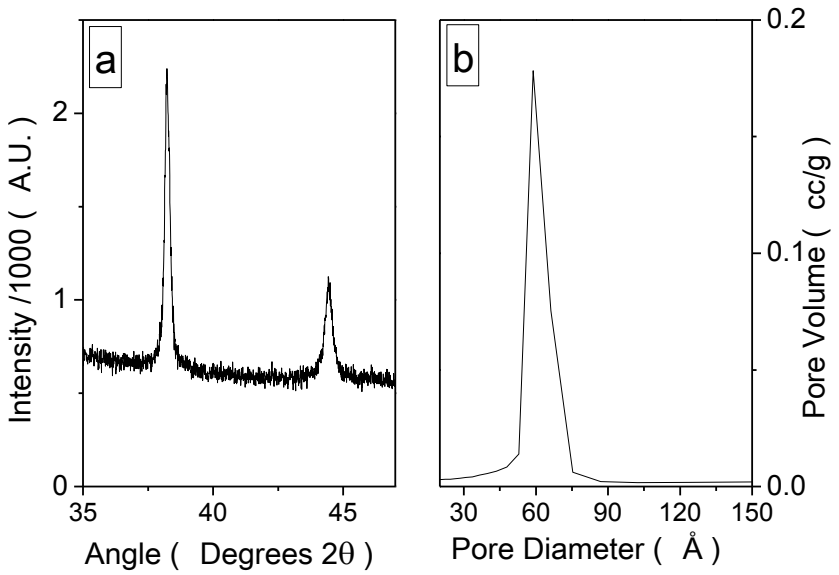


Figure 6.4 (a) XRD pattern of the PMO material with incorporated Au nanoparticles, showing the characteristic (111) diffraction peak and the (200) diffraction peak of gold and (b) BJH data of the same sample showing the continued reduction in pore diameter upon incorporation of Au nanoparticles.

Successful deposition of gold nanoparticles within and on the surface of the PMO material was also confirmed by TEM, as shown in Figure 6.5. Also shown in Figure 6.5 is the EDX spectrum of the same material, from which the labelled peaks due to gold can be seen.

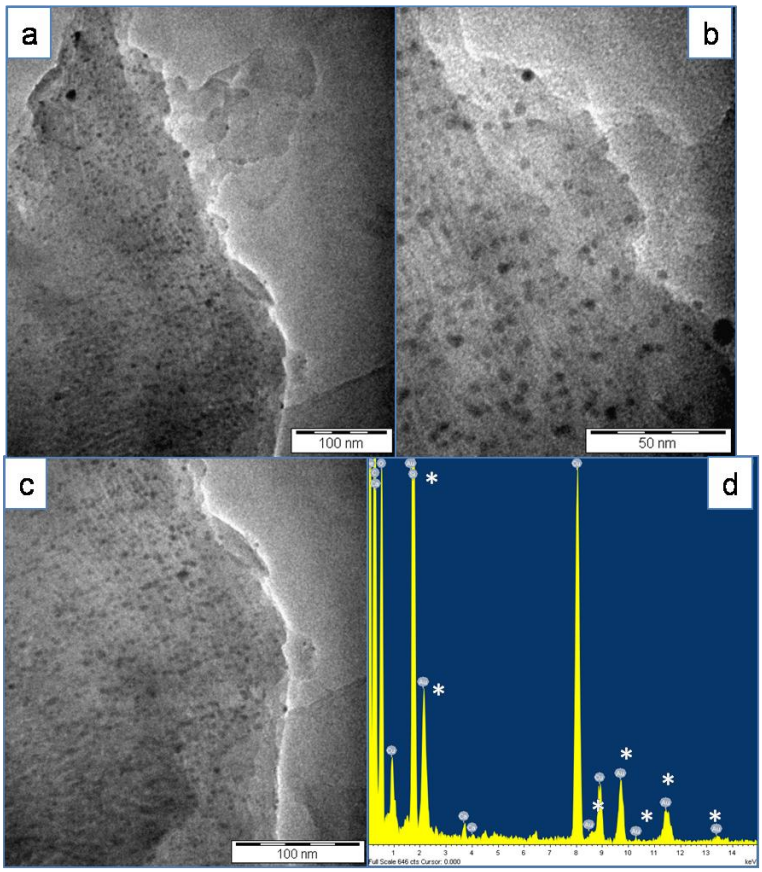


Figure 6.5 (a)-(c) TEM images of a PMO material with incorporated Au nanoparticles of various sizes deposited on the surface and in the pores of a PMO material. Also shown in (d) is the EDX spectrum of the same material with the Au peaks labelled.

Germanium inclusion into the pores of the PMO-Au material was carried at Ge precursor concentrations of 10 μL per 100 mg of the PMO-Au material. The reaction was undertaken in a pressurised hexane environment at 360°C. The recovered black material is referred to as PMO-Au-Ge. The mechanism of nanowire growth from a seed crystal is based on the

vapour/liquid/solid (VLS) growth mechanism which was developed by Wager *et al.* in the 1960s [16, 17]. Applying the VLS theory to the system here it is proposed that the germanium precursor degrades to atomic Ge and dissolves in the melted liquid phase of the catalyst, in this case Au. This occurs above the eutectic temperature of Ge:Au, see Figure 6.6.

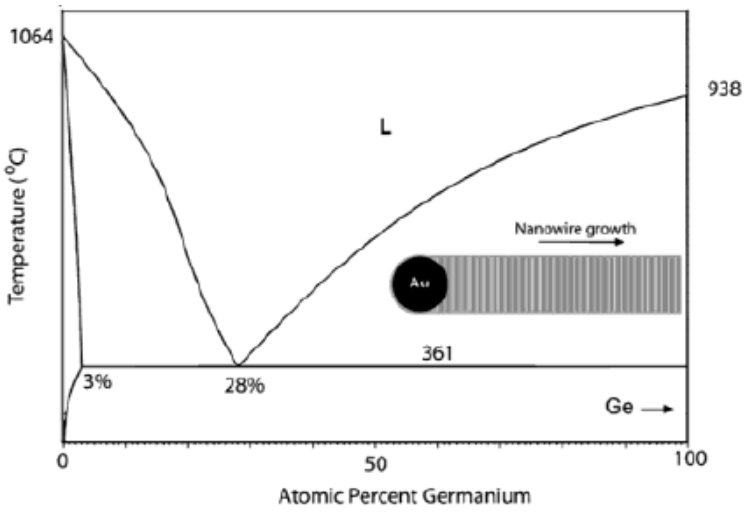


Figure 6.6 Binary phase diagram for the Au:Ge system re-produced from Hanrath *et al.* [23].

Once the gold droplet is saturated with atomic Ge, a germanium whisker exits the liquid droplet mixture. Growth is maintained by the continued incorporation of atomic Ge into the liquid phase droplet of the gold catalyst, this ensures that saturation is continuously maintained until the supply of atomic Ge is exhausted. As a result of this growth mechanism the limiting diameter of the whisker/wire is determined by the size of the liquid metal/catalyst droplet [23]. The pressurised hexane and sc-CO_2 atmosphere in which the nanowires are produced is an excellent medium for solvating the Ge precursor and penetrating into the pore structure of the PMO material to access the Au seeds within the pore structure.

Shown in Figure 6.7(a) to (c) are the different sizes of Ge nanowires obtained from the PMO-Au-Ge material. The varying sizes of nanowires are due to the different sizes of gold nanoparticles from which they grew. The large size distribution of nanoparticles resulted from the nature of the deposition method of the gold nanoparticles within the pore network and on the surface of the material. Due to the growth mechanism of these nanowires (catalysed growth from a seed crystal), these nanowires are thought to be near completely crystalline, rather than a collection of polycrystalline particles. The large amount of particulate matter which is also present in the TEM images may be due to poor control over the reaction conditions, for example, the reaction may have been too long or conducted at an incorrect temperature.

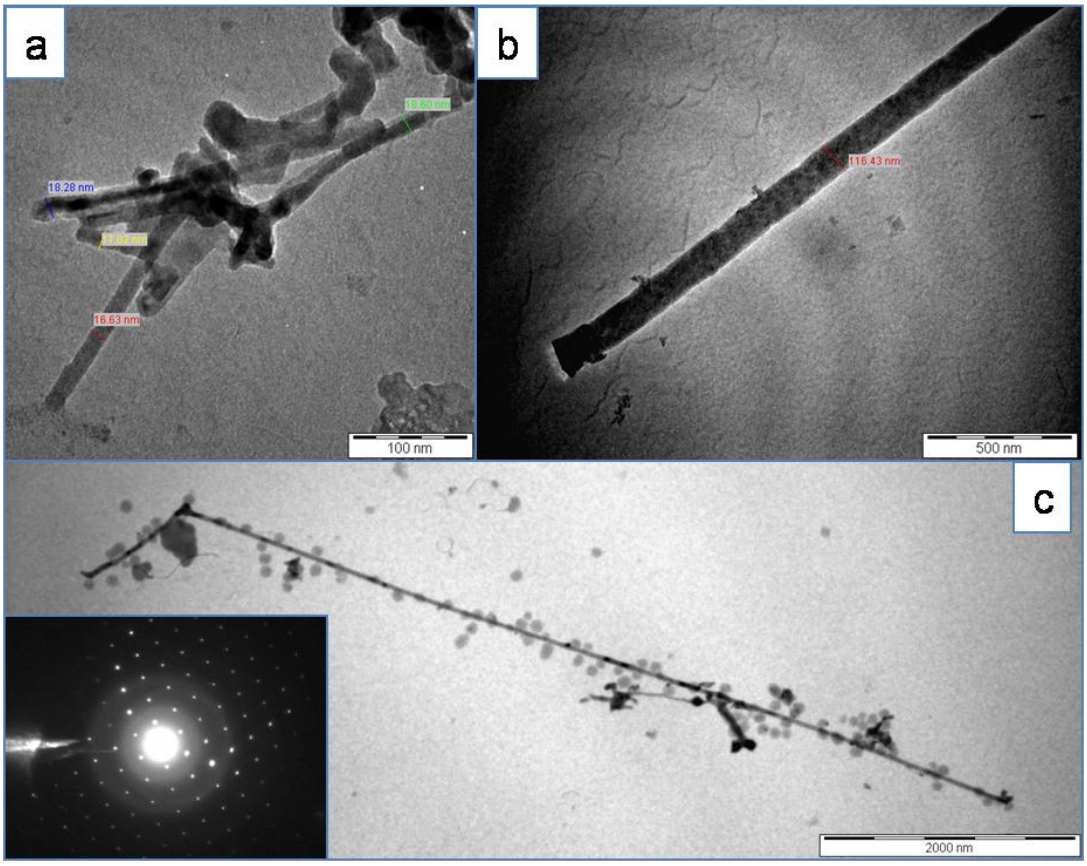


Figure 6.7 (a) and (b) TEM micrographs showing the recovered nanowires from the PMO-Au-Ge material. Figure (c) shows a TEM image and election diffraction pattern of one of the larger and highly crystalline nanowires synthesised using the PMO-Au material.

X-ray diffraction (XRD) data indicates the crystalline nature of the material recovered from Ge experiments and is shown in Figure 6.8. The XRD data was indexed using a JCPDS (Joint Committee on Powder Diffraction Standards) data base of common materials. A feature of the XRD pattern is the indexing of diffraction peaks due to a germanium-gold ($Au_{0.72}Ge_{0.28}$) alloy

which is expected due to the VLS mechanism by which these nanowires grow. It should be noted that due to the large amount of particulate matter present in the sample, the XRD pattern would have a large contribution from these particles as well as from the nanowire material.

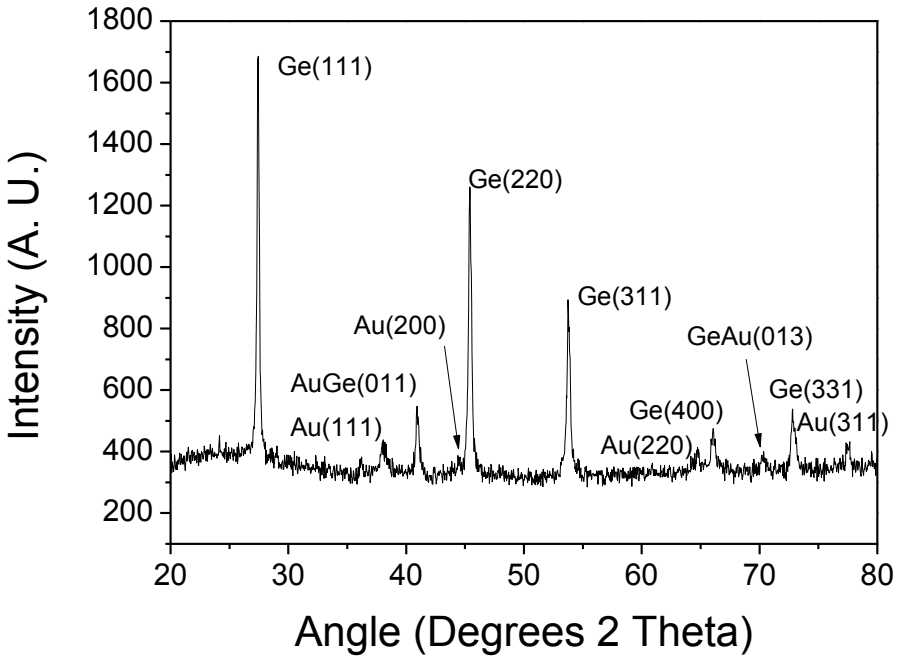


Figure 6.8 X-ray diffraction pattern of the PMO-AU-Ge material. The peaks were indexed using a JCPDS data base of common materials.

6.4.2 The Use of Polymer Templates in the Production of Nanostructures

Figure 6.9 shows AFM and SEM images of the etched polystyrene (PS) polymer thin film template used in this work which are described in greater detail in Chapter 2 but described here again briefly. Thin films of polystyrene (PS) - polymethylmethacrylate (PMMA) block copolymer were deposited via spin coating on an existing thin layer of PS-PMMA random copolymer on a silicon wafer from a 1% (w/w) PS-PMMA toluene solution. The samples were annealed under vacuum at 180°C to induce phase separation which resulted in vertical cylinders of PMMA arranged locally in a hexagonal fashion. The PMMA block and the polymer wetting layer were removed following deep UV exposure and subsequent washing with acetic acid and deionised water. The resulting film is seen in the AFM and SEM images in Figure 6.9. The AFM image in Figure 6.12(a) show the empty pore system after the PMMA block and the PS-PMMA random copolymer wetting layer were potentially removed. AFM measurements showed well ordered hexagonal domains and a relatively flat undamaged surface. The resulting pore dimensions of the PS matrix were 25 nm deep 50 nm wide with a 25 nm pore wall. The SEM image shown in Figure 6.9(b) shows again the ordered arrangement of hexagonal pores of the PS matrix.

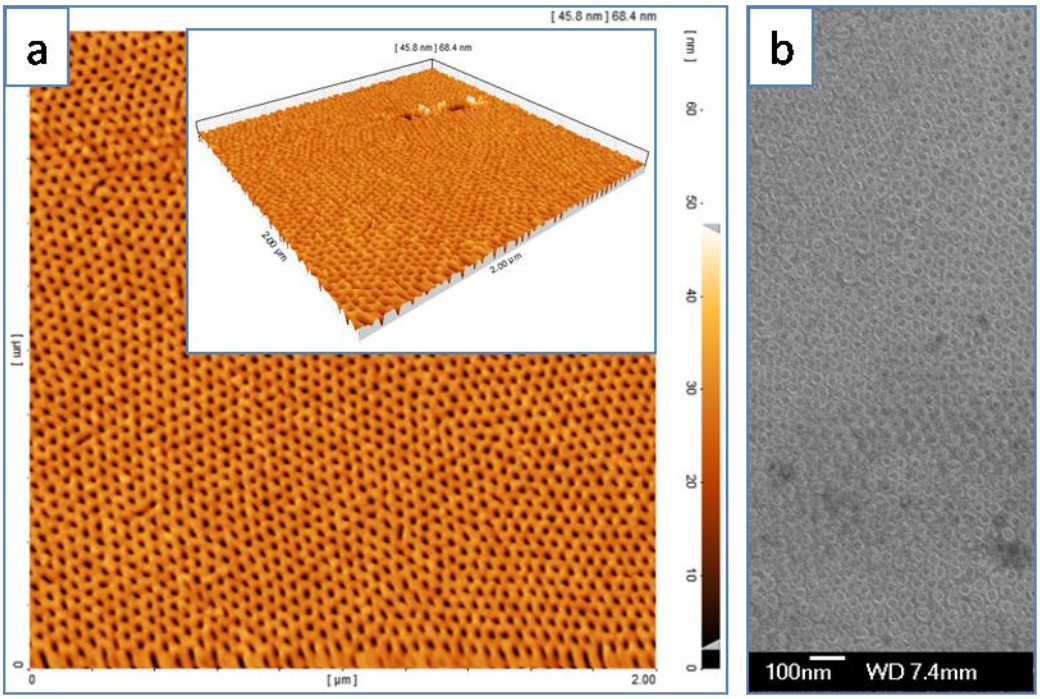


Figure 6.9 (a) AFM image of the hexagonally ordered porous PS matrix after removal of the PMMA block on silicon wafer and (b) an SEM image of the same material showing the hexagonally ordered pore structure of the PS matrix.

Once the exposed silicon of the PS polymer template was functionalised with thiol groups and treated with a suspension of thiol-stabilised gold nanoparticles, areas of the template had an altered appearance upon investigation with AFM. Figure 6.10(a) to (d) shows AFM images of the PS template treated with the suspension of Au nanoparticles and where there were once just empty pores there were now raised features, with the same approximate diameter (40 nm) of the empty pores (see inset Figure 6.10(c)). Other areas of the polymer template did not have the appearance of the raised features as shown in Figure 6.12 but remained that of an empty porous template.

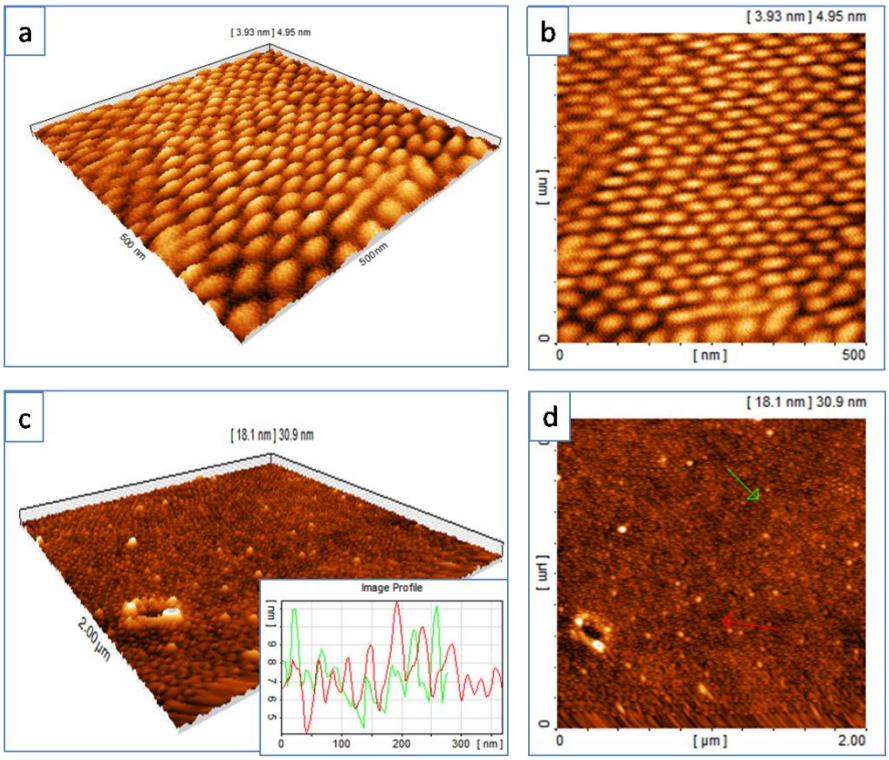


Figure 6.10 Figure (a) to (d) show AFM images of the vertical pore system of the PS matrix after functionalisation of the areas of silicon wafer which were not covered with PS and subsequent treatment in a suspension of thiol-stabilised gold nanoparticles. The inset in (c) is a cross-section profile of the red and green lines in image (d).

Figures 6.11(a) and (b) show SEM images of the vertical pore system of the PS matrix after chemical functionalisation of the exposed areas of the silicon wafer with thiol groups and subsequent treatment in a suspension of thiol-stabilised gold nanoparticles. The contrast between the pores containing the Au nanoparticles, which appear as the bright areas, and the PS matrix, darker areas, makes it relatively easy to image the PS template. Figure 6.11(c) shows an

x-ray photoelectron spectroscopy (XPS) spectrum of the PS matrix which underwent the same treatment as the samples in Figure 6.11(a) and (b). The XPS spectrum shows the presence of Au now present in the sample, the spectrum also shows the Si contribution as the x-rays penetrate the transparent polymer layer. The exchange between the thiol ligands stabilising the Au nanoparticles and the thiol-functionality at the bottom of the PS pore and the confinement of Au nanoparticles within the pore structure itself results in the aggregation of Au nanoparticles in the PS pore system.

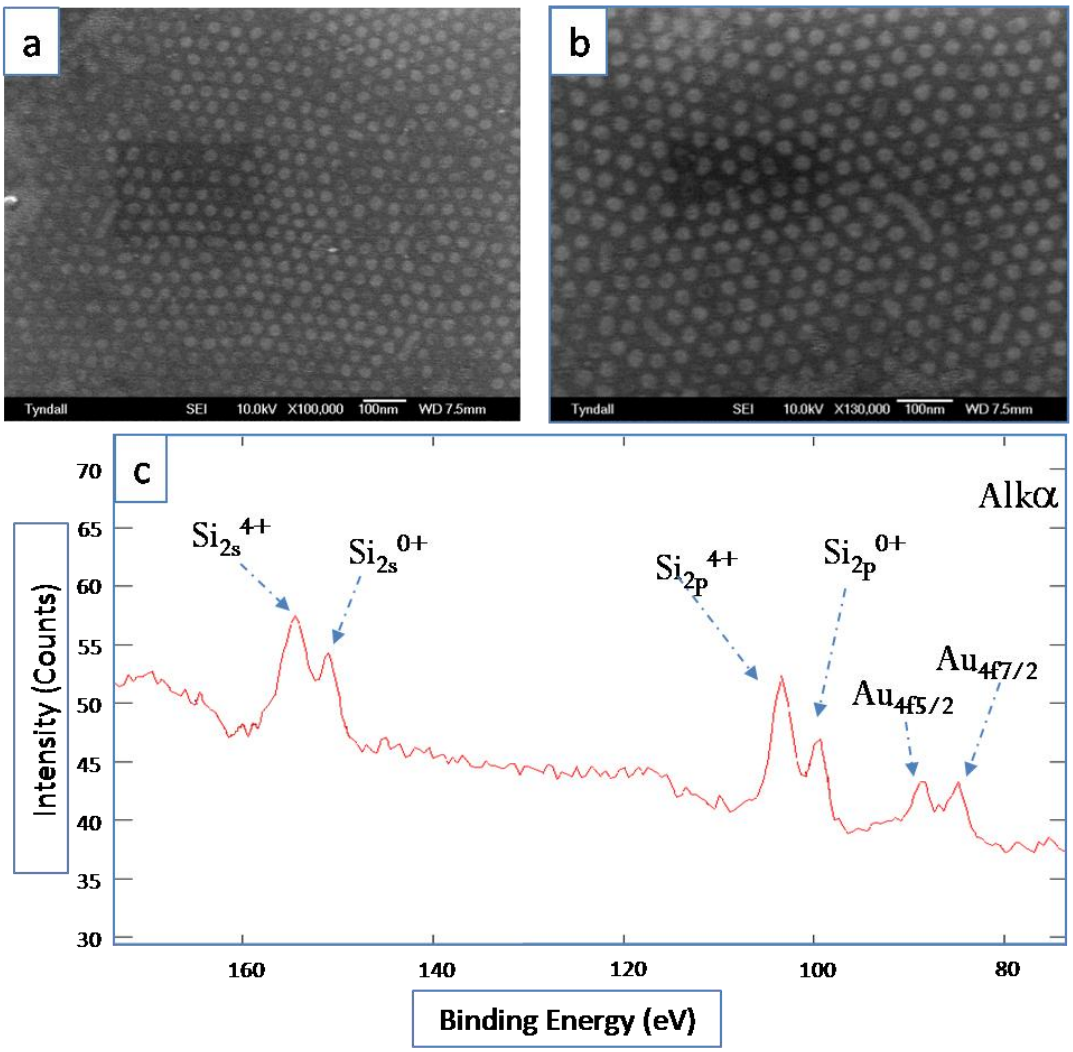


Figure 6.11 (a) and (b) show SEM images of the vertical pore system of the PS matrix after chemical functionalisation of the exposed areas of silicon wafer with thiol groups and subsequent treatment in a suspension of thiol-stabilised gold nanoparticles. (c) shows the XPS spectrum of similar PS polymer templates which underwent the same treatment.

Similar to the AFM analysis in Figures 6.12 only certain areas of the PS template showed this type of modification after treatment with the suspension of thiol-stabilised gold nanoparticles. The reason for this variation in coverage was established when a transmission electron microscopy (TEM) cross section was carried out on the templates. Figure 6.21 shows a TEM cross-section of the PS template. The process involved spluttering a gold over-layer on the PS template to add rigidity and more importantly contrast during the imaging process. The sample was then cross-sectioned and imaged, as shown in Figure 6.12. There is still a polymer layer present covering the silicon substrate at the bottom of the pore which is thought to be due to inconsistent coverage of the random PS-PMMA polymer wetting layer, leading to improper phase separation during the annealing step. Residual polymer still present in the bottom of the PS pore prevented functionalisation of the silicon wafer.

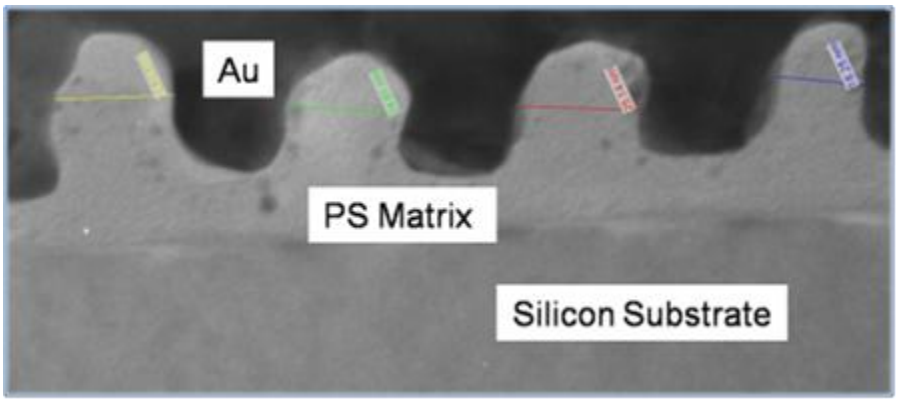


Figure 6.12 (b) TEM cross-section of the vertical pore system of the PS matrix before chemical functionalisation and treatment with gold nanoparticles solution showing the PS matrix and the depth reached during the PMMA etching step.

However, the PS templates where successful gold deposition had occurred were used as seed templates for the growth of Ge nanowires, the result of which can be seen in the SEM images in Figure 6.13. A variety of different diameter Ge nanowires were produced from the PS templated arrays of Au nanoparticles. However the expected ordered array of Ge nanowires which would mirror the array of Au nanoparticles within the PS matrix was not obtained. At the temperatures used during the synthesis of the Ge nanowires (up to 360°C) the PS template begins to decompose, between 300 to 350°C [37], and the Au nanoparticles begin to move and sinter into larger particles. Consequently when the gold-catalysed growth of Ge nanowires begins at 360°C, the Au nanoparticles that were once embedded in the PS matrix no longer retain the size, ordering and separation they once possessed. The resulting growth of Ge nanowires of a variety of diameters resembles a collection of nanowires which would be obtained from gold seeded wires deposited on a clean silicon wafer, as those shown in Figure 6.14(a) and (b). A more successful method of producing vertical nanowires was accomplished by Woodruff *et al.* who grew well ordered vertical nanowires of Ge from Au seeds using a chemical vapour deposition method [38]. The large clumps of material also shown in Figure 6.13 is the residue of the polymer decomposition.

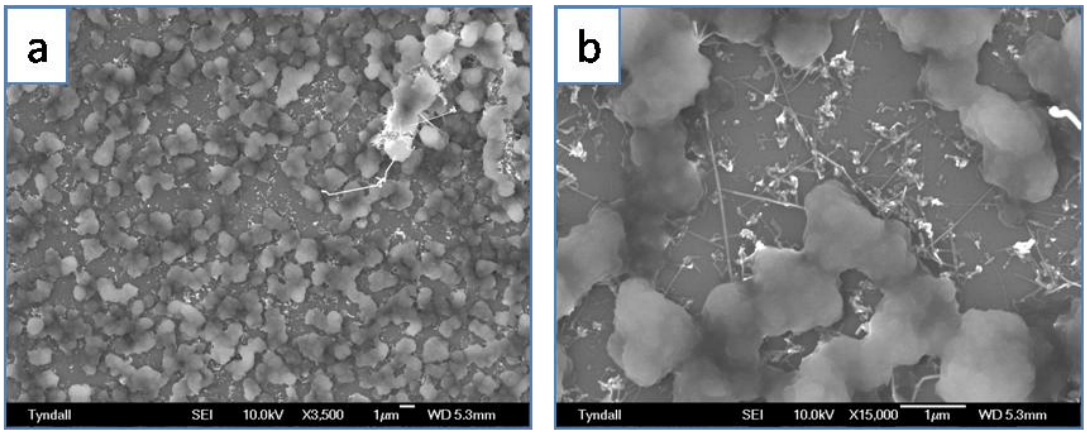


Figure 6.13 SEM images of the Ge nanowires grown from the Au-PS template which were recovered from the high pressure reaction.

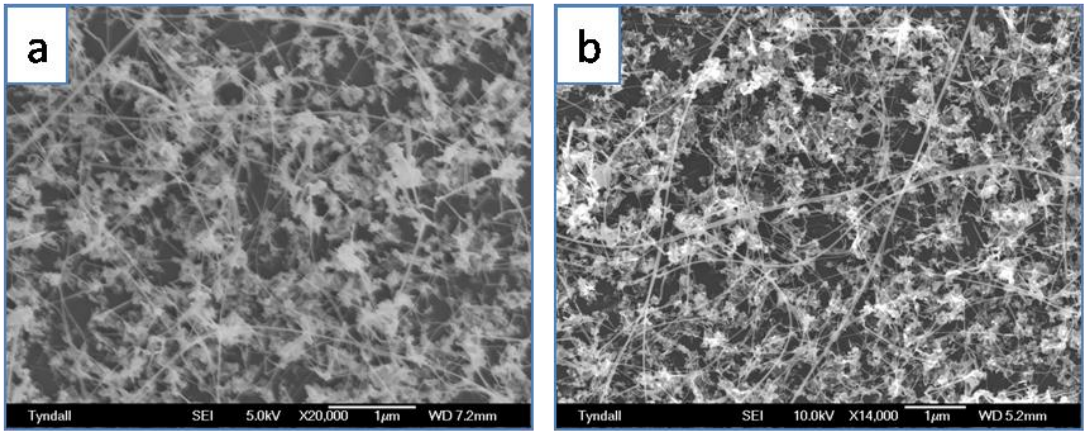


Figure 6.14 Shown are SEM images of the germanium nanowires grown from the Au nanoparticle deposition on a clean silicon substrate which was recovered from the high pressure reaction.

Figure 6.15 shows the XRD pattern of the recovered Ge-Au-PS template of the sample shown in Figure 6.13. The peak intensities are much lower than the intensities observed in Figure 6.12 which showed the XRD pattern of the material recovered from the Ge nanowires experiments using the PMO-Au material. The reason for the different intensities is due to the amount of sample being characterised, there was a very small amount of Ge and Au present in the polymer template experiments with respect to the PMO experiments. A diffraction peak was index as being due to a gold- germanium alloy ($Au_{0.72}Ge_{0.28}$) which was also seen in the PMO experiments mentioned previously.

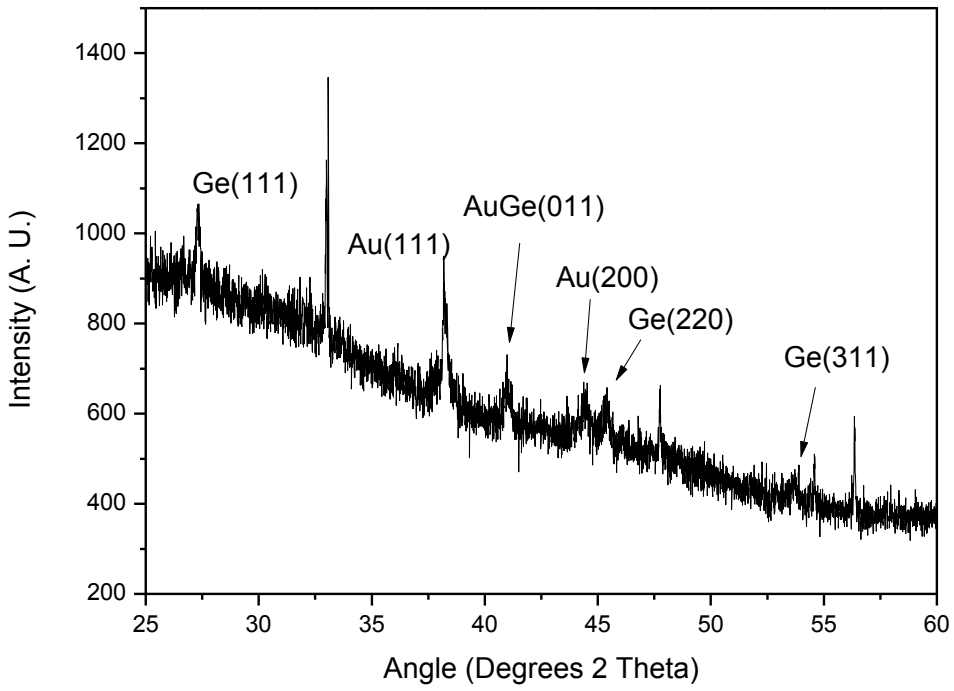


Figure 6.15 The XRD pattern of the Ge:Au PS template.

6.5 Conclusions

Ethylene bridged PMO was synthesised with a well ordered hexagonal pore structure and narrow pore size distribution as determined by XRD and N_2 adsorption analysis. Chemical modification of the surface of the PMO starting material was accomplished via the addition of thiol moieties to the surface. These thiol groups acted as reaction centres which deposited metallic Au clusters on the surface and in the pore network of the PMO by reduction of chloroauric acid. TEM and XRD analysis confirmed the presence of metallic Au clusters in the PMO material. The PMO-Au composite was then used to grow Ge nanostructures in a high temperature (360 °C) reaction in a pressurised hexane/sc-CO_2 atmosphere. From TEM analysis high aspect ratio Ge nanowires of various diameters were observed along with a lot of residual particulates. XRD data determined the crystalline nature of the sample, with contributions from crystalline Ge and Au but also a Ge-Au alloy which was determined to be a result of the growth mechanism of Ge nano-structures from a Au seed crystal.

A polymer template was also used to grow Ge nanostructures using a similar method as the one described for the PMO templates. A PS-PMMA polymer thin film was used which had the PMMA cylinder block removed comprised of a PS mask with exposed areas of the silicon substrate. The exposed areas of silicon substrate were functionalisation with the same thiol groups used the PMO functionalisation procedure and again acted as reduction centres which deposited metallic Au clusters within the PS pore, as determined by XPS, AFM and SEM techniques. However this deposition procedure was only partially successful due to certain pores

of the template not being completely etched to the silicon substrate and residual polymer remaining which was determined from a TEM cross-section of the sample. The PS template with embedded Au nanoclusters then underwent the same high temperature and pressurised hexane/sc-CO_2 as the PMO-Au composites. The recovered substrates, analysised using SEM and XRD, showed a number of nanowires growing randomLy from the sample but not with the expected regularity which would mirror the ordering of the Au nanoclusters form which they from. As a result of the high temperature at which the Au seeded Ge synthesis is carried out, the PS matrix which separates the different Au nanoclusters begins to decompose which eventually leads to the agglomeration of the nanoclusters before the catalysesd growth of Ge can occur. This results in the random growth of Ge nanowires which was observed in the SEM images.

6.6 References

1 Melde, B. J.; Holland, B. T.; Blanford, C. F.; Stein, A., Chem. Mater. 1999, 11, 3302.
2 Inagaki, S.; Guan, S.; Fukushima, Y.; Ohsuna, T.; Terasaki, O., J. Am. Chem. Soc. 1999, 121, 9611.
3 Hatton, B.; Landskron, K.; Whitnall, W.; Perovic, D.; Ozin, G. A., Accounts of Chemical Research 2005, 38, 305.
4 Yang, Q. H.; Liu, J.; Zhang, L.; Li, C., J. Mater. Chem. 2009, 19, 1945.
5 Shylesh, S.; Samuel, P. P.; Sisodiya, S.; Singh, A. P., Catal. Surv. Asia. 2008, 12, 266.
6 Rebbin, V.; Jakubowski, M.; Potz, S.; Froba, M., Microporous Mesoporous Mater. 2004, 72, 99.
7 Landskron, K.; Hatton, B. D.; Perovic, D. D.; Ozin, G. A., Science 2003, 302, 266.
8 Wight, A. P.; Davis, M. E., Chem. Rev. 2002, 102, 3589.
9 Hoffmann, F.; Cornelius, M.; Morell, J.; Froba, M., J. Nanosci. Nanotechnol. 2006, 6, 265.
10 Sze, S. M., Physics of semiconductor devices. Wiley-Interscience, New York.: 1981
11 Cui, Y.; Lieber, C. M., Science 2001, 291, 851.
12 Cui, Y.; Wei, Q. Q.; Park, H.; Lieber, C. M., Science 2001, 293, 1289.
13 Duan, X. F.; Huang, Y.; Cui, Y.; Wang, J. E.; Lieber, C. M., Nature 2001, 409, 66.
14 Dutta, A. K., Appl. Phys. Lett. 1996, 68, 1189.
15 Wang, D.; Dai, H., Angew. Chem. Int. Ed. 2002, 41, 4783.
16 Wagner, R. S.; Ellis, W. C., Appl. Phys. Lett. 1964, 4, 89.
17 Wagner, R. S.; Ellis, W. C.; Arnold, S. M.; Jackson, K. A., J. Appl. Phys. 1964, 35, 2993.
18 Holmes, J. D.; Johnston, K. P.; Doty, R. C.; Korgel, B. A., Science 2000, 287, 1471.
19 Liu, X.; Hanrath, T.; Johnston, K. P.; Korgel, B. A., Nano. Lett. 2003, 3, 93.
20 Holmes, J. D.; Ziegler, K. J.; Doty, R. C.; Pell, L. E.; Johnston, K. P.; Korgel, B. A., J. Am. Chem. Soc. 2001, 123, 3743.
21 English, D. S.; Pell, L. E.; Yu, Y.; Barbara, P. F.; Korgel, B. A., Nano. Lett. 2002, 2, 681.
22 Hanrath, T.; Korgel, B. A., J. Am. Chem. Soc. 2002, 124, 1424.
23 Hanrath, T.; Korgel, B. A., Adv. Mater. 2003, 15, 437.
24 Edwards, E. W.; Stoykovich, M. P.; Solak, H. H.; Nealey, P. F., Macromolecules 2006, 39, 3598.
25 Liu, C.-C.; Nealey, P. F.; Ting, Y.-H.; Wendt, A. E., J. Vac. Sci. Technol. B 2007, 25, 1963.
26 Guo, W. P.; Park, J. Y.; Oh, M. O.; Jeong, H. W.; Cho, W. J.; Kim, I.; Ha, C. S., Chem. Mater. 2003, 15, 2295.
27 Xiao, S. G.; Yang, X. M.; Edwards, E. W.; La, Y. H.; Nealey, P. F., Nanotechnol. 2005, 16, S324.
28 Hostetler, M. J.; Wingate, J. E.; Zhong, C. J.; Harris, J. E.; Vachet, R. W.; Clark, M. R.; Londono, J. D.; Green, S. J.; Stokes, J. J.; Wignall, G. D.; Glish, G. L.; Porter, M. D.; Evans, N. D.; Murray, R. W., Langmuir 1998, 14, 17.
29 Grudzien, R. M.; Grabicka, B. E.; Pikus, S.; Jaroniec, M., Chem. Mater. 2006, 18, 1722.
30 Loewenstein, L. M.; Mertens, P. W., J. Electrochem. Soc. 1998, 145, 2841.
31 Okorn-Schmidt, H. F., Ibm Journal of Research and Development 1999, 43, 351.
32 Faibish, R. S.; Yoshida, W.; Cohen, Y., J. Coll. Inter. Sci. 2002, 256, 341.

33 Gao, L.; McCarthy, T. L., J. Am. Chem. Soc. 2006, 128, 9052.
34 Tripp, C. P.; Hair, M. L., Langmuir 1992, 8, 1120.
35 Feng, X.; Fryxell, G. E.; Wang, L. Q.; Kim, A. Y.; Liu, J.; Kemner, K. M., Science 1997, 276, 923.
36 Zhang, W.-H.; Lu, X.-B.; Xiu, J.-H.; Hua, Z.-L.; Zhang, L.-X.; Robertson, M.; Shi, J.-L.; Yan, D.-S.; Holmes, J. D., Adv. Funct. Mater. 2004, 14, 544.
37 Kannan, P.; Biernacki, J. J.; Visco, D. P.; Lambert, W., J. Anal. Appl. Pyrolysis 2009, 84, 139.
38 Woodruff, J. H.; Ratchford, J. B.; Goldthorpe, I. A.; McIntyre, P. C.; Chidsey, C. E. D., Nano Lett. 2007, 7, 1637.

Chapter 7

Conclusions

Conclusions

The preceding chapters of this thesis outline the work undertaken on a variety of topics. Liquid crystal micelles and micelles in solution were exposed to high pressure CO_2 and selected high pressure hydrocarbon environments, the resulting changes observed in the micelles were recorded and interpreted using SANS. The arrangement of periodic mesoporous organosilicas within the channels of anodic alumina membranes under varying conditions were investigated using SAXS. PMOs and polymer thin films were used as templates with deposited gold nano-particles and used to grow germanium nanowires.

The work described in Chapter 3 outlines the characterisation of liquid crystal micelle films under high pressure CO_2 and propane. Liquid crystal films (essentially bulk liquid crystal phase) templated form the Pluronic F127 tri-block copolymer, the ionic surfactant CTAB and the non-ionic surfactant Brij 56 were subjected to high pressure environments and varying thermal conditions. The outcome was an observed increase in the spacing between neighbouring micelles (d-spacing) as the micelles adsorbed significant amounts of either CO_2 or propane and swelled in size while retaining the ordered structure of the liquid crystal. The CO_2 swelling route has the advantage over traditional swelling techniques which use solvents to swell liquid crystal micelles such as using glycols or trimethylbenzene, that the ordering of the micelles is retained even at high CO_2 pressure and enlarged micelle d-spacings. This swelling mechanism also has the advantage that a cosufactant was not needed to swell the liquid crystal micelles such as using SDS Pluronic liquid crystal micelle swelling agent and as a result a second mesophase phase was noticed in the Pluronic SANS scattering pattern. The work outlined in Chapter 3 continues

previous work in the field where supercritical CO_2 swollen Pluronic liquid crystals were used in the synthesis of mesoporous silica with varying pore diameters. The work here opens new possibilities in the production of mesoporous silica using CTAB and Brij 56 surfactants (or different varieties of these surfactants) in the production of mesoporous silica. The swelling observed in different gaseous environments was determined to be a function of the solubility of that gas in the respective liquid crystal micelles. The greatest swelling of the F127 liquid crystal was seen when CO_2 was employed as the swelling gas whereas there was no increase in d-spacing of the F127 liquid crystal when propane was used. However, when the liquid crystal films templated form Brij 56 and CTAB were exposed to a pressurised propane environment the liquid crystal was seen to lose order and destabilise, this was seen as a loss in the SANS peak intensity and a splitting of the peak, which was quite probably due to liquid crystal melting which has been reported in the past when liquid crystals are exposed to high pressure. However, this worked showed for the first time the swelling of liquid crystal by pressurised atmospheres. Carbon dioxide swollen liquid crystals have been utilised in the past in the production of large pore mesoporous silica but this is the first time the swelling of the pure liquid crystal has been demonstrated and measured. More in-depth study of a possible solvent induced liquid crystal phase change would reveal more information on liquid crystal stability at various gas densities which would be of great interest to this research field.

Chapter 4 describes the work conducted to characterise the effect that pressurised CO_2 and hydrocarbon environments have on F127 and CTAB micelles. The micellar solutions were composed of a dilute solution of each surfactant. Different pressures and changing thermal

conditions at a fixed pressure were employed to investigate the resulting influences on the different micellar solutions. The SANS data collected at each pressure and temperature were modelled using an appropriate mathematical model which best described the micellar system under investigation. Like the liquid crystal swelling seen in Chapter 3 an increase in micelle size was also seen here. From the results of the mathematical modelling it was determined that the increasing core radius and subsequent increase in the micelle radius was a result of uptake of the swelling solvent form the high pressure environment into the core of the micelles. During the modelling of the micellar systems the amount of swelling solvent in the core of the micelle, which was ultimately responsible for the swelling, was determined. The determination of the amount swelling solvent in the micelle core is the novel aspect of this work which separates it from standard reported work in the area of SANS investigation of swollen micelles. This work not only provides fundamental understanding of swelling micelles with high pressure gases but this work can also be used as a basis for the swelling of micelles using more conventional swelling routes like those of using organic solvents. A number of other micelle parameters were successfully modelled during the swelling process, including the aggregation number of the micelle, the degree of hydration in the core and the corona and the micelle volume fraction. The modelling study of the micelle SANS data resulted in a more detailed understanding the swelling which occurs when the micellar system is exposed to a high pressure environment. The different swelling observed in various micellar systems under different gases uncovered fundamental solubility characteristics which lay at the heart of the micelle swelling seen here. Further investigation of the swelling of micellar systems or liquid crystal systems for that matter, using different solvents with a separate solubility study run in parallel would unveil definite solubility requirements for the swelling of micelles and also determine how much solvent is required to

obtain a swelling response. Also further investigation is needed to determine if increased pressure (gas, liquid or SCF) has the effect of reducing the critical micelle concentration or if a reduction in the critical micelle temperature is seen.

The investigation of a PMO material deposited in the channels of anodic alumina membranes (AAM) is described in Chapter 5. The deposition of a PMO gel in the channels of AAMs under varying humidity conditions and with varying weight percentages of organic precursor resulted in different mesostructures being observed. Using SAXS measurements it was possible determine to the resulting mesostructure within the AAM channels *ex-situ* or to measure to formation of such mesostructures *in-situ*. Over-layer films which resulted from the formation of a mesoporous film on the surface of the AAM interfered with *in-situ* formation measurements of the mesostructure within the AAM channels, but did not hinder the successful determination of the present mesophase. Complementary TEM measurements helped confirm the types of structure which were present in the channels of the AAMs. The humidity conditions under which the deposition took place, which ultimately determines the rate of evaporation of the volatile components of the gel, was determined to have a major effect on the formation of one mesostructure over another. The undertaken time resolved study which observed the formation of the PMO mesostructure from initial deposition until the formation of a stable mesostructure revealed great insight into the formation of the mesostructure. Time resolved measurements like this are vital for the observation of various transitions which occur during the formation of mesoporous materials. This research shows the importance of the correct deposition conditions in order to achieve the correct pore morphology. Further study to improve the PMO adhesion to

the AAM walls and contraction characteristics of the PMO material during high temperature calcination would result in a higher quality porous material with improved separation ability.

Chapter 6 outlined the use of PMO powders and PS-PMMA polymer thin films as templates for the growth of germanium nanowires. The highly ordered pore structure of the PMO material was chemically modified with thiol functionality which acted as reduction centres in the reaction with chloroauric acid which leads to the deposition of gold nanoclusters in the internal pore structure and on the external surface of the PMO materials. The gold nanoclusters acted as catalysts in the seeded growth of germanium nanowires. TEM images showed well defined nanowires growing from the surface of the PMO material, while XRD analysis showed the chemical composition of the material as being mostly germanium but with some traces of a germanium-gold alloy, along with residual gold seeds still present. The work reported in Chapter 6 which makes use of PMO materials increases the possible applications of PMOs. Vertical pores of a polystyrene matrix were also used as templates for the deposition of gold nanoparticles using the same chemistry as used for the PMO materials. Using the same functionalisation method, the areas of exposed silicon were chemically modified with the same thiol groups as were used in the PMO section. Gold nanoparticles were successfully deposited within the pores of the PS matrix which again acted as seeds for the growth of germanium nanowires. The high temperature which is needed for the growth of crystalline germanium nanowires (even when a catalyst such as gold was used) resulted in the destruction of the polymer template and agglomeration of the gold nanoislands before the catalysed growth of the germanium nanowires could begin. The agglomeration of the gold seeds resulted in the

uncontrolled growth of germanium nanowires which led to a collection of nanowires of varying diameters and position. SEM was able to show the gold catalyst bulbs at the end of the germanium nanowires and also the residue of polymer template. Also it was determined that problems with the etching process during the polymer thin film production process resulted in areas of the thin film which were not etched all the way to the silicon wafer. Polymer have been used in the past to selectively deposit nanoparticles, however are very few reports of polymers being used as templates to grow nanostructures and it is vital for the field of polymer templating if it is to expand that industry relevant applications such as these are found. Further work is needed to produce polymers with enough thermal stability to withstand degradation and retain their structure at the temperatures used in the nanowires synthesis used here. Also, to be commercially useful, nanowires need to be grown without the benefit of a gold catalyst due to the poor electrical characteristics which germanium nanowires grown from gold possess. Lower synthesis temperatures may be achieved if a different catalyst is used, may be a bi-metallic compound, all of which requires further investigation.